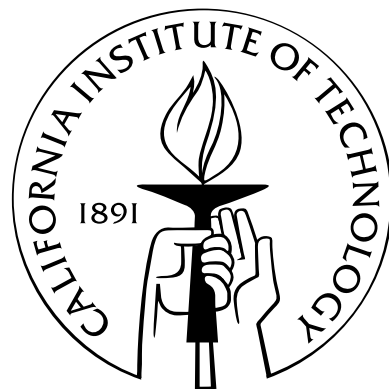


**Discrete Modeling of Granular Media:
A NURBS-based Approach**

Thesis by
Keng-Wit Lim

In Partial Fulfillment of the Requirements
for the Degree of
Doctor of Philosophy



California Institute of Technology
Pasadena, California

2015
(Defended November 25, 2014)

© 2015

Keng-Wit Lim

All Rights Reserved

To my family

Acknowledgements

I would like to begin by thanking the members of my thesis committee — Drs. José Andrade, Michael Ortiz, Pablo Ampuero, and Ravi Ravichandran — for their guidance, feedback, and advice during my time at Caltech. I am indebted to my advisor, Dr. José Andrade, for his enthusiasm and encouragement to pursue topics that I found truly interesting and exciting. I would also like to thank our collaborators, Dr. Kristian Krabbenhoft, for his technical advice on contact dynamics, as well as Drs. Gioacchino (Cino) Viggiani and Edward Andò for providing us with experimental data.

I would also like to thank my family for the support they have given me throughout my entire life, and in particular I must acknowledge my wife, Ailsa, for her support, encouragement, quiet patience, and unwavering love.

I am grateful for the financial support I received from the National Science Foundation (NSF CAREER Grant No. CMMI 1060087) and Air Force Office of Scientific Research (AFOSR YIP Grant No. FA9550-11-1-0052), without which I would not have been able to complete this work.

Abstract

One of the most critical drawbacks of current discrete element method (DEM) technology is its inability to account for complex particle morphological features, namely sphericity and roundness, due to the underlying primitive geometry bases (e.g., disks or spheres and simplexes), as well as the complexity of the associated contact algorithms. While the influence of particle morphology on properties such as strength and permeability is well established, DEM has not yet been able to incorporate particle morphological features to the extent that they become a truly predictive and useful tool for general granular materials.

To overcome the aforementioned difficulties, we have developed a new DEM based on Non-Uniform Rational Basis Splines (NURBS). The NURBS-based DEM aims to improve the representation of particle morphology in computations and ease the transition from binary images, in particular those obtained from X-Ray computed tomography, to discrete models.

With NURBS, the new DEM allows for the representation of particle morphological features to their fullest extent, with local contact rolling resistance and interlocking emanating directly from grain geometry. In addition, modeling flexibility is significantly enhanced to a level that is comparable with isogeometric methods. As such, the transition from image data to particle shapes is greatly streamlined. More importantly, increased macroscopic strength in granular packings composed of angular particles is fully captured.

The NURBS-based DEM is a first step towards constructing a new discrete element strategy that eliminates all the major deficiencies that have plagued classical DEM for a long time while at the same time maintaining a level of implementation simplicity that is comparable to classical DEM. These developments provide a long-awaited path forward towards a simple and predictive discrete analysis tool.

List of Figures

1.1	A definition of particle morphological features [1].	2
1.2	Schematic showing unified tomography-to-simulation framework across scales (left to right) and integration of characterization and simulation (top to bottom). Areas of relatively established understanding (shown in solid puzzle pieces), such as grain-scale tomography and simulation, are contrasted with focus areas that are in active development. Level sets, GEM [2; 3], and NURBS are key computational ingredients to enabling grain-scale characterization and simulations, which yield particle kinematics and forces. Using such quantities, multiscale methods provide the link between experiments and continuum plasticity models to complete the proposed framework (after [4]).	7
1.3	Using NURBS as a representation for grain morphology.	8
2.1	Illustration of two particles (Ω^i and Ω^j) that are potentially contacting. The gap g between the particles is positive if the particles are separated, and negative if the particles overlap. The moment arms emanating from each particle's centroid to its corresponding contact point are denoted by \mathbf{R}_i and \mathbf{R}_j for Ω^i and Ω^j , respectively.	12
2.2	Graph of non-smooth contact laws: (a) normal reaction force p against separation or gap g and (b) friction force $\ \mathbf{q}\ $ against slip; μ is the friction coefficient.	19
3.1	Schematic illustration of a NURBS curve. The curve degree p is 3 (cubic). The knots u_i and weights w_j are listed in the vectors U and w , respectively. The kink in the curve is due to full multiplicity $k = p = 3$, in which the knot/parameter value $u = 0.75$ is repeated $p = 3$ times.	27
3.2	Contact problem between two particles Ω^i and Ω^j . Refer to text for description.	33

3.3	Measures used for terminating the NURBS subdivision in the knot or node generation procedure. The two normal vectors emanating from nodes A and B are denoted by \mathbf{n}_A and \mathbf{n}_B , respectively. NURBS parametric directions are u and v	35
3.4	Example cases of sample and subdivide. For cases (a) and (b), the domain is square, and the subdivision is such that the largest subrectangles contain the sample points with the best function values, i.e., lower f values. For cases (c) and (d), the domain is rectangular, and the subdivision is performed only along the long dimension.	40
3.5	A schematic of the graph of $f(\mathbf{c})$ versus d for all rectangles in the parametric domain. Refer to the text for the meaning of the labeled quantities.	41
3.6	Illustration of DIRECT algorithm. For simplicity, we have set ϵ in (3.19) to zero. The lines are only to guide the eye — there is no physical subdivision of the NURBS surface or underlying parametric surface; instead the subdivision is performed implicitly through sampling and selection of optimal rectangles.	45
4.1	Illustration of the problem of contact between two particles (Ω^i and Ω^j) at time t_0 . See text for a description of the associated quantities.	51
4.2	Linear elastic contact law: (a) normal reaction force p against separation or gap g and (b) friction force $\ \mathbf{q}\ $ against slip; μ is the friction coefficient.	58
4.3	Biaxial compression: initial and final ($\epsilon_a = 0.21$) configurations with $k_N = 10^8$	61
4.4	Biaxial compression: response with $k_N = \infty$	62
4.5	Biaxial compression: response $k_N = 10^8$	62
4.6	Biaxial compression: response $k_N = 10^6$	63
4.7	Biaxial compression: response $k_N = 10^5$	63
4.8	Column drop test with interparticle friction coefficient of $\mu = 0.5$: comparison between non-convex and angular particles.	66
4.9	Column drop test with interparticle friction coefficient of $\mu = 0.5$: comparison between non-convex and disk particles.	67
4.10	Configurations of columns with interparticle friction coefficient of $\mu = 0.5$ at step 1600: approximate dimensions relative to column with non-convex particles.	68

4.11	Column drop test with interparticle friction coefficient of $\mu = 0$: comparison between non-convex and angular particles.	69
4.12	Column drop test with interparticle friction coefficient of $\mu = 0$: comparison between non-convex and disk particles. We note that at step 3200, the column with disk particles continues to flow; a final layer thickness of 1 particle is reached as the simulation is progressed.	70
4.13	Configurations of columns with interparticle friction coefficient of $\mu = 0$ at step 3200: approximate dimensions relative to column with non-convex particles. We note that at this point in time the column with disk particles continues to flow; a final layer thickness of 1 particle is reached as the simulation is progressed.	71
5.1	Grain-scale imaging using XRCT: (a) slice of triaxial specimen and (b) 3D reconstruction by stacking slices.	76
5.2	Summary of characterization steps: (left) slice of 3D XRCT volume of voxels, (middle two) application of proposed characterization technique, and (right) generated grain.	77
5.3	Macroscopic load-displacement response. Inserts: triaxial specimen at (a) initial state and (b) 9.11 % axial strain, with shear band highlighted. Station numbers are labeled in red.	81
5.4	Incremental displacement field between tomographic stages 6 and 7 obtained from DIC: (a) contour of magnitude of incremental displacement vector with shear band within the region indicated by dashed lines and (b) incremental displacement arrows.	82
5.5	Dilatancy inferred from DIC data with fit for multiscale calculation (see Section 5.3.3).	83
5.6	Global response from multiscale computation using dilatancy evolution information inferred from DIC (refer to Figure 5.5).	84
5.7	Unit cells 1 and 2, generated through the characterization step using 3D XRCT data. The shaded grey region shows cell orientation in local coordinate system with respect to the global coordinate system.	85

5.8	Deformed configurations for unit cells 1 and 2. Shaded grey region shows cell orientation in local coordinate system with respect to the global coordinate system: final applied shear angle is 40° from the 3-axis.	86
5.9	Results from discrete computations: evolution of (a) dilatancy and (b) stress ratio.	87
5.10	Global response from multiscale computation using dilatancy evolution information from discrete models (insert).	88
A.1	Initial configuration for nine-disk test.	93
A.2	Normal force F_n evolution at C for loading case (a) No. 1 at different values of global numerical damping.	94
A.3	Evolution of normal force F_n for all loading cases reported in Table A.1 with global numerical damping $\xi = 3$	95
A.4	Distorted configurations for nine-disk assembly after 5000 cycles of uniform compression and settlement, and after a subsequent 500 cycles of constant volume (shear) distortion. Results shown correspond to case when $k_n = k_s$ and interparticle friction angle $\phi = 30^\circ$	96
A.5	Normal and shear force evolution at point C in nine-disk assembly during 500 cycle shear distortion at various k_s/k_n ratios. (a) Interparticle friction angle $\phi = 15^\circ$. (b) Interparticle friction angle $\phi = 30^\circ$	96
A.6	Elastic collision: energy history.	97
A.7	Elastic collision: momentum history.	98
A.8	Elastic collision: velocity v_x history.	98
A.9	Elastic collision: velocity v_y history.	99
A.10	Plastic collision: energy history.	99
A.11	Plastic collision: momentum history.	100
A.12	Plastic collision: velocity v_x history.	100
A.13	Plastic collision: velocity v_y history.	101
A.14	Quasistatic sliding along a rigid frictional surface.	103
A.15	Dynamic sliding along a rigid frictional surface.	103
A.16	Block on an incline.	105
A.17	Displacement along x ($\mu = 0.36$).	107

A.18	Velocity along x ($\mu = 0.36$).	107
A.19	Displacement normal to plane or gap ($\mu = 0.36$).	108
A.20	Shear force ($\mu = 0.36$).	108
A.21	Normal contact force ($\mu = 0.36$).	109
A.22	Displacement along x ($\mu = 0.4$).	109
A.23	Velocity along x ($\mu = 0.4$).	110
A.24	Displacement normal to plane or gap ($\mu = 0.4$).	110
A.25	Shear force ($\mu = 0.4$).	111
A.26	Normal contact force ($\mu = 0.4$).	111

List of Tables

3.1	Control points (x_i, y_i) and weights w_i for a unit circle.	29
4.1	Comparison of Non-Smooth Contact Dynamics and classical DEM	48
A.1	Loading cases for uniform compression test	93

Contents

Acknowledgements	iv
Abstract	v
1 Introduction	1
1.1 General Overview	1
1.1.1 Characterization and modeling approaches	1
1.1.2 The role of particle morphology	2
1.1.3 Current shape representation techniques in discrete models	3
1.1.4 Connection between experiments and discrete modeling	5
1.2 Motivation	6
1.3 Research Objective	6
1.4 Contribution	9
1.5 Overview of Thesis	9
2 Discrete Methods	11
2.1 Discrete Element Method	11
2.1.1 Normal force and associated moments	11
2.1.2 Tangential force and associated moments	13
2.1.3 Discrete equations of motion	14
2.2 Contact Dynamics	19
3 NURBS-based Discrete Element Method	24
3.1 Non-Uniform Rational Basis-Splines (NURBS)	24
3.1.1 Basis-Splines (BS)	25
3.1.2 Rational B-Splines (RBS)	26

3.1.3	Non-Uniform (NU) Rational B-Splines (NURBS)	27
3.1.4	Closing a NURBS curve	28
3.1.5	NURBS surfaces	30
3.1.6	Relevance of NURBS to DEM calculations	30
3.2	Contact Problem and Implementation	32
3.2.1	General definition	33
3.2.2	Knot positioning	34
3.2.3	Distance function	37
3.2.4	The DIRECT optimization algorithm	37
3.2.4.1	Sample and subdivide	38
3.2.4.2	Identification of potentially optimal rectangles	41
3.2.5	Implementation of contact algorithm	43
3.3	Closure	46
4	A Contact Dynamics Formulation	47
4.1	Introduction	47
4.2	Governing Equations for Frictional and Arbitrary-Shaped Particles	51
4.2.1	General contact problem definition	51
4.2.2	Notation for general multi-particle system	52
4.2.3	Discrete update equations	53
4.2.4	Variational formulation of contact problem	54
4.2.5	Optimality conditions	55
4.2.6	Force-based problem	56
4.2.7	Static limit	56
4.2.8	Solution procedure and computational complexity	57
4.3	Contact Implementation	58
4.4	Numerical Examples	59
4.4.1	Biaxial compression	59
4.4.2	Column drop test	64
4.5	Closure	65

5 Multiscale Characterization and Modeling of Granular Materials through a Computational Mechanics Avatar: A Case Study with Experiment	72
5.1 Introduction	72
5.2 The Avatar Framework	75
5.2.1 Characterization toolbox	75
5.2.2 NURBS-based discrete element method	78
5.3 Case Study	80
5.3.1 Experiment setup	80
5.3.2 Dilatancy inference	80
5.3.3 Multiscale computation	82
5.3.4 Discrete modeling	85
5.4 Closure	87
6 Conclusions and Future Work	89
6.1 Conclusions	89
6.2 Future Work	90
A Verification Tests	92
A.1 Classic DEM Tests	92
A.1.1 Uniform compression test	93
A.1.2 Distortion test	94
A.2 Contact Dynamics Binary Collision Tests	97
A.3 Kinematics with Associated Sliding Rule	102
A.3.1 Quasistatic case	102
A.3.2 Dynamic case	103
A.3.3 The case with rotations included	104
A.3.4 A numerical test	105
B Three-Dimensional Contact Dynamics Formulation	112

Chapter 1

Introduction

1.1 General Overview

1.1.1 Characterization and modeling approaches

Most geomaterials used in field-scale applications are modeled using continuum mechanics [5; 6]. Continuum methods rely on constitutive models that are, by and large, developed phenomenologically [7–12]. These models have been shown to be predictive in many areas of science and engineering, but are unable to quantitatively answer more fundamental questions related to instability, shear banding, and failure in granular materials (e.g., avalanches and liquefaction), in which the changing micromechanical structure plays an important role.

On the experimental side, new technologies are enabling unprecedented access to information at lower scales that have not been considered possible several years ago. Progress has been made in unraveling much of the kinematic processes in granular matter mostly owing to X-ray computed tomography (CT) [13–16]. For example, it is now possible to obtain full field kinematics in sand particles as they are loaded macroscopically [17]. Using X-ray CT, it is thus possible to obtain all translational and rotational degrees of freedom in each particle for thousands of particles constituting a macroscopic assembly. In the area of interparticle forces, new developments using 3D X-ray diffraction [18] have shown that it is possible to measure average elastic strains in sand particles under macroscopic loading [19]. These experiments, however, do not furnish a means to measure interparticle forces. Photoelasticity was a tremendous contribution to the ability to infer interparticle contact forces, but it is limited to birefringent materials [20; 21] and hence cannot be applied to natural granular materials such as sands. The ability to measure interparticle forces in

natural granular materials is the missing link to constructing better constitutive models for granular materials, especially with the advent of multiscale models capable of using these incredibly rich kinematics [22].

Given that the relationship between interparticle forces and macroscopic stresses has been known for decades [23], one natural proposal would be to use a discrete model in conjunction with grain shape measurements to reproduce the macroscopic response of an experiment and at the same time infer the interparticle forces. The discrete model would operate at the fundamental level, i.e., Newtonian mechanics for particles. One such discrete approach is offered by the Discrete Element Method [24] (DEM). DEM, introduced more than three decades ago, was predicated on the possibility of revealing micromechanical features that were simply not accessible to continuum models. This modeling paradigm has allowed tremendous access to quantities such as contact forces, enabling the understanding of most features of the micromechanical behavior of granular materials and link them to macroscopic response [23]. This link, however, remains qualitative and this is mostly due to the inability to capture grain morphology accurately.

1.1.2 The role of particle morphology

Particle morphology can be characterized, in general, by three properties: sphericity, roundness, and roughness [1] (see Figure 1.1). These properties are sometimes referred to by other

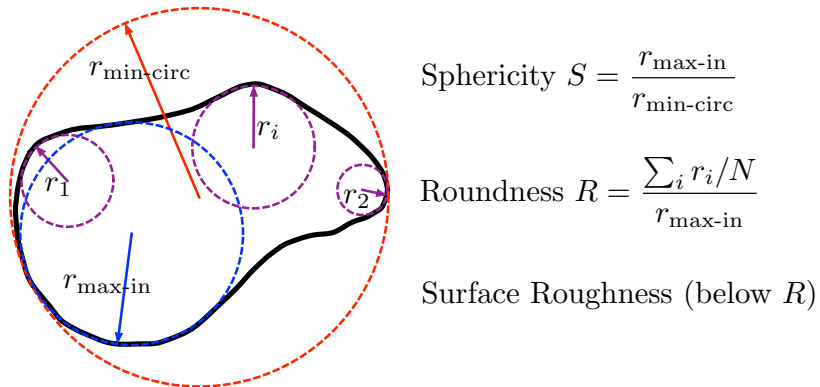


Figure 1.1: A definition of particle morphological features [1].

names, such as shape, angularity, and surface roughness, respectively [25]. These properties are scale dependent, as they measure morphological characteristics at different length scales, with increased spatial resolution needed to measure roughness, for example. Particle

morphology has been shown to be crucially important for macroscopic properties in granular materials. Some of the most critical macroscopic properties used in granular materials are strength and permeability, and both of these are intimately affected by particle morphology (e.g. [1; 26]). In the case of macroscopic strength, it has been determined that lack of sphericity, sharper angularity, and increased roughness all lead to increased mobilized strength in granular materials [1]. This macroscopic effect is due to micromechanical effects such as an increased number of contact points. Therefore, the ability of discrete models for granular materials to accurately capture particle morphology is of paramount importance if they are to correctly predict the macroscopic strength in real granular materials such as sands.

1.1.3 Current shape representation techniques in discrete models

In the past, researchers have attempted to incorporate the effects of particle shape or non-sphericity through rolling resistance. The prototypical rolling resistance model appears to originate from the work of Iwashita and Oda [27], who recognized that rotational resistance arises not only from contact behavior, but also from particle shape. In particular, they observed large voids and rotational gradients in shear band experiments, which were never reproduced by conventional DEM (at the time disks and spheres) since rolling would occur without any resistance at the contacts. To minimize the discrepancy between DEM simulations and experiments, they modified the classic DEM to include rolling resistance at the contacts. Their model treated the rolling resistance with a combination of an elastic rotational spring, a dashpot, a non-tension joint and a slider. The rolling resistance was provided through a pair of torque couples calculated as the product of the relative particle rotation and rotational spring stiffness, with the dashpot providing viscous damping for numerical stability. Using this model, they were able to predict shear band behavior that was similar to that seen in natural granular soils.

The work of Iwashita and Oda attracted wide interest and their rolling resistance model was subsequently adopted and extended in other studies (e.g., [28–33]). There can be, however, marked differences between the various proposed rolling resistance models, which may be attributed to the different assumptions on the physical sources contributing to rolling resistance [34]. As a result, the effectiveness of rolling resistance models can be problem dependent. In addition, these models contain artificial parameters, which are

usually chosen independently by trial and error. Despite these limitations, the introduction of rolling resistance models marked a defining moment in discrete modeling, when particle shape was recognized as an importance source of rolling resistance affecting the macroscopic strength of granular media.

More recent discrete simulation approaches include techniques to represent complex particle morphology or shape, beyond disks/spheres and ellipses/ellipsoids, which are based mostly on the clustering or clumping technique [35; 36] and polyhedra approach [37–41]. Through these techniques, rolling resistance would directly emanate from the geometry representation without relying on artificial rolling resistance models.

In the clustering technique, a group of spheres or circles are arranged and overlapped so that the outer curves or surfaces combine to approximate the shape of the grain. Then, the same disk-disk or sphere-sphere contact algorithm is reused over all potentially contacting pairs. The use of spheres in clustering techniques, while computationally inexpensive and easily implemented, is unappealing because of the lack of continuity in the curvatures and tangents. For example, the grains appear ‘clumpy’ at locations where spheres overlap or clump, and the curvature at any point in spherical-based discrete element is always positive. These anomalies prevent spherical-based discrete elements from higher fidelity contact mechanics calculations without further numerical treatment.

The polyhedra is essentially a rigid finite element. In 2D, the boundaries are represented as line segments while in 3D, the surfaces are represented using triangles or quads, similar to finite elements. In principle, polyhedra-based discrete elements can be refined as much as needed for an arbitrarily accurate grain shape representation. In practice, however, this resolution increase makes computational cost associated with narrow-phase contact detection and force calculations prohibitively expensive. As such, polyhedra-based discrete elements tend to appear ‘blocky’ and their shape representation capabilities not fully realized. In addition, the contact algorithms available for these geometrical entities are rather complex as they introduce the need to deal with face-to-node, node-to-node, and face-to-face contact. All development work on polyhedra techniques to date have focused almost exclusively on drawbacks:

- 1. compute cost on complex contact detection
- 2. not represent realistic enough shapes
- 3 convex only

the treatment of convex particles (e.g., [42]).

Alternatives, which are essentially combinations of the aforementioned techniques, include spheropolyhedra [43; 44] and potential particles [45; 46]. Spheropolyhedra are defined by the Minkowski sum of a simplex (either a point, a line segment, a triangle, or a tetrahe-

dron) with a sphere with radius r centered at the origin. The simplex serves as a skeleton for the particle and the radius r defines the distance of the particle surface from the skeleton. Potential particles are based on polyhedra with slightly rounded corners, edges, and faces. They are described by a smooth function that provides an analytical inside-outside check determined by the sign of the potential function, and the level sets of the function are strictly convex. In [46], a different potential function that enables the representation of spheres truncated with flats is proposed. These alternatives are still limited in terms of shape representation because their underlying formulations are based primarily on primitive geometries such as spheres, planes, and simple analytical functions.

In the several decades following the inception of DEM [24], there were tremendous efforts in the development of shape representation capabilities and associated contact algorithms (e.g., [35–37; 40]). Currently, however, it appears that progress has hit a plateau with shape representations, largely belonging to either the polyhedra or clustering approach, still too crude for real grain-scale calculations.

1.1.4 Connection between experiments and discrete modeling

While the influence of particle morphology on properties such as strength, permeability, etc. is well established [1; 26], it appears that grain-scale modeling and characterization efforts have remained compartmentalized, as exemplified by a relative lack of connection between real experiments and discrete modeling. In cases where discrete modeling of real granular materials with non-trivial geometries were attempted, crude discrete models with large geometrical biases and significantly calibrated parameters have been widely employed. Interestingly, the effects of geometrical bias on grain-scale response from use of simplified geometries are largely not discussed or quantified in the literature. It appears that the current gap between grain-scale modeling and characterization technologies is quite large. While imaging techniques are becoming increasingly sophisticated [13–17], there continues to be a lack of effort to bring discrete granular simulation technology closer to the engineering application level. To our knowledge, there is currently no work on discrete modeling of real granular materials at the grain scale.

1.2 Motivation

A discrete model that can directly incorporate particle morphological features (to within imaging resolution), and that can predict the response of real granular assemblies would eliminate the current bottleneck preventing the application of discrete models on real granular materials. More generally, a morphologically representative discrete model would allow computational discrete mechanics to catch up with and probe into the wealth of information offered by experimental techniques such as X-ray CT and X-ray diffraction, and probe the micromechanical response of a wide array of granular materials available in nature. At the same time, these advances would enable the development of new and more physics-based continuum constitutive models, relying less on phenomenology, as well as improve the predictive capabilities of multiscale methods that incorporate an underlying granular discrete model.

1.3 Research Objective

We look at the research objective in relation to the recent development of a tomography-to-simulation framework for studying granular materials [4], as illustrated in Figure 1.2. In support of this framework, computational techniques have been developed to extract and transition from binary image data of grains to the grain-scale quantities such as particle morphological features, kinematics, and contact spatial topologies. In particular, the very challenging region of grain-to-grain contact and particle morphology can now be accurately resolved (to within imaging resolution) using the level set method [47]. The transition from this information to discrete models and computations is the next logical step.

The research objective is therefore to devise a new DEM that can account for particle morphological features that have already been captured in the image data and that are necessary to make discrete computations predictive. Below, we list the components required to meet this research objective.

- 1. Geometry basis.** The development of a new DEM requires the choice of a basis for representing particle geometries. Based on promising results from the realm of isogeometric analysis [48], Non-Uniform Rational Basis-Splines (NURBS) was experimented with. In the context of granular simulations, NURBS provides great flexi-

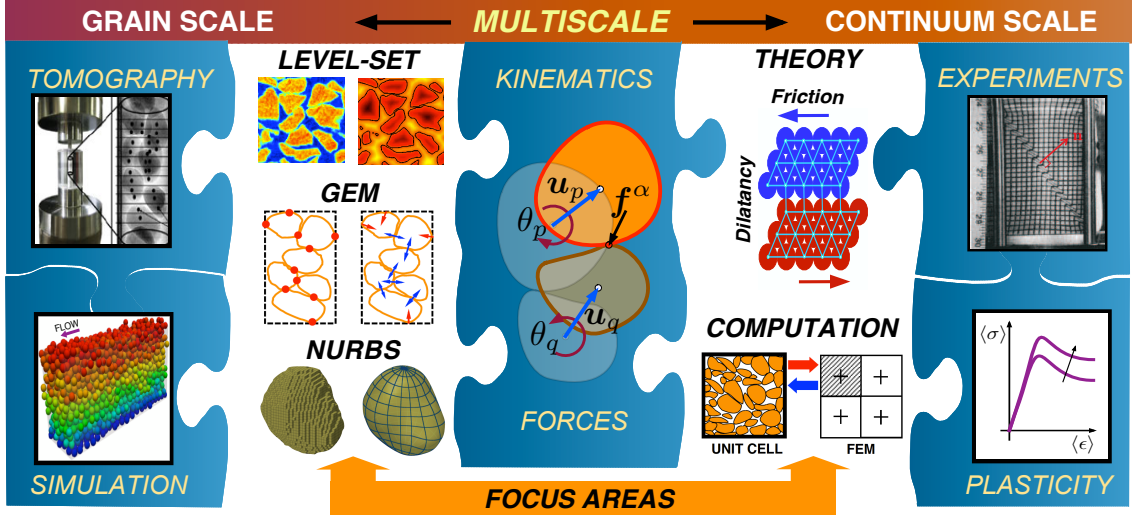


Figure 1.2: Schematic showing unified tomography-to-simulation framework across scales (left to right) and integration of characterization and simulation (top to bottom). Areas of relatively established understanding (shown in solid puzzle pieces), such as grain-scale tomography and simulation, are contrasted with focus areas that are in active development. Level sets, GEM [2; 3], and NURBS are key computational ingredients to enabling grain-scale characterization and simulations, which yield particle kinematics and forces. Using such quantities, multiscale methods provide the link between experiments and continuum plasticity models to complete the proposed framework (after [4]).

bility in representing arbitrary and complex geometries with much less information than conventional faceted or polygonal counterparts. The idea of using NURBS for representing grain geometry is shown in Figure 1.3, which shows an example of a sand particle imaged with 3D X-ray CT, with thousands of voxels used to render morphology (roundness and angularity) accurately, as well as the concept of seamlessly transitioning from binary image data in (a) to a smooth functional representation using NURBS in (c). The intermediate figure in (b) shows the control mesh furnished by the so-called NURBS control points.

2. **Contact algorithm.** The contact algorithm is one of the major components of DEM. Here, the quantity that needs to be determined is the signed gap or penetration, which is subsequently used in the calculation of the normal contact force. The major difficulty in using NURBS is that there is a separation between the control points and actual curve or surface. Therefore, there are no vertices or facets to simplify the determination of the signed gap. In addition, the process is necessarily iterative

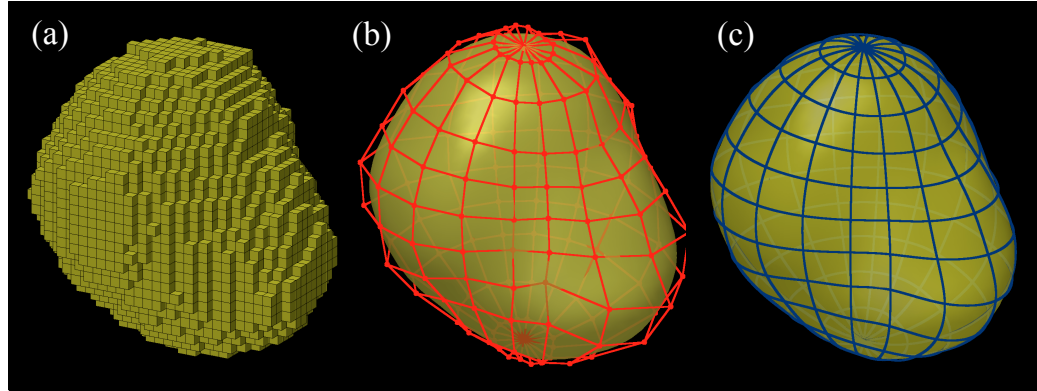


Figure 1.3: Using NURBS as a representation for grain morphology.

because of the generally nonlinear nature of parametric curves and surfaces. The challenge here is to devise a methodology that can take advantage of the parametric nature of NURBS to compute the signed gap or penetration between two non-convex NURBS surfaces.

3. **Time integration.** While this component is not related to particle morphology, it needs to be improved for practical reasons. It is well known that **explicit** algorithms used in classic DEM lead to very small time steps when nearly rigid particles (e.g., sand) are modeled. Here, a contact dynamics (CD) approach is desirable since the equations of motions and constraints are considered **implicitly**, allowing the use of larger time steps. Current CD approaches, however, are fairly difficult to implement and here, we seek a simpler CD formulation that would remedy this difficulty.
4. **Application with real particle geometries.** As a new DEM that aims to bring grain-scale characterization and modeling to a real application level, it needs to be assessed experimentally. In the past, we have characterized internal variables such as dilatancy and residual strength in shear bands using experimental data. As a first grain-scale application of our new DEM, we will attempt to numerically reproduce these experimentally-inferred internal variables. For this work, X-ray CT experimental data can be obtained from our collaborators at the University of Grenoble, France.

1.4 Contribution

The contribution of the work described in this thesis is the development of a new DEM that has enabled the seamless transition from X-ray CT image data to discrete computations, and in this process has allowed for the capturing sphericity and roundness, the two morphological measures that are used in characterizing real particle geometries. We have applied the new DEM to characterize and model the shear band response in a real triaxial specimen in which we have obtained a consistent set of internal variables — dilatancy and residual strength — between experiment and discrete simulation, providing the first complete link between grain-scale experiment and modeling in the tomography-to-simulation framework.

1.5 Overview of Thesis

This thesis is organized as follows: Chapter 2 covers some fundamental background concerning discrete methods, namely, their governing equations, time integration approaches, shape representation techniques and the current state of affairs of these methods in terms of granular materials modeling.

In Chapter 3, the details of our NURBS-based DEM is presented. In particular, the basics of NURBS are explained and the solution of the closest-point projection of a point on a NURBS surface through the Lipschitzian dividing rectangle (DIRECT) global optimization algorithm is described. The latter development is crucial to enabling the contact treatment of arbitrary-shaped non-convex particles, as well as making the implementation of the new DEM simple and robust.

In Chapter 4, a CD approach to our NURBS-based discrete method is presented. By combining particle shape flexibility, properties of implicit time integration (e.g., larger time steps) and non-penetrating constraints, as well as a reduction to a static formulation in the limit of an infinite time step), we target applications in which the classical DEM either performs poorly or simply fails, i.e., in granular systems comprising rigid or highly stiff angular particles and subjected to quasi-static or dynamic flow conditions.

Chapter 5 presents an application of the new DEM within a computational mechanics avatar framework in which a quantitative comparison of microscopic quantities from discrete simulation and experiment is made. This is the first attempt at using a discrete model inferred from real grain-level XRCT data to study the response of a real macroscopic triaxial

specimen.

Finally, Chapter 6 summarizes some key developments of this dissertation. Limitations of the current work are also discussed and future directions of research are outlined.

This thesis is based on a number of papers [4; 49–52]. To make this thesis flow better, content repetition is minimized as much as possible. In certain chapters (e.g., Chapter 5), however, there will be some repetition of concepts, equations, and ideas, as these chapters are in the process of being published as individual journal articles.

Chapter 2

Discrete Methods

In this chapter, we review the procedures used in the classic discrete element method and contact dynamics to determine the contact forces and particle kinematics.

2.1 Discrete Element Method

The two defining features of the classic DEM [24] are particle deformability and the use of an explicit time integration algorithm to resolve particle collisions. Here, particle deformability refers to use of springs to model the contact forces, which act only when there is particle overlap. These two features imply that the time step must be smaller than the elastic response time for numerical stability. In this section, we discuss these two features in detail.

2.1.1 Normal force and associated moments

To show how the contact forces are calculated, we can focus on the case of single cohesionless contact between two particles. Consider a grain Ω^i with a potentially contacting neighbor grain Ω^j , as shown in Figure 2.1. The effective normal contact force on grain Ω^i at the contact point is calculated using a linear elastic stiffness model such that

$$\mathbf{f}_n^i = \begin{cases} k_N g \mathbf{n}, & \text{if } g < 0 \\ \mathbf{0}, & \text{otherwise} \end{cases} \quad (2.1)$$

where k_N is the normal elastic stiffness and $g \mathbf{n}$ measures the penetration or overlap in vector form, determined by some contact algorithm (e.g., the closest point projection operation

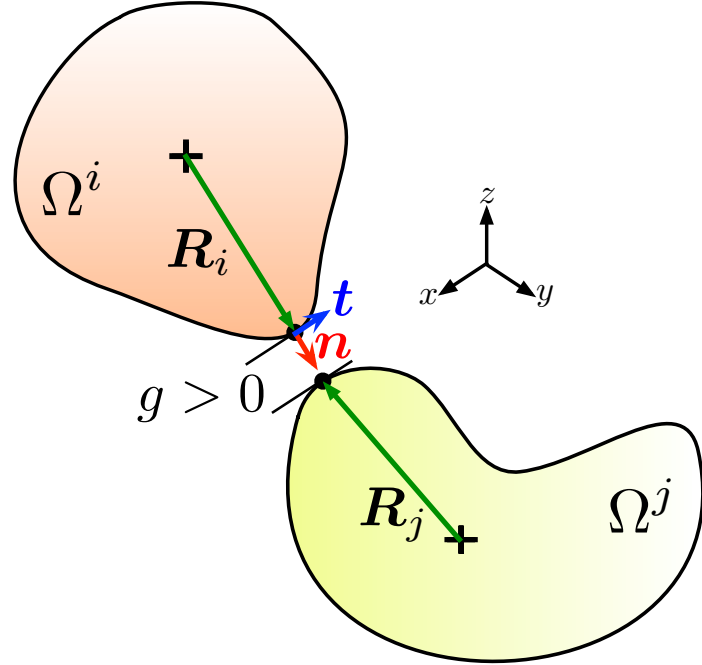


Figure 2.1: Illustration of two particles (Ω^i and Ω^j) that are potentially contacting. The gap g between the particles is positive if the particles are separated, and negative if the particles overlap. The moment arms emanating from each particle's centroid to its corresponding contact point are denoted by \mathbf{R}_i and \mathbf{R}_j for Ω^i and Ω^j , respectively.

described in Chapter 3). The sign convention used is that the normal vector \mathbf{n} points away from the grain of interest, which means that $g \mathbf{n}$ with $g < 0$ has a direction pointing toward grain Ω^i . By action and reaction, the effective normal contact force on grain Ω^j contacting with grain Ω^i is then

$$\mathbf{f}_n^j = -\mathbf{f}_n^i \quad (2.2)$$

Denoting the moment arm extending from the centroid of grain Ω^i to the contact point by \mathbf{R}_i , the moment due to normal force is calculated as

$$\mathbf{m}_n^i = \mathbf{R}_i \times \mathbf{f}_n^i \quad (2.3)$$

Similarly, the moment due to normal force on the contacting grain Ω^j is

$$\mathbf{m}_n^j = \mathbf{R}_j \times \mathbf{f}_n^j \quad (2.4)$$

where \mathbf{R}_j is the moment arm extending from the centroid of grain Ω^j to the contact point.

Remark 2.1.1 In the case of disks or spheres, the signed gap g is calculated as

$$g = R_i + R_j - \|\mathbf{x}_i - \mathbf{x}_j\| \quad (2.5)$$

where R_i and R_j are the radii of particles i and j , respectively. The corresponding particle centroids are \mathbf{x}_i and \mathbf{x}_j .

2.1.2 Tangential force and associated moments

For simplicity, the incremental tangential forces are calculated here using the simple Coulomb friction model proposed in [24; 53]. In this model, the tangential stiffness is initialized at time of first contact and exists until the grains separate. The velocity of grain Ω^i relative to grain Ω^j at the contact point is calculated as

$$\mathbf{v}_{\text{rel}} = \mathbf{v}^i + \boldsymbol{\omega}^i \times \mathbf{R}_i - \mathbf{v}^j - \boldsymbol{\omega}^j \times \mathbf{R}_j \quad (2.6)$$

where \mathbf{v}^i and \mathbf{v}^j are the translational velocities, and $\boldsymbol{\omega}^i$ and $\boldsymbol{\omega}^j$ are the angular velocities in global coordinate frame of grains Ω^i and Ω^j , respectively. We then calculate the incremental displacement as

$$\Delta \mathbf{u} = \mathbf{v}_{\text{rel}} \Delta t \quad (2.7)$$

The increment in shear force on grain Ω^i is calculated as

$$\Delta \mathbf{f}_s^i = -k_T \Delta \mathbf{s} \quad (2.8)$$

where k_T is the shear spring stiffness and

$$\Delta \mathbf{s} = \Delta \mathbf{u} - (\Delta \mathbf{u} \cdot \mathbf{n}) \mathbf{n} \quad (2.9)$$

is the tangential incremental displacement obtained by projecting the incremental displacement in the tangential direction. By action and reaction, the increment in shear force on grain Ω^j is

$$\Delta \mathbf{f}_t^j = -\Delta \mathbf{f}_t^i \quad (2.10)$$

Before the previous shear force can be updated, it needs to be corrected to account for the incremental rotation of the contact plane. The previous shear force vector at the contact point on grain Ω^i is first corrected as

$$\text{define as // incorrect use here} \\ \mathbf{f}_t^i := \mathbf{Z} \mathbf{f}_t^i \quad (2.11)$$

where \mathbf{Z} is the rotation matrix that rotates the previous normal vector \mathbf{n}^{prev} to the current normal vector \mathbf{n} . The shear force on grain Ω^i is updated as

Rotation matrix between 2 vectors: <https://math.stackexchange.com/questions/180418/calculate-rotation-matrix-to-align-vector-a-to-vector-b-in-3d>

$$\mathbf{f}_t^i := \mathbf{f}_t^i + \Delta \mathbf{f}_t^i \quad (2.12)$$

and then capped as

$$\mathbf{f}_t^i := \mathbf{f}_t^i \left(\frac{f_{\max}}{\|\mathbf{f}_t^i\|} \right) \quad (2.13)$$

where

$$f_{\max} = \|\mathbf{f}_n^i\| \tan \phi \quad (2.14)$$

with ϕ being the interparticle friction angle. Again, by action and reaction, the shear force on grain Ω^j contacting with grain Ω^i is

$$\mathbf{f}_t^j = -\mathbf{f}_t^i \quad (2.15)$$

Finally, the corresponding moments associated with the tangential forces are

$$\mathbf{m}_t^i = \mathbf{R}_i \times \mathbf{f}_t^i \quad (2.16)$$

$$\mathbf{m}_t^j = \mathbf{R}_j \times \mathbf{f}_t^j \quad (2.17)$$

for grains Ω^i and Ω^j , respectively.

2.1.3 Discrete equations of motion

In DEM, the equations of motion are integrated explicitly, particle-by-particle, using information from the previous time step. As such, in discussing the discrete equations of motion, we can focus on an individual particle. We assume that the resultant force and moment, obtained from summing all the forces and moments induced by contact interactions between

the particle and its contacting neighbors, are given. We first consider the translational components. The equation governing translational motion of the grain's center of mass is given by Newton's law:

$$M a_i + C v_i = F_i \quad (2.18)$$

where $i = 1, 2, 3$ in three dimensions, M is the mass of the grain, and $C = \xi M$ is the damping, which proportionally scales the linear velocity v_i , with ξ being the global damping parameter. The linear acceleration is given by a_i and is related to the resultant force F_i . To integrate the translational components of motion, we employ the centered finite-difference integration scheme proposed in [24]: Cundall 1979

$$v_i^{n+1/2} = \frac{1}{1 + \xi \Delta t / 2} \left[(1 - \xi \Delta t / 2) v_i^{n-1/2} + \frac{\Delta t}{M} F_i \right] \quad (2.19)$$

$$x_i^{n+1} = x_i^n + \Delta t v_i^{n+1/2} \quad (2.20)$$

The control points of the NURBS patches in the grain are then translated by displacements according to $\Delta t v_i^{n+1/2}$.

For the 2D case, the discrete equations for integrating the rotational degree of freedom are analogous to those for the translations. For 3D, however, this is not the case. For the rotational components of motion in 3D, it is convenient to work in principal body-fixed frame. For the rest of this section, unless noted otherwise, we work with quantities that are defined with respect to the principal body-fixed frame. Consider the angular accelerations α_i given through the Euler's equations of motion as

$$\alpha_1 = [m_1 + \omega_2 \omega_3 (J_2 - J_3) - \xi J_1 \omega_1] / J_1 \quad (2.21)$$

$$\alpha_2 = [m_2 + \omega_3 \omega_1 (J_3 - J_1) - \xi J_2 \omega_2] / J_2 \quad (2.22)$$

$$\alpha_3 = [m_3 + \omega_1 \omega_2 (J_1 - J_2) - \xi J_3 \omega_3] / J_3 \quad (2.23)$$

where ω_i for $i = 1, 2, 3$ are the angular velocities, m_i are the moments, and J_i are the principal moments of inertia. Here, inertia-proportional damping is included via the global damping parameter ξ . The Euler equations are nonlinear due to the presence of the products of angular velocities on the right hand side. Therefore, to appropriately integrate the

rotational components of motion, we use a predictor-corrector algorithm proposed in [54], which can be described in the following steps:

1. Estimate the angular velocities at the current time step by assuming constant angular acceleration for an additional half step:

$$\omega_i'^n = \omega_i^{n-\frac{1}{2}} + \frac{1}{2} \Delta\omega_i^{n-1} \quad (2.24)$$

where $\Delta\omega_i^{n-1} = \alpha_i^{n-1} \Delta t$.

2. Calculate angular velocity predictors using the above estimates:

$$\Delta\omega_1'^n = \Delta t \left[m_1^n + \omega_2'^n \omega_3'^n (J_2 - J_3) - \xi J_1 \omega_1'^n \right] / J_1 \quad (2.25)$$

$$\Delta\omega_2'^n = \Delta t \left[m_2^n + \omega_3'^n \omega_1'^n (J_3 - J_1) - \xi J_2 \omega_2'^n \right] / J_2 \quad (2.26)$$

$$\Delta\omega_3'^n = \Delta t \left[m_3^n + \omega_1'^n \omega_2'^n (J_1 - J_2) - \xi J_3 \omega_3'^n \right] / J_3 \quad (2.27)$$

3. Predict angular velocities at the current time step:

$$\omega_i^n = \omega_i^{n-\frac{1}{2}} + \frac{1}{2} \Delta\omega_i'^n \quad (2.28)$$

4. Calculate angular velocity correctors:

$$\Delta\omega_1^n = \Delta t \left[m_1^n + \omega_2^n \omega_3^n (J_2 - J_3) - \xi J_1 \omega_1^n \right] / J_1 \quad (2.29)$$

$$\Delta\omega_2^n = \Delta t \left[m_2^n + \omega_3^n \omega_1^n (J_3 - J_1) - \xi J_2 \omega_2^n \right] / J_2 \quad (2.30)$$

$$\Delta\omega_3^n = \Delta t \left[m_3^n + \omega_1^n \omega_2^n (J_1 - J_2) - \xi J_3 \omega_3^n \right] / J_3 \quad (2.31)$$

Additional iterations are performed by repeating steps 1 through 4 until the correctors converge to some desired tolerance.

5. Update angular velocities using the correctors:

$$\omega_i^{n+\frac{1}{2}} = \omega_i^{n-\frac{1}{2}} + \Delta\omega_i^n \quad (2.32)$$

For small time steps used to resolve the interparticle contacts and for quasi-static conditions

in which the angular velocities are small, the number of iterations is typically small. Usually, between 3 and 5 iterations are required to achieve machine precision tolerance.

After obtaining the angular velocities, the orientation of the principal body-fixed frame is updated using the singularity-free quaternion approach in [55], which is described as follows. The rotation matrix that transforms vectors in global space to vectors in body frame is given by

$$\mathbf{A} = \begin{pmatrix} -q_1^2 + q_2^2 - q_3^2 + q_4^2 & -2(q_1 q_2 - q_3 q_4) & 2(q_2 q_3 + q_1 q_4) \\ -2(q_1 q_2 + q_3 q_4) & q_1^2 - q_2^2 - q_3^2 + q_4^2 & -2(q_1 q_3 - q_2 q_4) \\ 2(q_2 q_3 - q_1 q_4) & -2(q_1 q_3 + q_2 q_4) & -q_1^2 - q_2^2 + q_3^2 + q_4^2 \end{pmatrix} \quad (2.33)$$

where the q_i 's are the quaternions defined by

$$q_1 = \sin\left(\frac{\theta}{2}\right) \sin\left(\frac{\psi - \phi}{2}\right) \quad (2.34)$$

$$q_2 = \sin\left(\frac{\theta}{2}\right) \cos\left(\frac{\psi - \phi}{2}\right) \quad (2.35)$$

$$q_3 = \cos\left(\frac{\theta}{2}\right) \sin\left(\frac{\psi + \phi}{2}\right) \quad (2.36)$$

$$q_4 = \cos\left(\frac{\theta}{2}\right) \cos\left(\frac{\psi + \phi}{2}\right) \quad (2.37)$$

and ϕ , θ , and ψ are the Euler angles in the $z'x'z'$ notational convention [56]. The initial values of the quaternions are calculated using the initial configurations of the grains before the start of the simulation.

The time derivatives of the quaternions can be expressed in terms of products of the quaternions with the angular velocities as a singularity-free set of equations:

$$\begin{pmatrix} \dot{q}_1 \\ \dot{q}_2 \\ \dot{q}_3 \\ \dot{q}_4 \end{pmatrix} = \frac{1}{2} \begin{pmatrix} -q_3 & -q_4 & q_2 \\ q_4 & -q_3 & -q_1 \\ q_1 & q_2 & q_4 \\ -q_2 & q_1 & -q_3 \end{pmatrix} \begin{pmatrix} \omega_1 \\ \omega_2 \\ \omega_3 \end{pmatrix} \quad (2.38)$$

with closure of the above system given by the normalization relation

$$\sum_{i=1}^4 q_i = 1 \quad (2.39)$$

The above system of equations can be solved using an explicit finite difference scheme [54], which results in the following update equation:

$$\mathbf{q}^{n+1} = \mathbf{B}^{-1} \mathbf{B}^T \mathbf{q}^n \quad (2.40)$$

where

$$\mathbf{q}^n = \begin{pmatrix} q_1^n \\ q_2^n \\ q_3^n \\ q_4^n \end{pmatrix}, \quad \mathbf{B} = \begin{pmatrix} 1 & -\beta_3 & \beta_1 & \beta_2 \\ \beta_3 & 1 & \beta_2 & -\beta_1 \\ -\beta_1 & -\beta_2 & 1 & -\beta_3 \\ -\beta_2 & \beta_1 & \beta_3 & 1 \end{pmatrix} \quad (2.41)$$

and

$$\beta_i = \frac{\Delta t}{4} \omega_i^{n+\frac{1}{2}} \quad (2.42)$$

and where \square^T is the transpose operator. We note that equation (2.40) can be solved in closed form as described in [54]. It has been shown in [55] that equation (2.38) maintains the orthogonality relation of equation (2.39). Normalization of the quaternions, however, is performed after each integration step to prevent normalization failure resulting from round-off error.

The matrix \mathbf{A}^{n+1} of equation (2.33) at t_{n+1} can be evaluated using the quaternions in \mathbf{q}^{n+1} . The updated orientation (triads) of the principal body-fixed frame is then given by the rows \mathbf{A}^{n+1} . The required rotation matrix for rotating the particle about its center of mass is obtained as

$$\boldsymbol{\Pi}^{n+1} = \mathbf{A}^{n+1 T} \mathbf{A}^n \quad (2.43)$$

In the next calculation cycle, the moments on each grain due to interparticle contact, calculated in the global frame, are transformed into the principal body-fixed frame using \mathbf{A}^{n+1} .

Damping is used to achieve quasi-static conditions by utilizing the so-called dynamic relaxation, which allows the dissipation of accelerations, hence making all resulting forces

vanish, achieving in this way static equilibrium [57].

Verification tests on the classic DEM are shown in Appendix A.1.

2.2 Contact Dynamics

In contrast with DEM, CD considers the deformation of the granular medium as a whole, determined exclusively by geometric rearrangements of rigid particles [58]. The CD formulation appears to originate from the works of Lötstedt [59; 60], which provide the formulation of the contact problem between rigid bodies as a linear complementarity problem (LCP). Further analysis and development of solution procedures by Moreau [61] and Jean [62] led to the introduction of CD to the granular materials research community.

In this section, we provide the basics of CD and highlight the major differences between CD and DEM. For simplicity, we will work under the assumption of near quasi-static conditions in which the angular velocities are small. In this case, the terms containing products of angular velocities in equation (2.23) are neglected. In addition, for the purpose of illustrating the time integration scheme, we will assume that the coefficient of restitution between two particles is zero. This assumption can be shown to correspond to the fully implicit or backward Euler scheme (see Chapter 4).

The rigidity of the particles requires that the non-penetration constraint is enforced between particles. This constraint is embodied in the non-smooth graph of normal reaction force versus the gap or separation between two particles, as shown in Figure 2.2(a). The non-

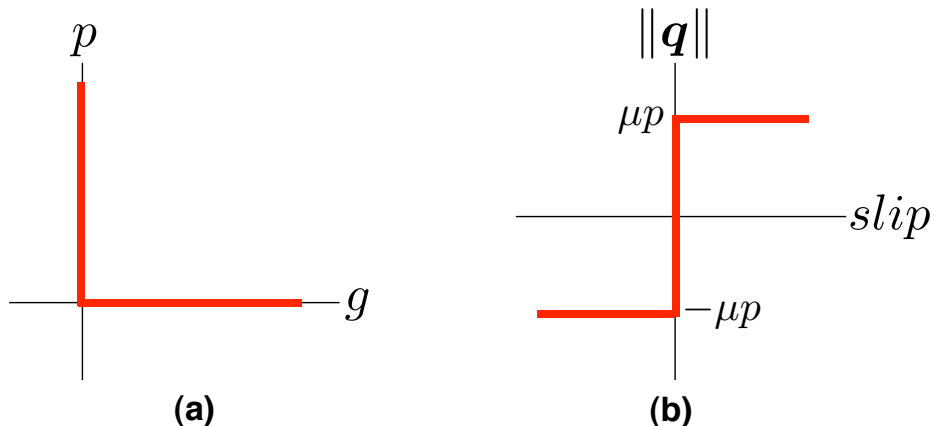


Figure 2.2: Graph of non-smooth contact laws: (a) normal reaction force p against separation or gap g and (b) friction force $\|q\|$ against slip; μ is the friction coefficient.

penetration constraint is sometimes described as unilateral, which means that the normal reaction is active when the gap is zero and is zero otherwise. In addition, a non-sliding constraint of frictional contacts is required. The most basic of such constraint is given by the Coulomb threshold, as shown in Figure 2.2(b).

To explain the single-contact update procedure, consider the following generalized velocity and force vectors:

$$\mathbf{V} = \begin{pmatrix} \mathbf{v}^i \\ \boldsymbol{\omega}^i \\ \mathbf{v}^j \\ \boldsymbol{\omega}^j \end{pmatrix} \quad (2.44)$$

$$\boldsymbol{\Lambda} = \begin{pmatrix} \boldsymbol{\lambda} \\ \mathbf{R}_i \times \boldsymbol{\lambda} \\ -\boldsymbol{\lambda} \\ -\mathbf{R}_j \times \boldsymbol{\lambda} \end{pmatrix} \quad (2.45)$$

where $\boldsymbol{\lambda}$ is the yet to be determined constraint force, and $\mathbf{R}_i, \mathbf{R}_j$ are again the moment arms, as shown in Figure 2.1. We can reexpress equations (2.45) in linear form as

$$\boldsymbol{\Lambda} = \begin{pmatrix} \mathbf{I} \\ -\mathbf{R}_i \\ -\mathbf{I} \\ \mathbf{R}_j \end{pmatrix} \boldsymbol{\lambda} = \mathbf{H} \boldsymbol{\lambda} \quad (2.46)$$

where \mathbf{R}_i is the matrix containing the components of the radius vector \mathbf{R}_i arranged in the form

$$\mathbf{R}_i = \begin{bmatrix} 0 & -R_{i,3} & R_{i,2} \\ R_{i,3} & 0 & -R_{i,1} \\ -R_{i,2} & R_{i,1} & 0 \end{bmatrix} \quad (2.47)$$

The relative velocity (2.6) can then be written as

$$\mathbf{v}_{\text{rel}} = \mathbf{H}^T \mathbf{V} \quad (2.48)$$

The equations of motion for the two interacting particles are given by

$$\frac{d\mathbf{V}}{dt} = \mathbf{M}_{\text{eff}}^{-1} (\mathbf{\Lambda} + \mathbf{F}_{\text{ext}}) \quad (2.49)$$

where \mathbf{M}_{eff} is the effective mass matrix given by

$$\mathbf{M}_{\text{eff}} = \begin{bmatrix} m^i \mathbf{1} & 0 & 0 & 0 \\ 0 & J^i \mathbf{1} & 0 & 0 \\ 0 & 0 & m^j \mathbf{1} & 0 \\ 0 & 0 & 0 & J^j \mathbf{1} \end{bmatrix} \quad (2.50)$$

and \mathbf{F}_{ext} is the generalized external load vector containing the external translational forces and moments acting on the particles. Using equations (2.46) and (2.48), we can rewrite (2.49) as

$$\frac{d\mathbf{v}_{\text{rel}}}{dt} = \mathbf{H}^T \mathbf{M}_{\text{eff}}^{-1} \mathbf{H} \boldsymbol{\lambda} + \frac{d\mathbf{v}_{\text{free}}}{dt} \quad (2.51)$$

where

$$\frac{d\mathbf{v}_{\text{free}}}{dt} = \mathbf{H}^T \mathbf{M}^{-1} \mathbf{F}_{\text{ext}} \quad (2.52)$$

is the acceleration without any interaction between the particles.

Discretizing equation (2.51) using a backward Euler scheme gives the discrete equation corresponding to equation (2.51) as

$$\frac{\mathbf{v}_{\text{rel}} - \mathbf{v}_{\text{free}}}{\Delta t} = \mathbf{H}^T \mathbf{M}_{\text{eff}}^{-1} \mathbf{H} \boldsymbol{\lambda} \quad (2.53)$$

with the new velocity without any interaction between the particles calculated as

$$\mathbf{v}_{\text{free}} = \mathbf{v}_{\text{rel}}^0 + \mathbf{H}^T \mathbf{M}^{-1} \mathbf{F}_{\text{ext}} \Delta t \quad (2.54)$$

where the quantities $\boldsymbol{\lambda}$ and \mathbf{v}_{rel} are unknowns and $\mathbf{v}_{\text{rel}}^0$ is the known relative velocity from the previous time step. To determine the unknowns, the steps in Algorithm 1 are applied.

- 1: Check if gap is open after one time step: $g + \Delta t \mathbf{v}_{\text{free}} \cdot \mathbf{n} > 0$? Yes, set $\boldsymbol{\lambda} = \mathbf{0}$ and $\mathbf{v}_{\text{rel}} = \mathbf{v}_{\text{free}}$ and exit. No, go to next step.
- 2: Compute new relative velocity assuming gap is closed: $g + \Delta t \mathbf{v}_{\text{rel}} \cdot \mathbf{n} = 0$. Assume non-sliding contact, i.e., zero tangential velocity $\mathbf{v}_{t\text{rel}} = \mathbf{0}$. Let $\mathbf{v}_{\text{rel}} = -(g/\Delta t)\mathbf{n}$. Compute:
 - Constraint force $\boldsymbol{\lambda}$ from equation (2.53)
 - Contact normal force $p = \boldsymbol{\lambda} \cdot \mathbf{n}$
 - Contact shear force $\mathbf{q} = \boldsymbol{\lambda} - p\mathbf{n}$
 Check Coulomb threshold: $\|\mathbf{q}\| \leq \mu p$? Yes, accept \mathbf{v}_{rel} , $\boldsymbol{\lambda}$ and exit. No, go to next step.
- 3: Gap is still closed $f = 0$ but $\mathbf{v}_{t\text{rel}} \neq \mathbf{0}$. Let $\mathbf{v}_{\text{rel}} = -(g/\Delta t)\mathbf{n} + \mathbf{v}_{t\text{rel}}$. Solve equation (2.53) for $\boldsymbol{\lambda}$ and $\mathbf{v}_{t\text{rel}}$ subject to:

$$\mathbf{q} = -\mu p \frac{\mathbf{v}_{t\text{rel}}}{\|\mathbf{v}_{t\text{rel}}\|}$$

Algorithm 1: Single-Contact Update Algorithm

Remark 2.2.1 Algorithm 1 is reminiscent of the return mapping algorithm used for elasto-plasticity constitutive updates [63].

We note that Algorithm 1 applies only to the single-contact case. In general, the multi-contact case applies, in which case the generalized load vector includes constraint forces and moments from neighboring contacts. It can then be shown that the resulting global equilibrium equation resembles a Laplace-type equation that couples all the constraint forces and moments, and hence these cannot be computed locally. Moreover, these constraint forces need to satisfy the non-penetration and non-sliding constraints at every contact. An iterative scheme is applied within each time step to obtain a globally consistent set of forces satisfying all the required constraints. In each iteration, a contact is selected and updated based on the contact law for the single-contact case, independent of the other contacts. The selection of contact for update is performed randomly through either a sweep or sequentially over the contact set. In the case of a random sweep, each contact is selected exactly once within the iteration while for the random sequential update, the same contact could be selected more than once. The iterative procedure causes a relaxation of forces to a globally consistent solution analogous to the behavior of information spreading in a diffusive (heat)

system. For a system with rigid particles, the number of unknowns in general exceeds the number of equilibrium equations. As such, there could be more than one globally consistent solution to the system. Therefore, it is crucial that the selection of contacts avoids any bias in information spreading in the system during the relaxation process.

Alternatively, the coupling of all the constraint forces and moments can be dealt with by directly solving the mixed LCP associated with the discrete update equations and contact constraints [64–68]. While small instances of LCPs often can be solved efficiently by means of pivot based algorithms such as that of Lemke [69], methods for larger problems still lag far behind current convex program solvers [70], e.g., second-order cone programs (SOCPs), as far as efficiency and robustness are concerned. Newton-based algorithms for LCP have also been developed [71] and although these methods in principle offer the same advantages as their convex programming counterparts, their performance has been shown to be highly problem dependent and convergence is generally not guaranteed. Moreover, while convex programs admit a straightforward analysis of existence and uniqueness properties (and most implementations automatically detect infeasibility, i.e., non-existence), LCPs are in general much harder to gauge with respect to these properties. This leads to a situation where one is unable to distinguish between algorithmic failure and non-existence of solutions [72].

In general, the implementation of solution procedures for CD is quite complicated and this remains the primary reason why CD has not been widely adopted by the granular research community despite favorable performance that has been shown through a number of studies [73–83]. In Chapter 4, we present a new formulation of CD that is numerically more palatable and significantly easier to implement.

Chapter 3

NURBS-based Discrete Element Method

The two major components of the proposed NURBS-based DEM are the use of NURBS for representing particle geometries, and the contact algorithm for determining the signed gap or penetration between two non-convex NURBS surfaces. We discuss these two components in detail in this chapter.

3.1 Non-Uniform Rational Basis-Splines (NURBS)

Non-Uniform Rational Basis-Splines (NURBS) are ubiquitous in the world of computer graphics, computer-aided design (CAD), computer-aided engineering (CAE), and computer-aided manufacturing (CAM) systems, as well as in computer animations. These functions provide great flexibility in representing arbitrary and complex geometries with much less information than conventional faceted or polynomial counterparts. Perhaps more importantly, in the context of this work and as shown in this section, the mathematical properties of NURBS make them ideal candidates for the description of grain morphology, the integration of discrete equations of motion, and the detection of contact.

In what follows we briefly describe the essential components of NURBS in the context of the current application. The literature on NURBS is extensive and relatively mature, and our purpose here is not to present all of its elements but rather those that are needed for completeness of presentation. For an exhaustive description of NURBS the reader is referred to [48; 84–86], whose presentation and notational convention we follow closely. We adhere to the convention in the computational geometry literature where the degree

$p = 1, 2, 3$, etc. refers to constant, linear, quadratic, cubic, etc., piecewise polynomials, respectively. In the following incomplete description of NURBS, we split the acronym into three parts: Non-Uniform (NU), Rational (R), and Basis-Splines (BS). We describe these parts in reverse order and incrementally for clarity of presentation.

3.1.1 Basis-Splines (BS)

Within the description of Basis-Splines (B-Splines), there are three main elements necessitated [86]:

1. A set of $n + 1$ control points \mathbf{P}_i ($0 \leq i \leq n$),
2. A knot vector U of $m + 1$ knots ($0 = u_0 \leq u_1 \leq \dots \leq u_{m-1} \leq u_m = 1$), and
3. A degree p satisfying $m = n + o$ where $o = p + 1$ is the order of the curve.

Note that the last requirement means that the number of knots $m + 1$ must be equal to the number of control points $n + 1$ plus the curve order $p + 1$. The control points need not lie on the curve itself. Rather, control points act as a scaffold that controls the geometry [48]. At the most rudimentary level, one manipulates the geometry by adjusting the control points until the desired shape is met. Piecewise linear interpolation of the control points effectively furnishes a control polygon bounding the geometry.

Given the aforementioned parameters, a (non-rational, polynomial) B-Spline curve is defined parametrically as

$$\mathbf{C}(u) = \sum_{i=0}^n N_{i,p}(u) \mathbf{P}_i \quad (3.1)$$

where u is the curve parameter, and $N_{i,p}$ is the i -th B-Spline basis function of degree p defined recursively as follows:

NOTE:

1. T-spline is used very often in Rhino design, check it

2. NURBS will have crack at seams when deformed (CS418 ppt NO.33), watch out

$$N_{i,0}(u) = \begin{cases} 1 & \text{if } u \in [u_i, u_{i+1}) \\ 0 & \text{otherwise} \end{cases}$$

$$N_{i,p}(u) = \frac{u - u_i}{u_{i+p} - u_i} N_{i,p-1}(u) + \frac{u_{i+p+1} - u}{u_{i+p+1} - u_{i+p}} N_{i+1,p-1}(u) \quad (3.2)$$

The above is also known as the Cox-de Boor recursion formula [87; 88].

de Boor's algorithms for B-Spline is a generalization of de Casteljau's algorithm for Bezier curve. It is fast and numerically stable.

Webpage:

<http://pages.mtu.edu/~shene/COURSES/cs3621/NOTES/>

<https://www.qiujiawei.com/b-spline-1/>

<https://blog.csdn.net/brightming/article/details/53953926>

<https://www.zhihu.com/question/30211038>

SISL NURBS library: <https://github.com/SINTEF-Geometry/SISL>

3.1.2 Rational B-Splines (RBS)

A known limitation of (non-rational) B-Splines, as defined in equation (3.1), is their inability to capture conic sections (e.g., circles and ellipses). This limitation stems from the simple polynomial form of B-Splines. To be able to represent conic sections, the parametric form would need to be *rational*, i.e., the quotient of two polynomials. A rational B-Spline (RBS) is furnished by adding a weight $w_i \geq 0$, which provides an additional degree of freedom for geometry manipulation. Hence, the curve equation becomes

$$\mathbf{C}(u) = \frac{\sum_{i=0}^n N_{i,p}(u) w_i \mathbf{P}_i}{\sum_{i=0}^n N_{i,p}(u) w_i} \quad (3.3)$$

$$= \sum_{i=0}^n R_{i,p}(u) \mathbf{P}_i \quad (3.4)$$

where $R_{i,p}(u) = N_{i,p}(u) w_i / (\sum_{i=0}^n N_{i,p}(u) w_i)$, $0 \leq i \leq n$, are the rational basis functions. Since $R_{i,p}(u)$ is rational, the exact description of conic sections becomes possible. Naturally, when all weights are equal to unity, equation (3.4) reduces to equation (3.1).

It is interesting to note the geometric contribution of the weights. The weight w_k affects the effective contribution of control point \mathbf{P}_k on the overall shape of the curve $\mathbf{C}(u)$. Making w_k smaller corresponds to ‘pushing’ the curve away from the control point \mathbf{P}_k . In the extreme, when $w_k = 0$, the term $w_k \mathbf{P}_k$ is annihilated from the equation of the curve and the contribution of the control point is obviously nullified. Another interesting extreme is obtained by making w_k very large relative to other weights. Dividing equation (3.4) by w_k gives

$$\mathbf{C}(u) = \frac{\sum_{i \neq k}^n N_{i,p}(u) w_i / w_k \mathbf{P}_i + N_{k,p}(u) \mathbf{P}_k}{\sum_{i \neq k}^n N_{i,p}(u) w_i / w_k + N_{k,p}(u)} \quad (3.5)$$

where one can see that as w_k is increased, the curve $\mathbf{C}(u)$ is ‘pulled’ towards the control point \mathbf{P}_k .

Remark 3.1.1 *In the context of grain modeling, the inability of non-rational B-Splines to represent conic sections should not be viewed as a disadvantage, since real grains are rarely spherical or circular in section. NURBS can be used in their simpler polynomial B-spline version when their full power is not necessary.*

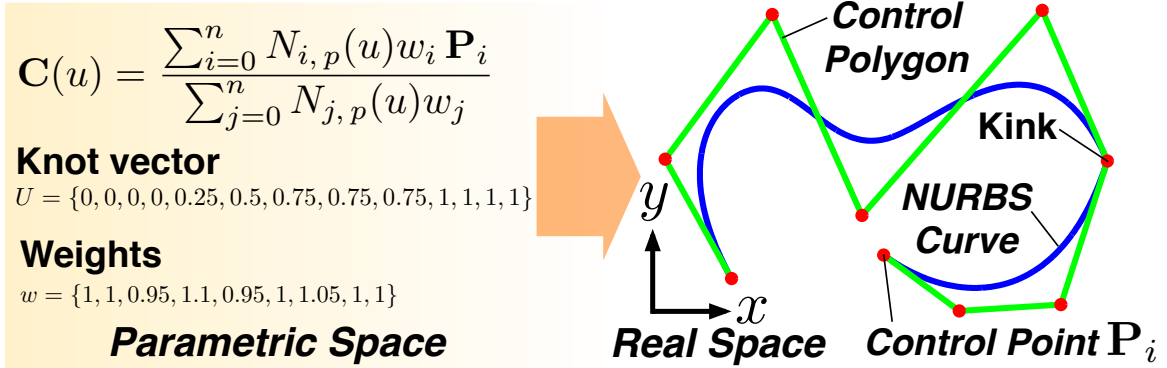


Figure 3.1: Schematic illustration of a NURBS curve. The curve degree p is 3 (cubic). The knots u_i and weights w_j are listed in the vectors U and w , respectively. The kink in the curve is due to full multiplicity $k = p = 3$, in which the knot/parameter value $u = 0.75$ is repeated $p = 3$ times.

3.1.3 Non-Uniform (NU) Rational B-Splines (NURBS)

The NU portion in NURBS is furnished by the knots in the knot vector U of the B-Splines. The non-decreasing knots u_i , $i = 0, 1, \dots, m$ partitions the parameter space into segments of half-open intervals $[u_i, u_{i+1})$, which are also called knot spans. The knot span can be of zero length since the knots need not be distinct, i.e., they can be repeated. The number of times a knot value repeats itself is called multiplicity k . Based on the way the knots are spaced, we can divide B-Splines into the following types:

1. Uniform B-Splines, which can be subdivided into non-periodic and periodic
2. Non-uniform B-Splines

In non-periodic uniform B-Splines, the knots are uniformly spaced except at the ends where the knot values are repeated $p + 1$ times, so that

$$U = \underbrace{\{0, 0, \dots, 0\}}_{p+1}, u_{p+1}, \dots, u_{m-p-1}, \underbrace{\alpha, \alpha, \dots, \alpha}_{p+1} \quad (3.6)$$

The above knots are also referred to as non-periodic or open knots. Non-periodic B-Splines are infinitely continuously differentiable in the interior of a knot span, and $(p - k)$ -times continuously differentiable at a knot. If $k = p$, we say that the knot has full multiplicity; the multiplicity cannot be greater than the degree. Multiplicity of knots provides a way to specify the continuity order between segments. For example, a full multiplicity knot in the

knot vector (away from the ends) means that a kink or cusp is present in the curve. On the other hand, in periodic B-Splines, the knots are uniformly spaced but the first and last knots are not duplicated, so that the knot vector looks like

$$U = \{0, 1, \dots, n\} \quad (3.7)$$

Periodic B-Splines are everywhere $(p - 1)$ -times continuously differentiable.

If the knots are unequally spaced, the knot vector is non-uniform, we get non-uniform B-Splines (the NU part in NURBS). The non-uniformity in knots can cause the degree p of the curve to be different between knot spans. As a matter of terminology and in describing grain geometries, knot vectors can be defined in either $[0, 1]$ or $[0, n]$. The choice of normalization does not have any effect on the shape of the curve, and it is therefore inconsequential. A schematic of a NURBS curve is shown in Figure 3.1.

Remark 3.1.2 *Equation (3.3) is usually taken as the definition of NURBS, although the non-uniformity of the knots is not obvious from this expression.*

Remark 3.1.3 *Several NURBS CAD technologies, such as [Rhino \[89\]](#), which are already available for geometric design of engineering components could be directly integrated into the modeling pipeline, facilitating the transition from binary data to models of granular assemblies.*

Remark 3.1.4 *It is rare that one would work with NURBS models directly in parametric space. In practice, grain shapes are typically generated interactively or through some optimization procedure such as least squares.*

3.1.4 Closing a NURBS curve

To reproduce grain geometries accurately, it is necessary to close the NURBS curves used to describe the grain boundary. There are at least two procedures to close a NURBS curve. In the first procedure, closed NURBS curves are defined by ‘wrapping’ control points. In this process, a uniform knot sequence of $m + 1$ knots is constructed such that: $u_0 = 0, u_1 = 1/m, u_2 = 2/m, \dots, u_m = 1$. Note that the domain of the curve is $[u_p, u_{n-p}]$. Then, the first and last p control points are wrapped so that $\mathbf{P}_0 = \mathbf{P}_{n-p+1} = \mathbf{P}_{n-p+2}, \dots, \mathbf{P}_{p-2} = \mathbf{P}_{n-1}$

and $\mathbf{P}_{p-1} = \mathbf{P}_n$. By wrapping the control points, C^{p-1} continuity is ensured at the joining point $\mathbf{C}(u_p) = \mathbf{C}(u_{n-p})$.

In the second approach, the first and last control points are made coincident, i.e., $\mathbf{P}_0 = \mathbf{P}_n$ and the first and last $p+1$ knots are clamped, i.e., repeated. The curve may or may not have C^k continuity depending on how the first and last k internal knot spans are chosen, and the first and last $k+1$ weights and control points are chosen. Perhaps the simplest example is that of a unit circle in which the control points and weights shown in Table 3.1 are used together with the following knot vector:

$$U = \{0, 0, 0, 1, 1, 2, 2, 3, 3, 4, 4\} \quad (3.8)$$

We notice that $\mathbf{P}_0 = \mathbf{P}_8$ and the first and last three knot values are clamped. Also, there are three pairs of internal knots with multiplicity two. In general, this would lead to a loss of continuity in the first derivative. However, in this case, continuity in the first derivative is maintained by three collinear control points in each of the following sets: $\{\mathbf{P}_7, \mathbf{P}_0 = \mathbf{P}_8, \mathbf{P}_1\}$, $\{\mathbf{P}_1, \mathbf{P}_2, \mathbf{P}_3\}$, $\{\mathbf{P}_3, \mathbf{P}_4, \mathbf{P}_5\}$, and $\{\mathbf{P}_5, \mathbf{P}_6, \mathbf{P}_7\}$. In this work, we will use knot vectors that are clamped.

i	x_i	y_i	w_i
0	1	0	1
1	1	1	$\sqrt{2}/2$
2	0	1	1
3	-1	1	$\sqrt{2}/2$
4	-1	0	1
5	-1	-1	$\sqrt{2}/2$
6	0	-1	1
7	1	-1	$\sqrt{2}/2$
8	1	0	1

Table 3.1: Control points (x_i, y_i) and weights w_i for a unit circle.

3.1.5 NURBS surfaces

In 3D, we describe the grain geometry as a tensor product surface, with the coordinates of the NURBS surface in real space given by components of the vector:

$$\mathbf{Y}(u, v) = \sum_{i=0}^m \sum_{j=0}^n \left(\frac{w_{ij} N_{i,p}(u) N_{j,p}(v)}{\sum_{g=0}^m \sum_{h=0}^n w_{gh} N_{g,p}(u) N_{h,p}(v)} \right) \mathbf{P}_{ij} \quad (3.9)$$

where \mathbf{P}_{ij} are the control points, w_{ij} are the weights, and $N_{i,p}(u)$ and $N_{j,p}(v)$ are the B-Splines univariate basis functions of degree p . We must therefore specify a knot vector for the u basis functions, and a second knot vector for the v basis functions. Although there is no restriction on the choice of degree, we have restricted to NURBS surfaces of (cubic) degree $p = 3$ in our applications.

3.1.6 Relevance of NURBS to DEM calculations

To conclude this section, some of the advantages of using NURBS in the context of DEM calculations are listed. Some of the most salient mathematical properties of NURBS that make them ideal candidates for DEM calculations are [48; 84]:

1. Local support property a point on the surface is locally affected by the surrounding control point
2. Invariance under affine transformations
3. Strong convex hull property
4. Local curvature equation
5. Integration with isogeometric analysis

The local support property affords the method tremendous flexibility in the description of grain geometries. For example, in the case of NURBS curves, local support implies that the basis function $N_{i,p}(u)$ is non-zero on $[u_i, u_{i+p+1}]$. Since the basis function $N_{i,p}(u)$ is the coefficient of control point \mathbf{P}_i , the product $N_{i,p}(u)\mathbf{P}_i$ changes if \mathbf{P}_i changes, but the change in $N_{i,p}(u)\mathbf{P}_i$ only affects the segment on $[u_i, u_{i+p+1}]$, leaving the rest of the curve $\mathbf{C}(u)$ unchanged. Therefore, because of local support, a change in the position of a control point only affects the local portion of the NURBS curve, and this allows great flexibility when trying to approximate grain boundaries accurately. Also, by the local support property,

any modifications to the weights w_i , too, will only affect the section of the NURBS curve on the $[u_i, u_{i+p+1})$ interval.

The invariance property of NURBS under affine transformations is useful when updating the grains described using NURBS within the time integration scheme. Exploiting this property, a grain's position is updated by simply translating and/or rotating the control points relative to the grain's centroid.

The strong convex hull property ensures that, for a closed NURBS curve, the entire grain is located within the convex hull defined by the corresponding control points. Using the control points to define a convex hull bounding each grain, the granular entities described using NURBS can be easily incorporated into existing DEM global collision detection algorithms. We note that the control polygon defined by the control points could be non-convex. Also, the convex hull property fails for negative weights in which a portion of the affected curve segment will be outside of the convex hull defined by the corresponding control points. However, negative weights are not typically used when describing grain shapes, and therefore convex hull failure is typically not a concern.

NURBS provides a simple procedure for evaluating local curvatures. It is well known that contact stresses (e.g., Hertzian contact) depend on the radii of curvature of two contacting bodies. Evaluation of curvature for simple shapes such as circles and ellipses is straightforward but becomes complicated for arbitrary-shaped grains. In addition to providing the tangent and normal boundary vectors needed for contact force calculations, NURBS also provide local curvature evaluations that can be used directly in calculating local contact forces. After obtaining the first and second local derivatives $\mathbf{C}^{(1)}$ and $\mathbf{C}^{(2)}$, respectively, the curvature vector can be evaluated such that

$$\boldsymbol{\kappa} = \frac{(\mathbf{C}^{(1)} \cdot \mathbf{C}^{(1)}) \mathbf{C}^{(2)} - (\mathbf{C}^{(1)} \cdot \mathbf{C}^{(2)}) \mathbf{C}^{(1)}}{(\mathbf{C}^{(1)} \cdot \mathbf{C}^{(1)})^2} \quad (3.10)$$

and consequently, the local radius of curvature is calculated such that $R = 1/\|\boldsymbol{\kappa}\|$.

Finally, the use of NURBS provides a foundation for high-fidelity physics at the granular level. Since NURBS have recently been shown to furnish a basis for isogeometric analysis [48], within each particle more complex analysis, such as plasticity, damage, or possibly breakage, can be performed. Evidently, NURBS can offer tremendous flexibility in repre-

senting and optimizing grain morphology, as well as provide important geometric properties that would enable higher-fidelity discrete calculations.

Remark 3.1.5 *Isogeometric analysis is a computational mechanics technology that uses basis functions emanating from computer aided geometric design (CAGD), such as B-splines, NURBS, and T-splines. It has been shown that isogeometric analysis provides more precise and efficient geometric representations [48].*

Remark 3.1.6 *The last two of the above features of NURBS have not been considered in this thesis. These can potentially be explored in the future.*

3.2 Contact Problem and Implementation

Our earlier work described in [49; 50] has focused on particles geometries that are angular but strictly convex, and the contact algorithms were generalizations of the intersection-based approach used for disks and spheres. While the work has led to improvements in particle morphology representation beyond disks and spheres, it was still limited in two ways. First, the increase in rolling resistance of angular but convex geometries relative to disks is limited. For instance, rolling resistance provided by distributed contact reaction over flat boundaries cannot be represented using strictly convex shapes. Moreover, interlocking behavior between non-convex particles, which contributes significantly to mobilized strength and stability [90; 91], is not accounted for. Second, the generation of strictly convex NURBS shapes is very difficult and restrictive from a modeling perspective. This is even more so when dealing with image data of real particle shapes and obtaining strictly convex boundaries through a fitting procedure is not possible in most cases.

A contact algorithm capable of dealing with general non-convex NURBS particles, to be described in this chapter, would eliminate the above two limitations. As a result, a more faithful representation on the contact force distributions over particle boundaries is obtained and the image data-to-analysis pipeline is significantly streamlined. Without loss of generality, we will work with 3D NURBS surfaces throughout the remaining of this chapter. We also assume that the underlying parametric domain has been normalized, i.e., $0 \leq u \leq 1$ and $0 \leq v \leq 1$ (a unit square).

3.2.1 General definition

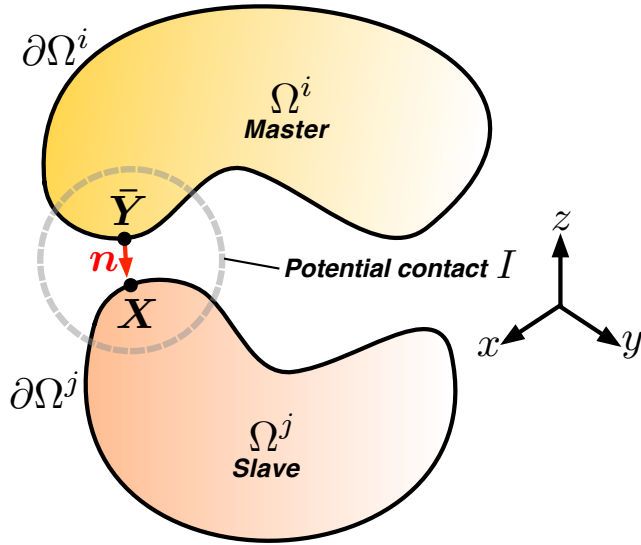


Figure 3.2: Contact problem between two particles Ω^i and Ω^j . Refer to text for description.

We consider a general two-particle contact problem in three dimensions, with the particles in question to be potentially contacting at some time instant t . Referring to Figure 3.2, let W_i be the set of potential contacts associated with particle i , and denote using $I \in W_i$ a particular contact point in the set.

Following a master-slave approach to describe the contact problem [92], a contact point on the slave particle Ω^j is denoted by \mathbf{X} while the contact point on the master particle Ω^i is defined to be the closest point projection (CPP) of \mathbf{X} onto the surface of the master particle: i.e., the point that is closest to \mathbf{X} among all points in the master particle

$$\bar{\mathbf{Y}} \equiv \bar{\mathbf{Y}}(\mathbf{X}) = \min_{\mathbf{Y} \in \partial\Omega^i} \|\mathbf{X} - \mathbf{Y}\| \quad (3.11)$$

where $\|\cdot\|$ is the standard Euclidean norm. As shown in Figure 3.2, the contact plane at a potential contact point I is described on the master surface $\partial\Omega^i$ by the outward unit normal \mathbf{n} at point $\bar{\mathbf{Y}}$. The gap or penetration at time t is then defined as

$$g(\mathbf{X}) = [\mathbf{X} - \bar{\mathbf{Y}}(\mathbf{X})]^T \mathbf{n} \quad (3.12)$$

dot product, but $|\mathbf{n}|=1$ (unit normal), so this is vectorXY's projection along n direction
<0 if vectorXY and normal vector are in opposite direction (overlap)

By this definition, contact penetration occurs if $g(\mathbf{X}) < 0$. This convention is similar to

that used in the definition of contact problems in the finite element method (FEM) [92]. In the context of classic DEM [24] with a linear contact law, once the gap is determined, the normal contact force on the master particle is then calculated as (refer to (2.1)):

$$\mathbf{f} = \begin{cases} k_N g(\mathbf{X}) \mathbf{n}, & \text{if } g(\mathbf{X}) < 0 \\ \mathbf{0}, & \text{otherwise} \end{cases} \quad (3.13)$$

where k_N is the normal contact stiffness. An equal and opposite force acts on the slave particle. Essentially, the contact problem boils down to the problem of solving the CPP problem (3.11) and in the remaining sections, we describe how this is done in the context of NURBS. Task: how to find the closest projection point

3.2.2 Knot positioning

We generalize the node-to-surface approach typically used in the contact treatment of finite element models [92] to a ‘knot-to-surface’ (KTS) approach to enable the contact treatment of non-convex particles described using NURBS surfaces. More recently, the KTS approach has been employed in isogeometric finite elements [93] and a similar approach is taken here. The contact points \mathbf{X} associated with the slave particle are represented through knots and these points are to be projected onto the master surface to determine if there is contact penetration. The representation of contact points through knots is necessary for computational tractability, as well as for tracking the incremental slip and contact gain or loss around non-convex surfaces of potentially contacting particles. While similar to nodal discretization in FEM, we emphasize that the key difference here is that the positioning of contact points by knots does not change the particle geometry, i.e., isogeometric; the knots vary continuously in the underlying parametric space. In this work, we have adopted to position the knots a priori as a preprocessing step.

In real applications where a large number of arbitrary-shaped grains are represented by 3D NURBS surfaces, the manual positioning of knots proved to be extremely difficult, if not impossible. As such, an automatic and adaptive knot positioning strategy is required. To this end, we have devised an automatic knot positioning algorithm based on a NURBS recursive subdivision scheme (see Algorithm 2). The NURBS surface is subdivided until the following termination criteria (see Figure 3.3) are met:

1. Real space arc distance corresponding to each parametric direction of less than ϵ_d
2. Acute angle between normal vectors at adjacent knot positions of less than ϵ_θ

and a knot or node is positioned at the center of the subdivided surface at the terminated level.

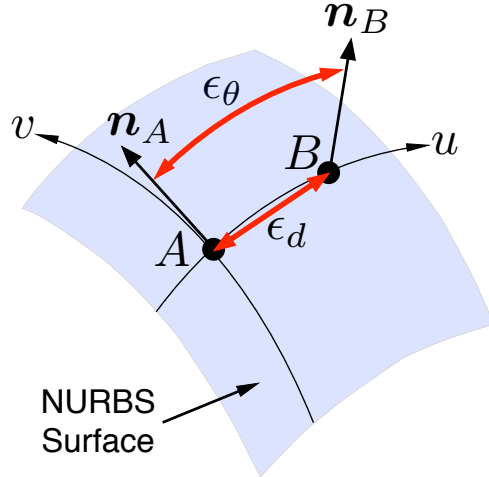


Figure 3.3: Measures used for terminating the NURBS subdivision in the knot or node generation procedure. The two normal vectors emanating from nodes A and B are denoted by \mathbf{n}_A and \mathbf{n}_B , respectively. NURBS parametric directions are u and v .

think of this step as the mesh generation step in FEM
knots == nodes, the mesh of knots is generated by recursive subdivision until certain criteria is met

36

Input: NURBS surface $S = \mathbf{Y}(u, v)$, real arc distance tolerance ϵ_d , angle tolerance ϵ_θ

Output: List of knot positions in real space

procedure AKP(S)

 Calculate the real-space points corresponding to the corners in parametric space:
 $\mathbf{x}_1 = \mathbf{x}(u_{\min}, v_{\min})$, $\mathbf{x}_2 = \mathbf{x}(u_{\max}, v_{\min})$, $\mathbf{x}_3 = \mathbf{x}(u_{\max}, v_{\max})$, $\mathbf{x}_4 = \mathbf{x}(u_{\min}, v_{\max})$

 Calculate real arc distance corresponding to each parametric direction:

$$D_u = \max(\|\mathbf{x}_3 - \mathbf{x}_4\|, \|\mathbf{x}_1 - \mathbf{x}_2\|), D_v = \max(\|\mathbf{x}_1 - \mathbf{x}_4\|, \|\mathbf{x}_2 - \mathbf{x}_3\|)$$

 Let $\Delta u = u_{\max} - u_{\min}$, $\Delta v = v_{\max} - v_{\min}$, $u_{\text{ave}} = (u_{\max} + u_{\min})/2$,
 $v_{\text{ave}} = (v_{\max} + v_{\min})/2$.

 Define acute angle between unit normal vectors $\theta(\mathbf{n}_1, \mathbf{n}_2) = \cos^{-1}(\mathbf{n}_1 \cdot \mathbf{n}_2)$

if ($D_u > D_v$)* **then**

 Compute unit normal vectors: $\mathbf{n}_{u1} = \mathbf{n}(u_{\min} + \Delta u/3, v_{\text{ave}})$,
 $\mathbf{n}_{u2} = \mathbf{n}(u_{\min} + 2\Delta u/3, v_{\text{ave}})$ and $\theta_u = \theta(\mathbf{n}_{u1}, \mathbf{n}_{u2})$.

if ($D_u > \epsilon_d$) **and** ($\theta_u > \epsilon_\theta$) **then**

 | Split surface into 2 child surfaces S_1, S_2 at u_{ave}

else

 | Surface is a LEAF

end if

else ($D_u \leq D_v$)*

 Compute unit normal vectors: $\mathbf{n}_{v1} = \mathbf{n}(u_{\text{ave}}, v_{\min} + \Delta v/3)$,
 $\mathbf{n}_{v2} = \mathbf{n}(u_{\text{ave}}, v_{\min} + 2\Delta v/3)$ and $\theta_v = \theta(\mathbf{n}_{v1}, \mathbf{n}_{v2})$.

if ($D_v > \epsilon_d$) **and** ($\theta_v > \epsilon_\theta$) **then**

 | Split surface into 2 child surfaces S_1, S_2 at v_{ave}

else

 | Surface is a LEAF

end if

end if

if (Surface is a LEAF) **then**

 | Store midpoint $\mathbf{x}(u_{\text{ave}}, v_{\text{ave}})$ as a knot position

else

 | Recurse, i.e., apply AKP, on the two child surfaces S_1, S_2

end if

end procedure

*For a closed single patch NURBS surface, a seam joins either the edges at (a) $u = 0, 1$ or (b) $v = 0, 1$. At first entry into this procedure, the **if** ($D_u > D_v$) block is executed for case (a) while the **if** ($D_u \leq D_v$) block is executed for case (b).

Algorithm 2: Automatic Knot Positioning (AKP) Algorithm.

3.2.3 Distance function

The distance function of a fixed slave point \mathbf{X} on a slave surface to a master surface $\mathbf{Y}(u, v)$ is given by

$$d(u, v) = \|\mathbf{X} - \mathbf{Y}(u, v)\| \quad (3.14)$$

or, squaring both sides, we obtain the distance squared function

$$f(u, v) = [\mathbf{X} - \mathbf{Y}(u, v)]^T [\mathbf{X} - \mathbf{Y}(u, v)] \quad (3.15)$$

where $f(u, v) = [d(u, v)]^2$ and the coordinates of the NURBS surface $\mathbf{Y}(u, v)$ is given by (3.9).

The CPP problem can then be formulated as (cf. (3.11))

$$\bar{\mathbf{Y}} = \min_{(u,v) \in \Gamma} f(u, v) \quad (3.16)$$

where Γ is the bounded normalized parametric space of the NURBS master surface. In real applications, where surfaces are always well-defined, the underlying NURBS basis functions are products or quotients (with denominators that are bounded away from zero) of univariate B-Splines basis functions, which in turn are polynomials. This implies the distance squared function $f(u, v)$ is Lipschitz continuous. This means that there exists a finite bound on the rate of change of the squared distance function. This key observation allows one to employ the Lipschitzian dividing rectangle (DIRECT) global optimization procedure as a solution to the CPP problem.

3.2.4 The DIRECT optimization algorithm

Here, we describe how the DIRECT algorithm can be adapted to the CPP problem (3.16). We describe the following two components of the DIRECT algorithm,

1. Sample and subdivide
2. Identification of potentially optimal parametric rectangles

followed by a simple example to illustrate how the overall DIRECT algorithm works. We emphasize that, in the application of this algorithm, the NURBS surface or underlying

parametric domain is not physically subdivided. The key feature of the DIRECT algorithm is that the subdivisions are performed implicitly through sampling (i.e., function evaluation) and selection of optimal rectangles.

3.2.4.1 Sample and subdivide

The basic idea of this step is as follows: the sampling part determines the goodness of the current solution of f in (3.16), while the subdivision part ensures efficiency as well as convergence of the DIRECT algorithm. After subdivision, the parametric domain will consist of subregions that are either squares or rectangles. We first describe the sample and subdivide step for squares followed by an extension to rectangles.

The basic idea behind the DIRECT algorithm is the sampling of the values of the function f at the points $\mathbf{c} \pm \delta \mathbf{e}_i$, $i = 1, 2$, where \mathbf{c} is the center of the parametric square, δ is one-third side length of the parametric square, and \mathbf{e}_i is the unit vector in either the u ($i = 1$) or v ($i = 2$) direction. Since the underlying parametric domain of the NURBS surface is 2D, the sampling points would be located above, below, to the left, and to the right of the center point (see Figure 3.4(a) or (b)).

The square domain is subdivided such that each subregion (rectangle or square) would contain a sample point at its center. The following strategy for subdividing the square is adopted in [94]. Let

$$w_i = \min \{f(\mathbf{c} - \delta \mathbf{e}_i), f(\mathbf{c} + \delta \mathbf{e}_i)\}, \quad i \in 1, 2 \quad (3.17)$$

be the best of the function values sampled along the u and v directions. First, split the square into thirds along the dimension with the smallest w value. Then, split the rectangle that contains \mathbf{c} into thirds along the remaining direction. This strategy ensures that the largest subrectangle contains the sample point with the best function value, i.e., lowest f value. The reason for this strategy is to bias the search near points with good function values, since larger rectangles are preferred for sampling (as a result of convex hull; see below). For rectangular domains, the subdivision is performed only along the long dimension. This ensures that the rectangles shrink in both parametric directions, ensuring convergence [94]. Examples illustrating this subdivision strategy are shown in Figure 3.4. Algorithm 3 formally describes the above steps and covers both square and rectangular domains.

Input: A parametric subregion (rectangle or square)

Output: A subdivided subregion

- 1: Identify the set $I \subseteq \{1, 2\}$ with maximum parametric side length in parametric space, where 1 and 2 are in the u and v directions, respectively. Let δ equal to one-third of this maximum length (if square, pick both sides, otherwise pick longer dimension - see explanation in the text).
- 2: Sample the function at the points $\mathbf{c} \pm \delta \mathbf{e}_i$ for all $i \in I$, where \mathbf{c} is the center of the parametric rectangle and \mathbf{e}_i is the i -th unit vector.
- 3: Divide the rectangle containing \mathbf{c} into thirds along the dimensions in I , starting with the dimension lowest value of

$$w_i = \min \{f(\mathbf{c} - \delta \mathbf{e}_i), f(\mathbf{c} + \delta \mathbf{e}_i)\}$$

and continue to the next dimension. from i=1 to i=2, vertical dimension to horizontal dimension for example

Algorithm 3: Sample and Subdivide Algorithm

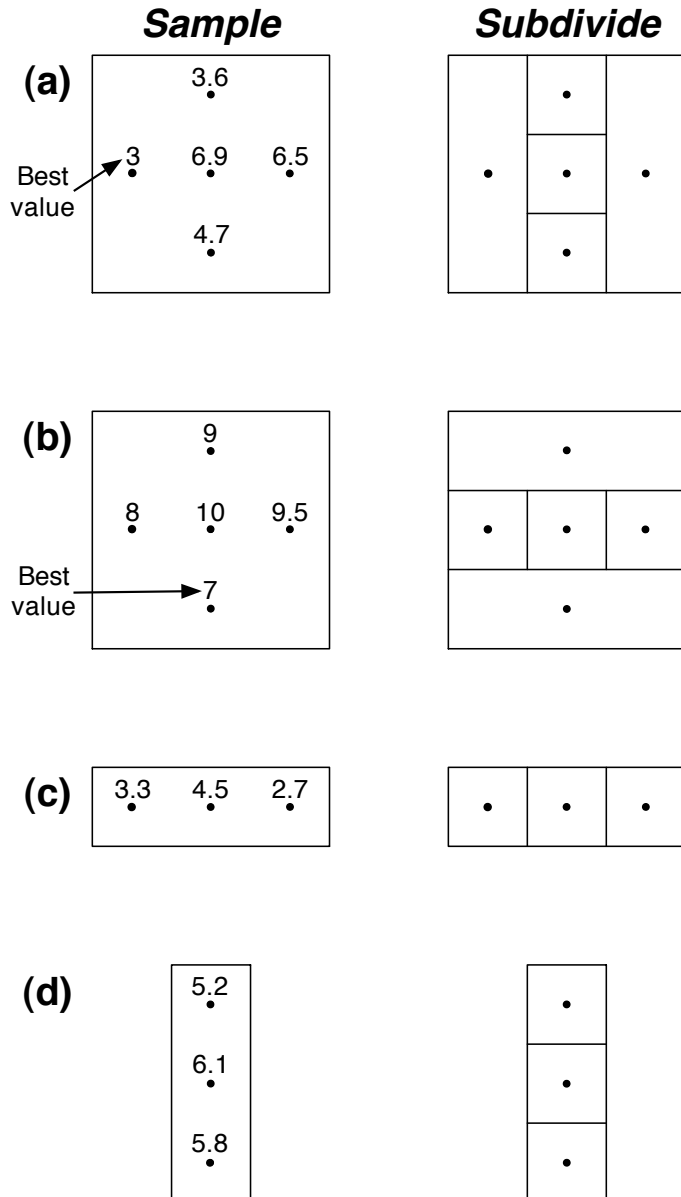


Figure 3.4: Example cases of sample and subdivide. For cases (a) and (b), the domain is square, and the subdivision is such that the largest subrectangles contain the sample points with the best function values, i.e., lower f values. For cases (c) and (d), the domain is rectangular, and the subdivision is performed only along the long dimension.

3.2.4.2 Identification of potentially optimal rectangles

Assume that we have partitioned the unit square parametric domain underlying the NURBS surface into a total of m rectangles (or squares if the sides are equal). To select optimal rectangles for subdivision, we first compute the following for each rectangle j :

- Distance from its center to its vertex d_j
- Function value evaluated at the center $f_j = f(\mathbf{c}_j) = f(u_j, v_j)$

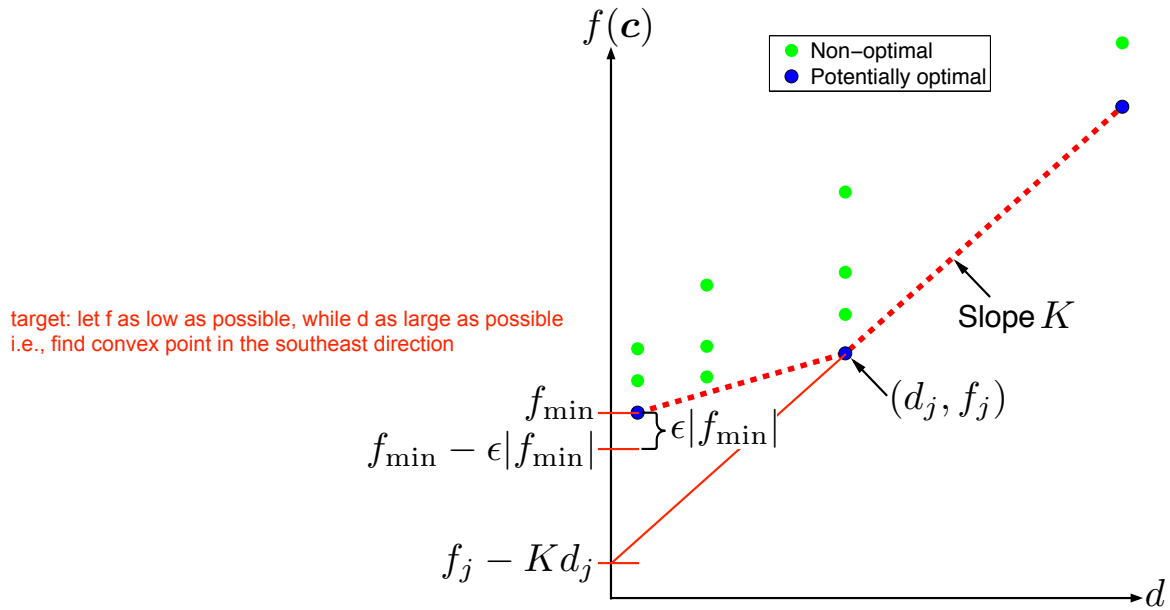


Figure 3.5: A schematic of the graph of $f(\mathbf{c})$ versus d for all rectangles in the parametric domain. Refer to the text for the meaning of the labeled quantities.

Then, we plot the points (d_j, f_j) on a graph with f_j on the abscissa for all $j = 1, \dots, m$, as shown schematically in Figure 3.5. Each point on the graph represents a rectangle in the parametric domain. The set of potentially optimal rectangle is defined as follows.

Definition 1 Let $\epsilon > 0$ be a positive constant and f_{\min} be the best current solution, i.e., the lowest value of f over all m rectangles. A rectangle j is said to be potentially optimal if there exists some $K > 0$ such that

$$f_j - Kd_j \leq f_i - Kd_i, \quad \forall i = 1, \dots, m \quad (3.18)$$

$$f_j - Kd_j \leq f_{\min} - \epsilon |f_{\min}| \quad (3.19)$$

We note that K is simply a rate-of-change constant but we can loosely interpret it as a Lipschitz constant. From Figure 3.5, $f_j - Kd_j$ can be seen as an abscissa intercept, which provides the lower bound for f_j . The lower bound contains two terms f_j and $-Kd_j$. The first term is lower when the function values are lower. Thus, this term favors locations where previous function values are lower, i.e., emphasis on local search. The second term is lower the larger d_j becomes. Therefore, this term puts the search emphasis on larger rectangles, i.e., emphasis on global search. As such, K can also be interpreted as a relative weight on global versus local search. Instead of relying on a single constant K , which is usually high (too much emphasis on global search) and resulting in slow convergence, the DIRECT algorithm considers all possible weights, and at the same time determines and reduces the weights as the search proceeds. Moreover, the algorithm does not require the a priori specification of the weights, which are usually very hard to estimate or are completely unknown. To see how these are achieved, we observe that geometrically the first condition (3.18) means that the optimal rectangles can be found as the lower right of the convex hull of the set of points in the graph of f (see dashed red line in Figure 3.5). This means that there is no need to determine K . The second condition (3.19) prevents the algorithm from becoming too local, at which point too many iterations are performed for marginal improvements. This means that some of the smaller rectangles near the bottom right of the aforementioned convex hull may not be selected. A range of 10^{-3} to 10^{-7} has been suggested but DIRECT is rather insensitive to the choice of ϵ [94], due to the convex hull procedure to select potentially optimal rectangles. The convex hull of points can be performed efficiently using the Graham's scan algorithm [95]. If the rectangles are sorted by function value within groups of rectangles with the same center-vertex distance, the resulting computational complexity is $O(m')$, where $m' < m$ is the number of distinct center-vertex distances [94]. For further details on data structures, implementation strategies, and theoretical analysis of the DIRECT algorithm, we refer the reader to [94; 96; 97].

To prevent proliferation of function evaluations as the global minimum is approached, we terminate the DIRECT global search when the relative change in the parameter values is less than some tolerance (e.g., $\Delta u/u, \Delta v/v < 0.1$) and switch to a local minimization step to finalize the contact point on the master surface. We use the parametric values at termination of the DIRECT global search as an initial guess and a small neighborhood around this initial guess as the search domain. The local minimization problem can be

solved using either gradient-based or derivative-free constrained optimization algorithms [98]. Here, we choose the derivative-free procedure since it is simpler and does not require the evaluation of the Hessian of the function f .

3.2.5 Implementation of contact algorithm

The implementation of the CPP operation can be simply achieved by programming a function handle that returns the squared distance value f between a given slave contact point \mathbf{X} and a point $\mathbf{Y}(u, v)$ on the master surface, and using this function handle in the DIRECT algorithm. The CPP algorithm proceeds as described in Algorithm 4. The one-to-one mapping of the DIRECT algorithm to the CPP problem is particularly noteworthy; except for a few quantities that are relevant to NURBS and the CPP problem, the steps proceed identically with those laid out in [94]. An illustration of the DIRECT algorithm for a few iterations is shown in Figure 3.6. The proposed contact algorithm is then implemented by applying the CPP algorithm on candidate contact points \mathbf{X} of the slave surface to determine their closest projected points $\bar{\mathbf{Y}}(\mathbf{X})$. The penetration is calculated using (3.12), from which the corresponding normal contact force vector on the master particle is then determined by (3.13).

The identification of candidate slave contact points for the CPP operation can be performed through a number of standard collision detection algorithms (e.g., [42]). For example, only those points that are inside the bounding box of the master surface will be considered.

this step is quite similar to polyhedra case

Input: Slave point \mathbf{X} and master surface $\mathbf{Y}(u, v)$

Output: Closest projected point $\bar{\mathbf{Y}}(\mathbf{X})$

- 1: Let $\mathbf{c}_1 = (u_1, v_1)$ be the center point of normalized parameter space (unit square) and evaluate $f(\mathbf{c}_1)$. Set current best value $f_{min} = f(\mathbf{c}_1)$, number of sample points $m = 1$, and iteration counter $k = 0$.
- 2: Identify the set S of potentially optimal parametric rectangles.
- 3: Select any rectangle $j \in S$.
- 4: Sample and subdivide (see Algorithm 2). Update f_{min} and $m = m + \Delta m$ where Δm is the number of new points sampled.
- 5: Remove rectangle j from set S . If S is not empty, go to Step 3.
- 6: Increment iteration counter $k = k + 1$. If relative in parametric direction is less than specified tolerance, go to Step 7. Otherwise, go to Step 2.
- 7: Start constrained optimization procedure using current best (u, v) and corresponding parametric rectangle to finalize the closest projected point on the master surface $\bar{\mathbf{Y}}(\mathbf{X})$. Exit.

Algorithm 4: DIRECT Closest Point Projection Algorithm

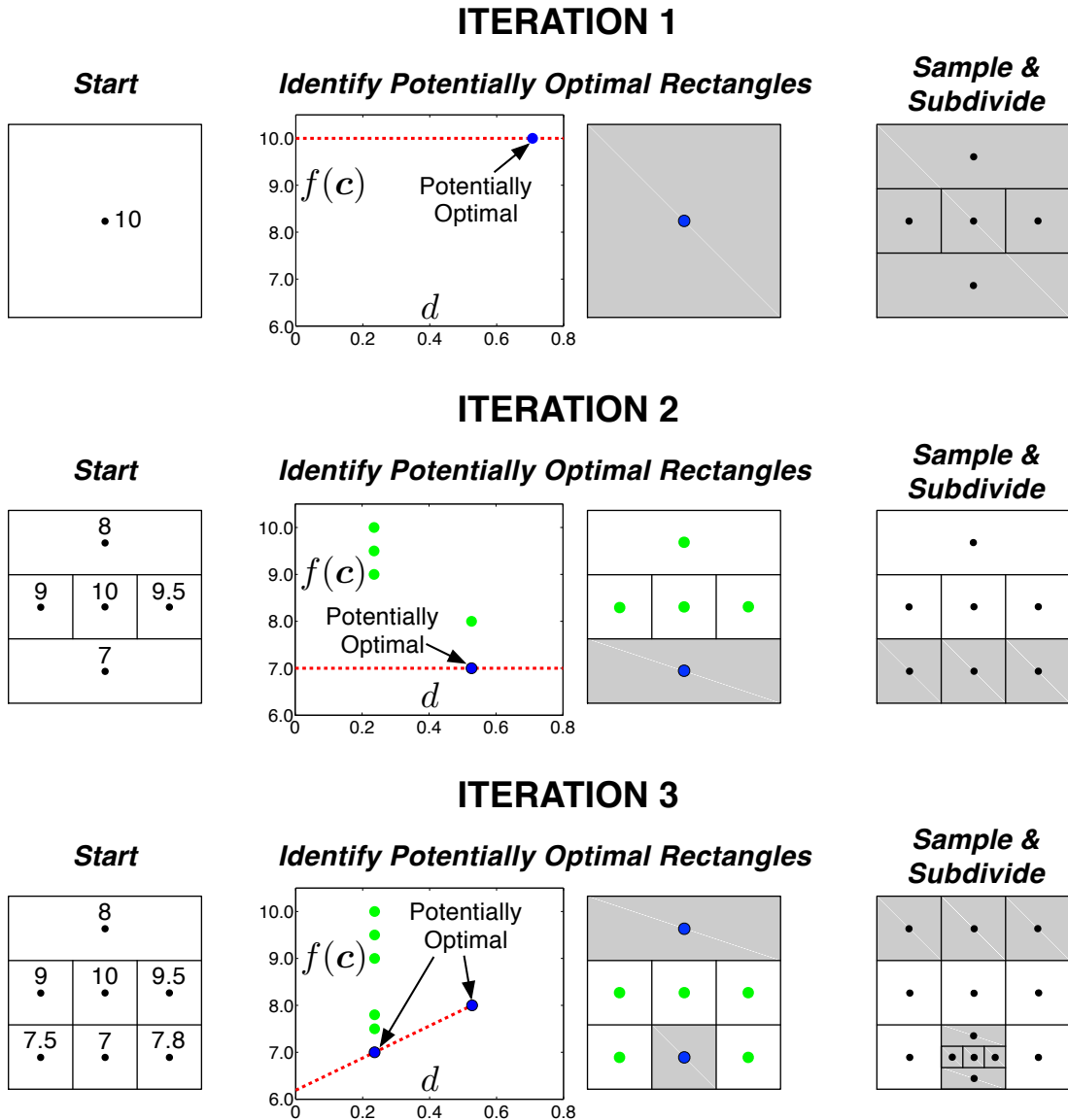


Figure 3.6: Illustration of DIRECT algorithm. For simplicity, we have set ϵ in (3.19) to zero. The lines are only to guide the eye — there is no physical subdivision of the NURBS surface or underlying parametric surface; instead the subdivision is performed implicitly through sampling and selection of optimal rectangles.

3.3 Closure

We have presented a new algorithm for determining the signed gap value for non-convex NURBS surfaces. The functionality of the algorithm will be demonstrated through discrete simulations described in the next two chapters.

Chapter 4

A Contact Dynamics Formulation

4.1 Introduction

In this chapter, we describe a contact dynamics (CD) approach to our NURBS-based discrete method. By combining particle shape flexibility through NURBS, properties of implicit time integration (e.g., larger time steps) and non-penetrating constraints, as well as a reduction to a static formulation in the limit of an infinite time step, we target applications in which the classical discrete element method either performs poorly or simply fails, i.e., in granular systems composed of rigid or highly stiff angular particles and subjected to quasi-static or dynamic flow conditions. The integration of CD and our NURBS-based discrete method is made possible while significantly simplifying implementation and maintaining comparable performance with existing CD approaches.

To motivate the development of our approach, we first refer the reader to Table 4.1 for a brief summary of the key features of and differences between CD and the classical DEM by Cundall and Strack [24]. In the following, we highlight the difficulties associated with classic CD and DEM followed by a description on how we eliminate them through the combined approach.

The so-called Non-Smooth CD, originally developed by Moreau [61; 62; 102; 103], is an alternative discrete approach to the DEM. The most prominent feature of CD, in contrast to that of classical DEM, is that the particles are considered perfectly rigid and the contact forces are determined as those that prevent interparticle penetration and at the same time satisfy the frictional stick-slip constraints. In their simplest forms, these contact laws are embodied in the so-called Signorini unilateral contact condition and classical Coulomb law, as shown in Figures 2.2a and 2.2b, respectively. Commensurate with these physical

Table 4.1: Comparison of Non-Smooth Contact Dynamics and classical DEM

Feature	Non-Smooth Contact Dynamics	Classic DEM
Normal contact	Rigid; unilateral contact ^{1,2} or non-penetration constraint directly included	Modeled using normal spring; particles overlap
Friction contact	Stick-slip frictional constraint ^{1,2} directly included	Imposes shear force incrementally using relative velocity from previous step
Time integration	Implicit, usually stable, and with larger time step ³	Explicit, with stability criterion; critical time step scales with inverse of spring frequency. Inefficient for highly stiff particles and cannot be applied to rigid particles
Collision response	Considers collisions and stick-slip frictional transitions simultaneously; velocities may be non-smooth	No real collisions and velocity jumps cannot occur due to continuous nature of contact spring
Damping	Numerical damping ⁴	Through global and/or local damping devices, i.e., dashpots
Quasistatic limit	Can be directly included in formulation	Dynamic in nature; oscillations in solutions are typical; quasistatic limit is approached using global and/or local damping
Particle morphology representation ^{5,6}	Disk- or sphere-clustering and polyhedra	
Implementation difficulty	Intermediate to difficult ⁷	Easy
Computational efficiency	Contact and constraint forces solved implicitly. Geometrical information (e.g., gap values and contact orientations) are stored in matrices as part of the solution procedure; higher memory requirement ⁸	Contact forces are solved explicitly using particle overlap and previous velocities; time integration easily parallelized. Minimal storage of geometrical information; lower memory requirement

(1) Regularization to account for particle elasticity possible (e.g., [99])

(2) See Figure 2.2

(3) Although the time step can be larger, it has to be reasonable so that collisions are properly resolved

(4) Does not apply in the quasistatic limit

(5) We list only those approaches, beyond ellipses/ellipsoids, that appear to be currently most widely applied

(6) Improved using NURBS in this work

(7) Made easier in this work

(8) In this work, managed using efficient large-scale mathematical programming solvers (e.g., [100; 101])

enhancements, however, is the need for both contact and constraint forces to be solved simultaneously or implicitly since the problem is nonlinear. The need for an implicit solution procedure till today remains the primary reason why CD is deemed much more complicated to implement than DEM. This has thwarted the wide adoption of CD despite the favorable performance that has been shown through a number of studies [73–83].

While there is wide applicability of DEM, its application has gone beyond its restriction as a tool that is strictly applicable only to materials with finite elasticity. For example, DEM is widely used as a tool to study real granular materials that are almost rigid or highly stiff in nature. Here, finite elasticity means that the contact interaction is essentially modeled using springs. Under explicit time integration algorithms that are typically used in DEM, the stable time step is restricted by the critical time step, which scales with the inverse of the contact spring-particle mass frequency. This results in infinitesimally small time steps if material parameters corresponding to highly stiff particles (e.g., rocks, sand, steel) if the material is perfectly rigid, the time step should theoretically be 0 are used. Although explicit integration algorithms can be easily parallelized, the runtime for stiff systems remains computationally prohibitive. One modeling technique commonly employed in practice to overcome this restriction is to simply reduce the contact stiffness, usually by two to four orders of magnitude, to the extent that particle kinematics obtained from simulations are still somewhat representative of the overall response of the actual system of interest. If quasi-static behavior is assumed to hold, usually used in combination with stiffness tuning is mass scaling, in which the particle masses are adjusted (usually increased) such that the combined spring-particle system frequency is lowered, increasing the time step size. In practice, model calibration by means of mass scaling and/or stiffness tuning is a delicate and cumbersome process. Another problem that is associated with the presence of contact springs and the dynamic nature of DEM is the introduction of unwanted oscillations or noise, with frequencies that increase with spring stiffness. This requires additional calibration of the global and/or local damping parameters. Moreover, under certain loading conditions (e.g., strain-controlled and dynamic), either particle kinematics or contact forces obtained under such calibration procedures can be highly inaccurate [57].

Recent CD approaches include techniques to represent complex particle morphology or shape, and these have been described in Chapter 2. In this aspect, recent trends show a clear dichotomy between the choice of shape representation technique. A key component in the CD formulation is the signed separation or gap, which is used in the determination

of constraint forces to prevent particle interpenetration. While the polyhedra approach is considered a more accurate shape representation technique than the clustering approach, the associated algorithms for the determination of the signed penetration are complicated due to the need to enumerate all the various combinations of contact entities (node, edge, surface). As such, the simpler disk/sphere-clustering is favored over the more accurate polyhedra-based approach.

We combine and refine two important developments that allow us to eliminate all the above difficulties:

- We simplify the formulation and implementation of CD significantly by generalizing a variational CD formulation recently developed for disks and spheres [72; 99; 104]. This particular formulation, which is employed here, is appealing because it provides a way for CD to be easily implemented and solved using off-the-shelf mathematical programming solvers. The most prominent advantage of this formulation is its automatic inclusion of the quasi-static limit, enabling quasi-static modeling without the need for adjusting damping parameters or time step.
- We remove the complexities associated with polyhedra-based contact detection algorithms by adopting NURBS to describe arbitrary particle geometries. Following the approach as described in Chapter 3 to determine the signed gap, the integration of our NURBS-based discrete method into the CD formulation is shown to be simple and straightforward. The ‘knot-to-surface’ approach to contact described in Chapter 3 is similar to that employed in the contact treatment of frictionless bodies in isogeometric analysis [93]. The key difference and novelty here is on the simultaneous treatment of contact elasticity and frictional contact within the aforementioned CD formulation, as well as the ability to perform contact calculations for granular systems, which contain a large number of particles. Both particle elasticity and friction at the contact level are treated implicitly and simultaneously, and the contact algorithm is cast into a mathematical programming-based contact dynamics framework.

This chapter describes the details of how each of the above items is implemented and is structured as follows: we describe the contact problem and summarize the variational formulation of the general contact problem for frictional particles in Section 4.2; then, we present two numerical examples in Section 4.4 to demonstrate the capabilities of the com-

bined approach before closing in Section 4.5. For clarity of presentation and implementation details, we limit our discussion to the two-dimensional case. An extension of the method to the three-dimensional setting is outlined in Appendix B.

4.2 Governing Equations for Frictional and Arbitrary-Shaped Particles

The formulations from [51; 72; 99; 104] carry forward completely to the general case of frictional and arbitrary-shaped particles without any change. As such, simplicity of implementation is retained. Here, we present a summary containing only those key equations required for the completeness of presentation. Where necessary, we point the reader to the appropriate references for further details.

4.2.1 General contact problem definition

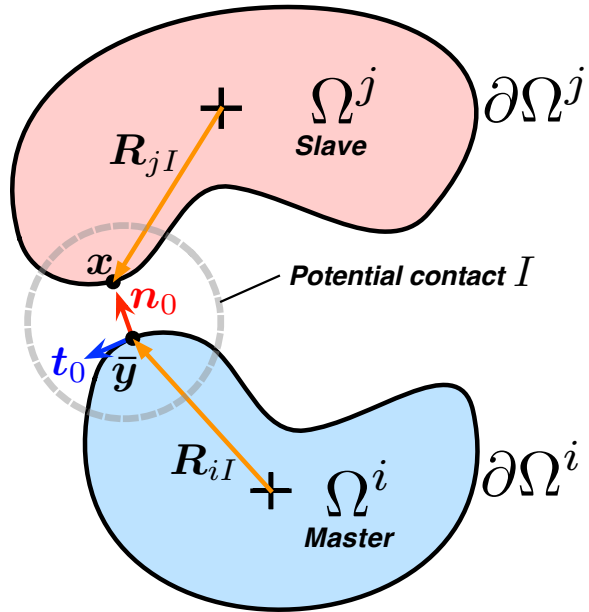


Figure 4.1: Illustration of the problem of contact between two particles (Ω^i and Ω^j) at time t_0 . See text for a description of the associated quantities.

For convenience, we repeat here the contact problem described in Chapter 3, specialized to the 2D case as shown in Figure 4.1. The two-particle contact problem is defined at some initial time t_0 . Let W_i be the set of potential contacts associated with particle i and denote by $I \in W_i$ a particular contact point in the set. A contact point on the slave

particle Ω^j is denoted by \mathbf{x} , while the contact point on the master particle is defined as the closest point projection of \mathbf{x} onto the boundary of the master particle:

$$\bar{\mathbf{y}} \equiv \bar{\mathbf{y}}(\mathbf{x}) = \min_{\mathbf{y} \in \partial\Omega^i} \|\mathbf{x} - \mathbf{y}\| \quad (4.1)$$

As shown in Figure 4.1, the contact plane at a potential contact point I is described on the master boundary $\partial\Omega^i$ by the normal \mathbf{n}_0 and tangent \mathbf{t}_0 at point $\bar{\mathbf{y}}$. The gap at time t_0 is then defined as

$$g_0(\mathbf{x}) = (\mathbf{x} - \bar{\mathbf{y}}(\mathbf{x}))^T \mathbf{n}_0 \quad (4.2)$$

with the non-penetration constraint requiring that $g \geq 0$.

unlike DEM, particle can never really penetrate. there is always a gap, and after collision, they will again have gap

4.2.2 Notation for general multi-particle system

To facilitate the variational formulation of the governing equations, we first set the notation for the general multi-particle system that will be used throughout this chapter. A particle i has mass m^i and mass moment of inertia J^i . The position and rotation of the particle are denoted by $\mathbf{x}^i = (x^i, y^i)^T$ and α^i , respectively, and their corresponding translational and rotational velocities by $\mathbf{v}^i = (v_x^i, v_y^i)^T$ and ω^i . We introduce the following matrix or vector quantities that cover general n -particle systems:

$$\begin{aligned} \mathbf{M} &= \text{diag}(m^1, m^1, \dots, m^n, m^n) \\ \mathbf{J} &= \text{diag}(J^1, \dots, J^n) \\ \mathbf{x} &= (\mathbf{x}^1, \dots, \mathbf{x}^n), \mathbf{v} = (\mathbf{v}^1, \dots, \mathbf{v}^n) \\ \boldsymbol{\alpha} &= (\alpha^1, \dots, \alpha^n), \boldsymbol{\omega} = (\omega^1, \dots, \omega^n) \\ \mathbf{g} &= (g^1, \dots, g^N), \mathbf{p} = (p^1, \dots, p^N), \mathbf{q} = (q^1, \dots, q^N) \end{aligned} \quad (4.3)$$

where \mathbf{M} is the diagonal matrix containing the particle masses and \mathbf{J} is the diagonal matrix containing the particle mass moments of inertia. The kinematical quantities are the vectors of particle translations \mathbf{x} and rotations $\boldsymbol{\alpha}$, and their corresponding velocities \mathbf{v} and $\boldsymbol{\omega}$. The contact quantities are given by the vectors \mathbf{p} , \mathbf{q} , and \mathbf{g} , which are the contact normal forces, shear forces, and gap values, respectively, each at N number of contacts.

n is number of particles, N is number of contacts

A quantity, which at the initial time is denoted by \square_0 , would then be denoted at time

$t_0 + \Delta t$ by \square . For example, \mathbf{x}_0 and \mathbf{v}_0 are the known positions and velocities at time t_0 , while \mathbf{x} and \mathbf{v} are the corresponding quantities at time $t_0 + \Delta t$. With this notation, an increment of a quantity will be denoted by $\Delta \square = \square - \square_0$.

4.2.3 Discrete update equations

Under the discretization of the equations of motion using the θ -method [105], the resulting discrete update equations for translation and rotations are given by:

$$\begin{aligned}\bar{\mathbf{M}}\Delta\mathbf{x} &= \bar{\mathbf{f}}_0 = \mathbf{f}_{\text{ext}} + \bar{\mathbf{M}}\mathbf{v}_0\Delta t \\ \bar{\mathbf{J}}\Delta\boldsymbol{\alpha} &= \bar{\mathbf{m}}_0 = \mathbf{m}_{\text{ext}} + \bar{\mathbf{J}}\boldsymbol{\omega}_0\Delta t\end{aligned}\quad (4.4)$$

rotational moment

In the above, the matrices $\bar{\mathbf{M}}$ and $\bar{\mathbf{J}}$ contain the scaled particle masses and mass moments of inertia, respectively:

$$\begin{aligned}\bar{\mathbf{M}} &= \frac{1}{\theta\Delta t^2}\mathbf{M} \\ \bar{\mathbf{J}} &= \frac{1}{\theta\Delta t^2}\mathbf{J}\end{aligned}\quad (4.5)$$

The effective translational force vector $\bar{\mathbf{f}}_0$ contains the external load vector \mathbf{f}_{ext} , which we have assumed to be constant (e.g., due to gravity). The effective rotational moment vector $\bar{\mathbf{m}}_0$ contains the external rotational moments \mathbf{m}_{ext} , which may be applied on the particles.

The translational and angular velocities are calculated, respectively, as

$$\begin{aligned}\mathbf{v} &= \frac{1}{\theta}\left[\frac{\Delta\mathbf{x}}{\Delta t} - (1-\theta)\mathbf{v}_0\right] \\ \boldsymbol{\omega} &= \frac{1}{\theta}\left[\frac{\Delta\boldsymbol{\alpha}}{\Delta t} - (1-\theta)\boldsymbol{\omega}_0\right]\end{aligned}\quad (4.6)$$

where $0 \leq \theta \leq 1$. The stability properties of the θ -method are well known: for $\theta = \frac{1}{2}$ an unconditionally stable and energy preserving scheme is recovered, for $\theta > \frac{1}{2}$ the scheme is unconditionally stable and dissipative, and for $\theta < \frac{1}{2}$ stability depends on the time step. In the context of binary collisions, the algorithmic energy dissipation that occurs for $\theta > \frac{1}{2}$ can be related to the physical dissipation associated with impact and thus to the restitution

coefficient e through the relation

$$e = \frac{1 - \theta}{\theta} \quad (4.7)$$

Indeed, as shown in [72], a value of $\theta = \frac{1}{2}$ corresponds to an elastic collision while $\theta = 1$ reproduces a perfectly inelastic collision. Binary elastic and plastic collision tests are shown in Appendix A.2.

4.2.4 Variational formulation of contact problem

Following the formulation procedure as described in [51; 72; 99; 104], the resulting discrete mixed force-displacement problem, including contact constraints, takes the form:

kinetic energy $1/2mv^2$ $1/2lw^2$ the following are all WORK!

$$\begin{aligned} \text{objective function} \quad & \min_{\Delta\boldsymbol{x}, \Delta\boldsymbol{\alpha}} \max_{\boldsymbol{p}, \boldsymbol{q}} \quad \left\{ \frac{1}{2} \Delta\boldsymbol{x}^T \bar{\boldsymbol{M}} \Delta\boldsymbol{x} - \Delta\boldsymbol{x}^T \bar{\boldsymbol{f}}_0 \right\} && \text{translational kinetic energy} \\ & + \left\{ \frac{1}{2} \Delta\boldsymbol{\alpha}^T \bar{\boldsymbol{J}} \Delta\boldsymbol{\alpha} - \Delta\boldsymbol{\alpha}^T \bar{\boldsymbol{m}}_0 \right\} && \text{rotational kinetic energy} \\ & + \left\{ \Delta\boldsymbol{x}^T (\boldsymbol{N}_0 \boldsymbol{p} + \widehat{\boldsymbol{N}}_0 \boldsymbol{q}) - \boldsymbol{g}_0^T \boldsymbol{p} - \Delta\boldsymbol{\alpha}^T (\boldsymbol{R}_0^q \boldsymbol{q} + \boldsymbol{R}_0^p \boldsymbol{p}) \right\} && \begin{matrix} \text{tangential momentum} \\ \text{normal momentum} \end{matrix} \\ & - \left\{ \frac{1}{2} \boldsymbol{p}^T \boldsymbol{C}_N \boldsymbol{p} + \frac{1}{2} \Delta\boldsymbol{q}^T \boldsymbol{C}_T \Delta\boldsymbol{q} \right\} && \text{work by other forces} \end{aligned} \quad (4.8)$$

subject to $\|\boldsymbol{q}\| - \mu \boldsymbol{p} \leq \mathbf{0}, \quad \boldsymbol{p} \geq \mathbf{0}$ coulomb constraint

With a slight abuse of notation, we have denoted the vector containing the absolute values of the shear forces by $\|\boldsymbol{q}\|$. The matrix \boldsymbol{N} contains all the normals associated with potential contacts $\boldsymbol{n} = (n_x, n_y)^T$ while the matrix $\widehat{\boldsymbol{N}}$ has the same form contains entries $\boldsymbol{t} = (-n_y, n_x)^T$, i.e., the tangent vector defined as the 90° counterclockwise rotation of \boldsymbol{n} . We note the presence of the term with incremental shear $\Delta\boldsymbol{q} = \boldsymbol{q} - \boldsymbol{q}_0$, which requires the tracking of shear forces at contact points and makes the problem history-dependent.

In equation (4.8), the matrix \boldsymbol{R}_0^q contains the contribution of the total angular momentum balance from the tangential forces and contains entries $\boldsymbol{R}_{iI}^T \boldsymbol{n}_0$ where \boldsymbol{R}_{iI} is the moment arm vector extending from the centroid of particle i to the contact point $\bar{\boldsymbol{y}}$. The matrix \boldsymbol{R}_0^p contains the contribution of the total angular momentum balance from the normal contact forces and contains entries $-\boldsymbol{R}_{iI}^T \boldsymbol{t}_0$. Both $\boldsymbol{R}_{iI}^T \boldsymbol{n}_0$ and $-\boldsymbol{R}_{iI}^T \boldsymbol{t}_0$ are signed moment arms and their signs depend on whether the associated contact force induces a positive (clockwise) or negative moment on the particle. A similar description applies to the slave particle using its contact normal $-\boldsymbol{n}_0$ and tangent $-\boldsymbol{t}_0$. The matrices \boldsymbol{C}_N and \boldsymbol{C}_T contain the compliances

$1/k_N$ and $1/k_T$ on the diagonal, where k_N and k_T are the normal and tangential contact stiffnesses, respectively. Finally, the Coulomb criterion is imposed with $\mu = \tan \phi$ being the effective interparticle friction coefficient and ϕ is the effective friction angle at the scale below the particle angularity level.

4.2.5 Optimality conditions

Following the approach in [72], the first-order KKT conditions associated with equation (4.8) give the linear moment balance:

$$\bar{\mathbf{M}}\Delta\mathbf{x} + \mathbf{N}_0\mathbf{p} + \widehat{\mathbf{N}}_0\mathbf{q} = \bar{\mathbf{f}}_0 \quad (4.9)$$

balance of angular momentum:

$$\bar{\mathbf{J}}\Delta\boldsymbol{\alpha} - \mathbf{R}_0^q\mathbf{q} - \mathbf{R}_0^p\mathbf{p} = \bar{\mathbf{m}}_0 \quad (4.10)$$

sliding friction conditions:

$$\|\mathbf{q}\| - \mu\mathbf{p} + \mathbf{s} = \mathbf{0}, \mathbf{s} \geq \mathbf{0} \quad (4.11)$$

$$\text{diag}(\mathbf{s})\boldsymbol{\lambda} = \mathbf{0}, \boldsymbol{\lambda} \geq \mathbf{0} \quad (4.12)$$

where \mathbf{s} is the slack vector, introduced to enforce equality, and kinematics:

$$\mathbf{N}_0^T\Delta\mathbf{x} + \mu\boldsymbol{\lambda} = \mathbf{g}_0 + \mathbf{C}_N\mathbf{p} \quad (4.13)$$

$$\widehat{\mathbf{N}}_0^T\Delta\mathbf{x} - (\mathbf{R}_0^{qT} + \mathbf{R}_0^{pT})\Delta\boldsymbol{\alpha} = \text{sgn}(\mathbf{q})\boldsymbol{\lambda} + \mathbf{C}_T\Delta\mathbf{q} \quad (4.14)$$

where sgn is the signum function. The kinematics in equations (4.13) and (4.14) pertain to the associated sliding rule, which leads to an apparent dilation proportional to the friction coefficient μ . However, as described in [72], this dilation can be viewed as an artifact of the time discretization which, with the exception of a few pathological cases, is gradually reduced as the time step is reduced. Moreover, it was shown in [72] that the dilation, even for rather large time steps, is negligible over a range of common conditions, including both instances of highly dynamic and relatively unconfined flows as well as confined quasi-static deformation processes. The consequences of the associated sliding rule are discussed in

Appendix A.3.

4.2.6 Force-based problem

Finally, it is possible to cast equation (4.8) in terms of the following force based problem:

$$\begin{aligned} \text{minimize} \quad & \frac{1}{2} \mathbf{r}^T \bar{\mathbf{M}}^{-1} \mathbf{r} + \frac{1}{2} \mathbf{t}^T \bar{\mathbf{J}}^{-1} \mathbf{t} + \mathbf{g}_0^T \mathbf{p} \\ & + \frac{1}{2} \mathbf{p}^T \mathbf{C}_N \mathbf{p} + \frac{1}{2} \Delta \mathbf{q}^T \mathbf{C}_T \Delta \mathbf{q} \\ \text{subject to} \quad & \mathbf{r} + \mathbf{N}_0 \mathbf{p} + \widehat{\mathbf{N}}_0 \mathbf{q} = \bar{\mathbf{f}}_0 \\ & \mathbf{t} - \mathbf{R}_0^q \mathbf{q} - \mathbf{R}_0^p \mathbf{p} = \bar{\mathbf{m}}_0 \\ & \|\mathbf{q}\| - \mu \mathbf{p} \leq \mathbf{0}, \quad \mathbf{p} \geq \mathbf{0} \end{aligned} \quad (4.15)$$

where \mathbf{t} is the dynamic vector associated with the rotations, i.e., torque vector.

4.2.7 Static limit

Omitting the dynamic forces \mathbf{r} and \mathbf{t} from equation (4.15) gives rise to the following static problem which is valid in the limit of Δt tending to infinity:

$$\begin{aligned} \text{minimize} \quad & \mathbf{g}_0^T \mathbf{p} + \frac{1}{2} \mathbf{p}^T \mathbf{C}_N \mathbf{p} + \frac{1}{2} \Delta \mathbf{q}^T \mathbf{C}_T \Delta \mathbf{q} \\ \text{subject to} \quad & \mathbf{N}_0 \mathbf{p} + \widehat{\mathbf{N}}_0 \mathbf{q} = \bar{\mathbf{f}}_{\text{ext}} \\ & \mathbf{R}_0^q \mathbf{q} + \mathbf{R}_0^p \mathbf{p} = \mathbf{0} \\ & \|\mathbf{q}\| - \mu \mathbf{p} \leq \mathbf{0}, \quad \mathbf{p} \geq \mathbf{0} \end{aligned} \quad (4.16)$$

The above principle is useful for quasi-static problems governed by an internal pseudo-time rather than physical time. Examples include common soil mechanics laboratory tests such as triaxial tests, quasi-static soil-structure interaction problems such as cone penetration, and various applications in the earth sciences where the time scales are such that the deformations are of a quasi-static nature (e.g., [106; 107]). We note that in the quasi-static formulation, the accuracy of the scheme would then depend on the increment size of the applied boundary conditions (e.g., wall displacements or stresses).

4.2.8 Solution procedure and computational complexity

We observe that equations (4.15) and (4.16) are essentially standard quadratic programming problems. In this work, the primal-dual interior-point solver in MOSEK [101] is used for the solution of both problems. The solution and storage costs associated with these problems are usually justified by the larger analysis steps that can be taken when using implicit algorithms. This is more so for systems comprised of rigid or highly stiff particles in which explicit solution procedures perform poorly or simply fail. Moreover, large-scale mathematical programming solvers with sparse storage (e.g., [100; 101]) are becoming widely available and increasingly efficient and robust. More recent solvers such as MOSEK [101] also include multi-core or multi-threaded capabilities.

The performance of the primal-dual interior-point method in the context of our proposed contact dynamics formulation has been described in detail in [72], and the following properties are summarized: 1) insensitivity of iteration count to problem size, 2) arithmetic complexity that is equivalent to standard Newton-Raphson schemes, and 3) highly robust (almost never fails or stalls). The overall cost is therefore comparable to implicit Newton-Raphson-type schemes used in nonlinear finite element analysis. For details on the fundamental theory and implementation of interior-point methods, we refer the reader to [108].

4.3 Contact Implementation

The CD formulation of either equation (4.15) or (4.16) described in the previous section offers great simplicity and significant effort reduction in contact implementation in that the only required information is the signed gap values at the initial time \mathbf{g}_0 . The implementation of the contact algorithm proceeds as described in Chapter 3, specialized to the 2D case.

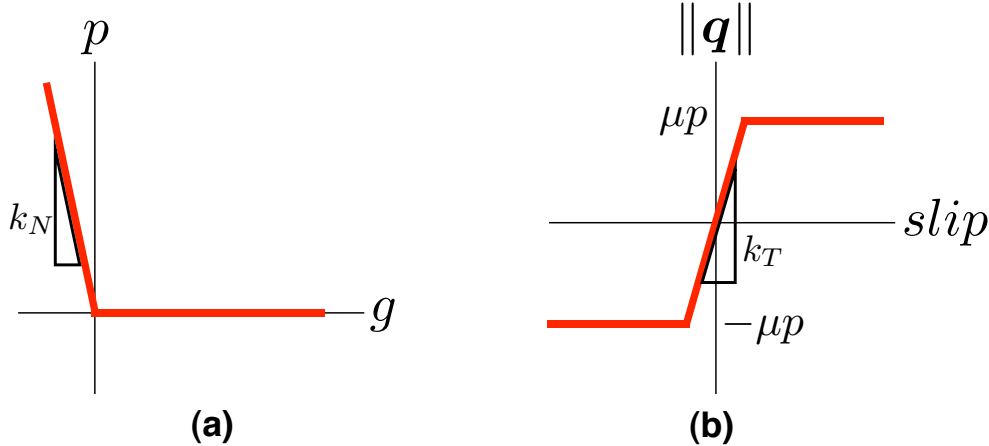


Figure 4.2: Linear elastic contact law: (a) normal reaction force p against separation or gap g and (b) friction force $\|\mathbf{q}\|$ against slip; μ is the friction coefficient.

Here, we have only considered the case of linear contact elasticity, as shown in Figure 4.2, but extension to nonlinear elasticity is entirely possible as is the consideration of more complex contact models incorporating hardening, viscous effects, etc. The resulting scheme bears some similarity to standard DEM schemes in that the consideration of a finite contact stiffness implies the possibility for an elastically reversible interparticle penetration. The inclusion of contact elasticity reproduces the more basic case of rigid particles in the limit of the contact stiffness tending to infinity. Moreover, in contrast to standard DEM, there are no algorithmic repercussions from operating with a large or, in the extreme case, infinite stiffness, reproducing the contact law shown in Figure 2.2. Indeed, the same algorithm is used regardless of the contact stiffness, with perfect rigidity being a limiting case that allows for certain simplifications. For example, in the limiting case, both C_N and C_T in either equation (4.15) or (4.16) are zero, and the associated quadratic terms drop out from the formulation. In particular, this means that no information of the shear forces needs to be carried over from one time step to the next. As a result, contact stiffness values that are representative of real materials (e.g., steel or rock) can be used without causing numerical

difficulties.

The static problem described by equation (4.16) reveals a number of interesting properties related to the indeterminacy of force networks in granular media. It is well known that rigid particles lead to a situation where the force network solution is non-unique [109–112]. Setting $\mathbf{C}_N = \mathbf{C}_T = \mathbf{0}$ in equation (4.16) leads to a linear program where global optimality may be achieved by more than one set of forces. Conversely, for finite values of \mathbf{C}_N and \mathbf{C}_T , the solution is unique, i.e., there is a unique set of contact forces leading to the optimal value of the objective function.

4.4 Numerical Examples

In this section, we present two examples that highlight the effects of particle morphology on the macroscopic response of granular assemblies, as well as the robustness of our proposed method. In particular, we compare responses of assemblies with three levels of particle angularity: disk, angular but (strictly) convex, and non-convex particles.

4.4.1 Biaxial compression

Biaxial compression simulations using the static limit formulation in equation (4.16) are carried out on a rectangular assembly of initial width W_0 and initial height H_0 containing 1520 particles. First, an assembly with non-convex particles is prepared using 16 different shapes. Then, two additional assemblies — one with angular convex particles and another with disks — are also prepared. The particles in these assemblies are obtained by matching average particle diameters of the 16 non-convex shapes. Effectively, sphericity is kept constant and a comparison of effects of angularity is made. The three assemblies with their corresponding particle shapes are shown in Figure 4.3.

The non-convex and angular assemblies have an initial porosity of approximately 0.152, while the disk assembly has an initial porosity of approximately 0.176. The higher porosity of the disk assembly points to the inability of disks to match porosity by just simply matching average particle diameters. Indeed, a wider distribution of disk sizes would be required in this case to match the initial porosity of 0.152, which in turn would substantially increase the number of particles. In this regard, the use of disks to represent particle geometry introduces an unavoidable geometrical bias, which leads to packings with higher

porosities [91]. Nevertheless, in this example, we retain the disk assembly for comparison with the other two assemblies. Two interparticle friction coefficients $\mu = 0.3$ and 0.5 are used to gauge the effect of interparticle friction. The upper wall is moved downwards while the applied stress on the right wall σ_3 is maintained at 125 units. A total of about 150 steps are used to impose a total axial strain of approximately 0.21. The left and bottom walls are stationary. All walls are frictionless.

To show the effects of particle elasticity, we perform the tests with several values of particle elasticity: $k_N = \infty, 10^8, 10^6, 10^5$. The tangential stiffness is set at $k_T = 2k_N/3$, which is within the range for a physically consistent volumetric response in granular materials [99; 113]. At every time step, the current width W and current height H of the assembly box are tracked, and the stresses σ_1 and σ_3 computed using the contact forces of the particles impinging on the top and right walls, respectively. The results in terms of deviatoric stress $\sigma_1 - \sigma_3$ versus axial strain, $\epsilon_a = 1 - H/H_0$, and volumetric strain, $\epsilon_v = 1 - WH/(W_0H_0)$, versus axial strain are shown in Figures 4.4 through 4.7. We see that the macroscopic response at $k_N = 10^8$ is close to rigid. As k_N is lowered, a more elastic initial response is observed in which the sharp initial peak is progressively suppressed and the peak response lowers slightly. At $k_N = 10^5$, an initial slope in the deviatoric stress becomes visible and the corresponding volumetric strain response shows an initial compaction followed by volume expansion. The deformed configurations of the three assemblies for the case of $k_N = 10^8$ are shown in Figure 4.3.

In all cases, we note the following observations. For a particular assembly, the macroscopic deviatoric stress reaches a constant value that is independent of the elastic properties while the rate of volumetric strain tends to zero, in agreement with standard continuum plasticity theories. Comparing across the three assemblies with different particle angularity levels, however, we observe that both the peak strength and dilatancy increase with increasing angularity, i.e., from disks to non-convex. This latter observation is consistent with experimental evidence of increased strength with increasing angularity of the particles [1].

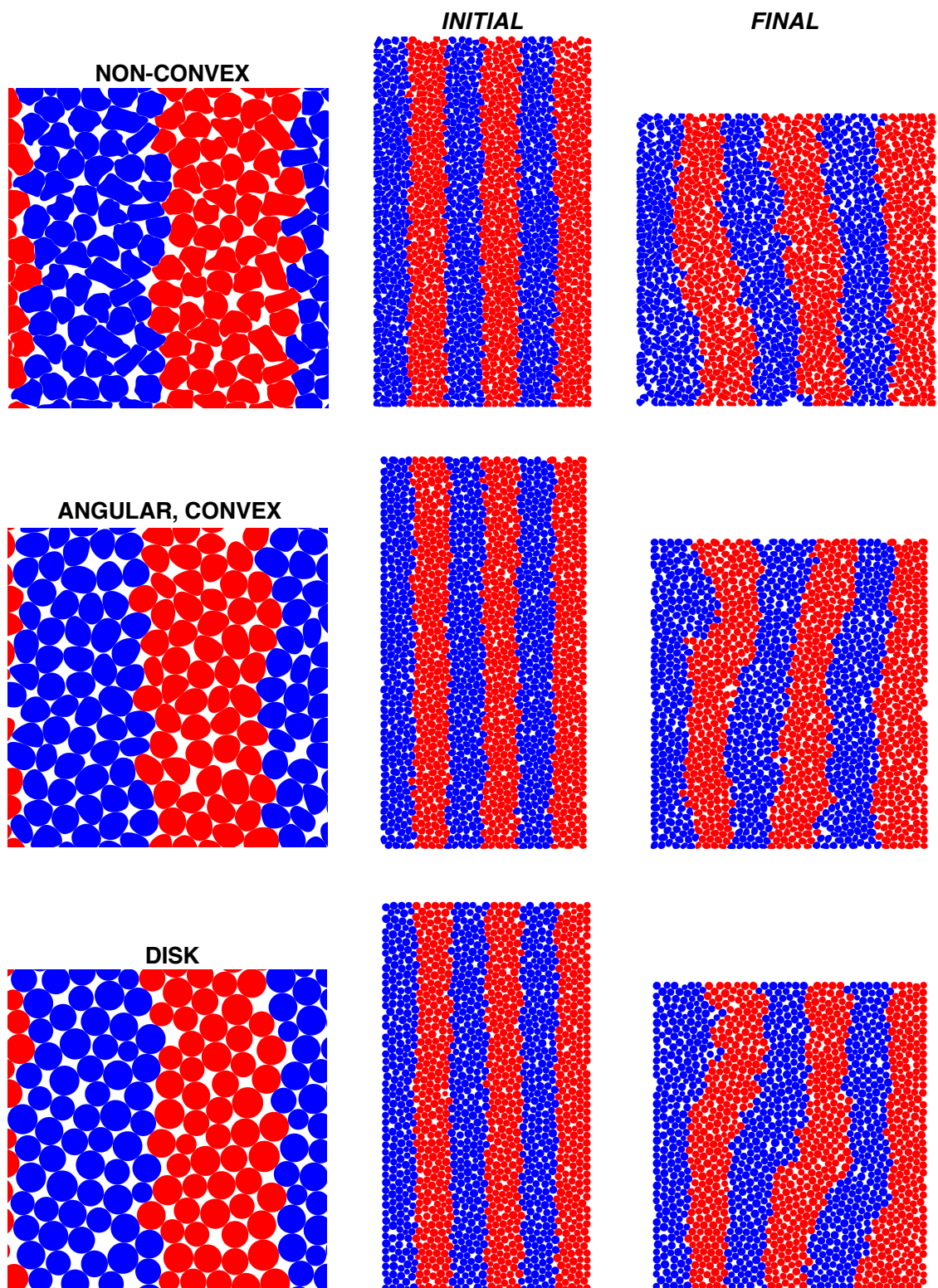


Figure 4.3: Biaxial compression: initial and final ($\epsilon_a = 0.21$) configurations with $k_N = 10^8$.

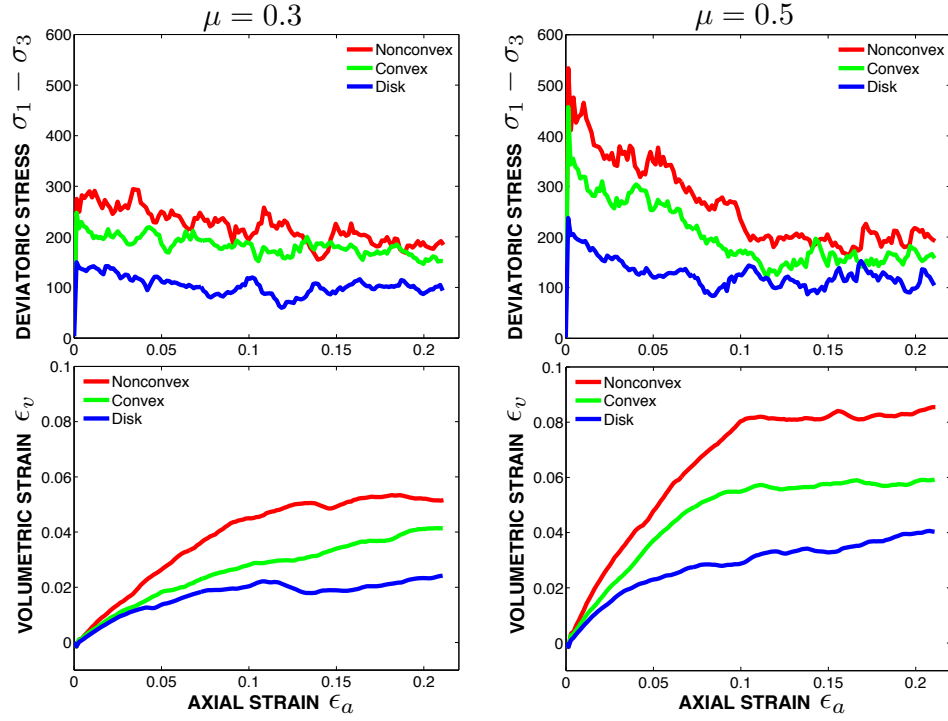


Figure 4.4: Biaxial compression: response with $k_N = \infty$.

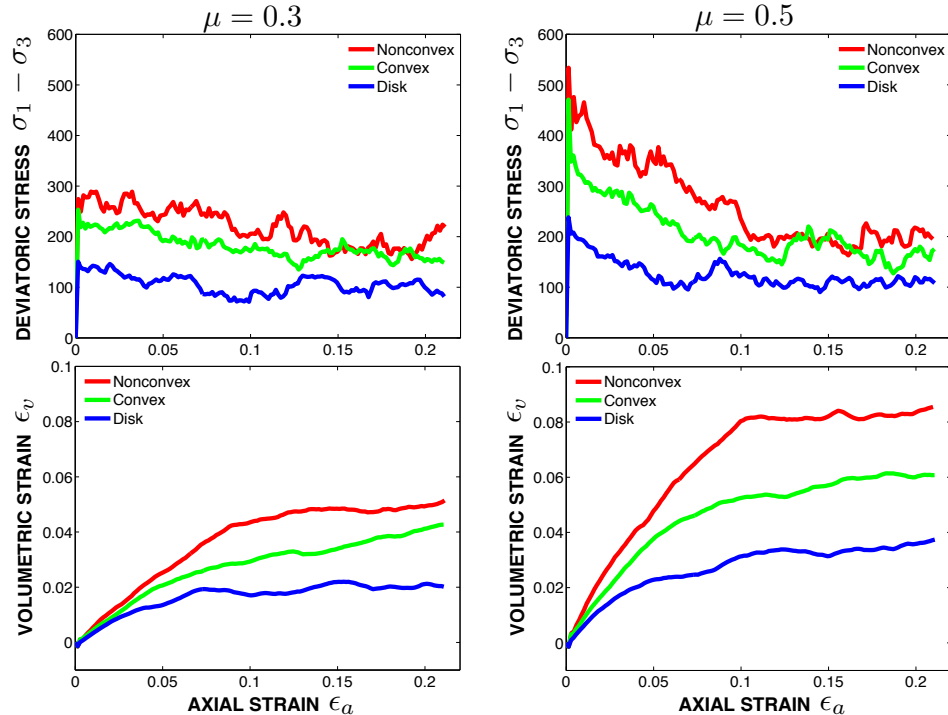
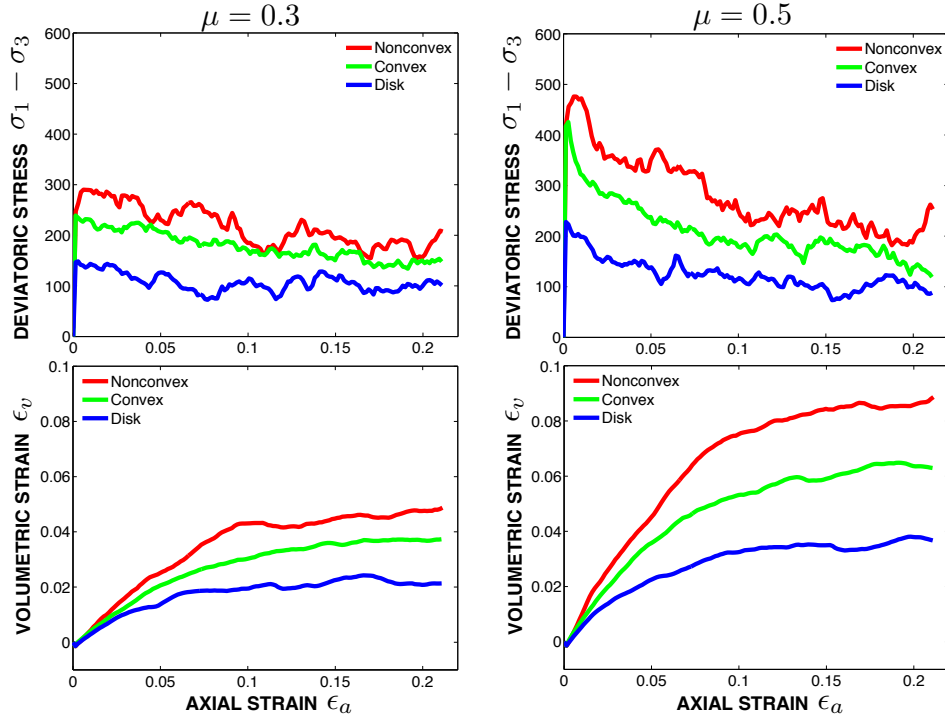
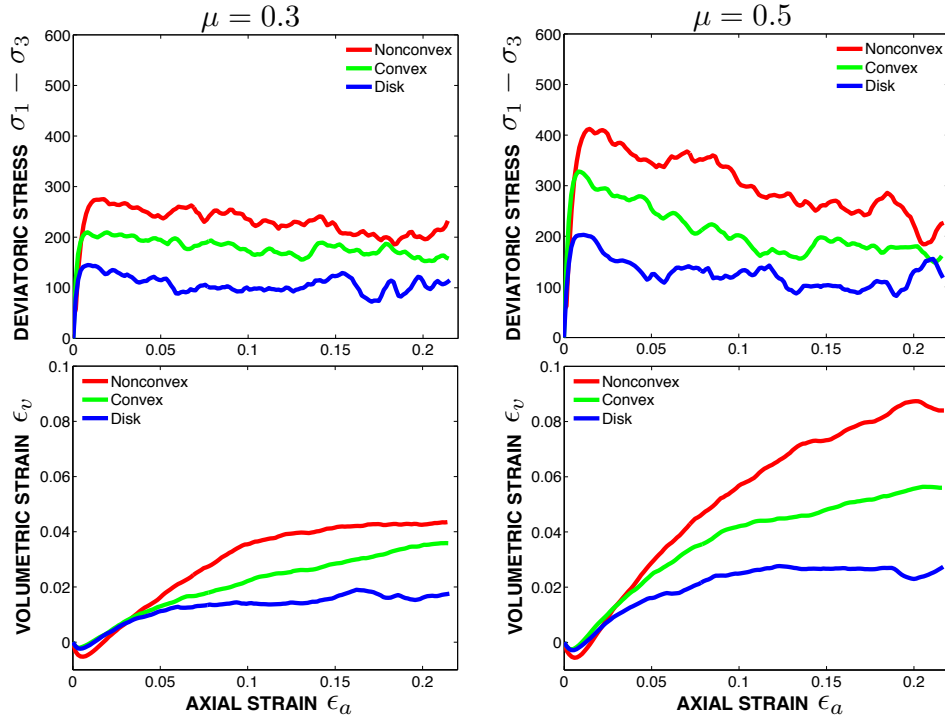


Figure 4.5: Biaxial compression: response $k_N = 10^8$.

Figure 4.6: Biaxial compression: response $k_N = 10^6$.Figure 4.7: Biaxial compression: response $k_N = 10^5$.

4.4.2 Column drop test

We consider a column with an initial height to width ratio H_0/L_0 of approximately 1.68. The base supporting the column has a friction coefficient of $\mu_{\text{base}} = 0.5$, while a smooth vertical wall representing a symmetry boundary is placed on one side of the column. Three columns with 1520 particles of increasing angularity — disk, angular but convex, and non-convex, as shown at Step 0 in Figures 4.8 and 4.9 — are constructed using particles from the sixteen different shapes described in the biaxial test example. These particles are dropped into the rectangular box that forms the column and settled under gravity. Drop test simulations are then conducted by removing one of the side walls of the box and letting the column spread under gravity. The simulations are carried out using the dynamic formulation in equation (4.15) with $\theta = 0.7$ and a time step of $\Delta t = 0.05$ for two interparticle friction coefficients $\mu = 0.5$ and $\mu = 0$. We set the contact elasticity to be $k_N = 10^8$ and $k_T = 2k_N/3$ for all columns.

We compare the response evolutions of the angular and disk columns against the non-convex column, as shown in Figures 4.8 and 4.9. The final configurations of the three columns for $\mu = 0.5$ are shown in Figure 4.10. The slopes of the final spreads of the angular and disk columns are approximately 12° and 9° , respectively. More prominently, the slope in the non-convex column is 17° . This is a 5° and 8° increase from the angular and disk columns, respectively, which is quite significant. Relative to the non-convex column, the final spreads of the angular and disk columns are approximately 14 and 45 percent wider. These observations are consistent with the increase of rolling resistance with increasing angularity.

For the case of $\mu = 0$, the response evolutions of the angular and disk columns as compared with the non-convex column are shown in Figures 4.11 and 4.12, with the final configurations of all columns shown in Figure 4.13. At Step 3200, the angular and non-convex columns have stopped flowing, while the disk column continues to flow and, as the simulation is progressed, a final layer thickness of 1 particle is reached. Essentially, without rolling resistance, the disk column simply ‘melts’ away. On the other hand, the angular and non-convex columns maintain a well-defined spread, even at zero interparticle friction, due to the rolling resistance provided by angular and non-convex particles. As expected, the non-convex column has a smaller spread due to increased angularity in the non-convex

particles.

4.5 Closure

We have presented a contact dynamics (CD) approach to our NURBS-based discrete method. By combining particle shape flexibility, properties of implicit time integration (e.g., larger time steps) and non-penetrating constraints, as well as a reduction to a static formulation in the limit of an infinite time step, we target system properties and deformation regimes in which the classical discrete element method either performs poorly or simply fail, i.e., in granular systems composed of rigid or highly stiff angular particles and subjected to quasi-static or dynamic flow conditions. The implementation the combined approach is made simple by adopting a variational framework, which enables the resulting discrete model to be readily solved using off-the-shelf mathematical programming solvers.

Numerical simulations of the biaxial compression and column drop tests for varying contact elasticities, including the rigid case, were performed, and the ability of the combined approach to capture the effects of increased rolling resistance, associated with increased angularity in and interlocking between non-convex particles, on the macroscopic response were clearly demonstrated. These effects are manifested macroscopically through an increase in the mobilized shear strength and dilatancy under biaxial compression, and a smaller spread and higher angle of response under a column drop test. These observations are consistent with reported experimental observations. The effect of geometrical bias from the use of disks to match average particle diameter on packing porosity, which in turn affects mobilized strength, is also noted.

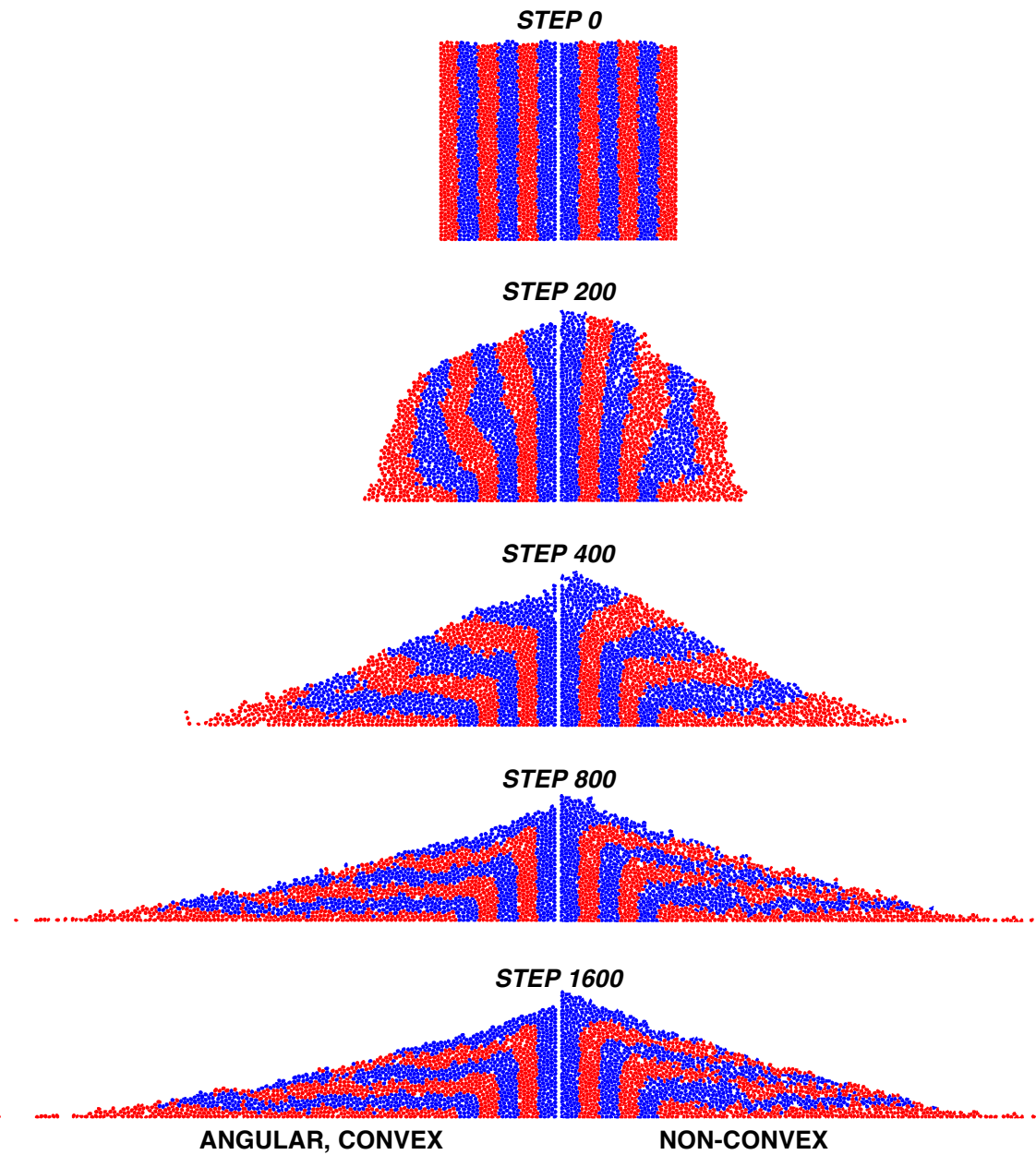


Figure 4.8: Column drop test with interparticle friction coefficient of $\mu = 0.5$: comparison between non-convex and angular particles.

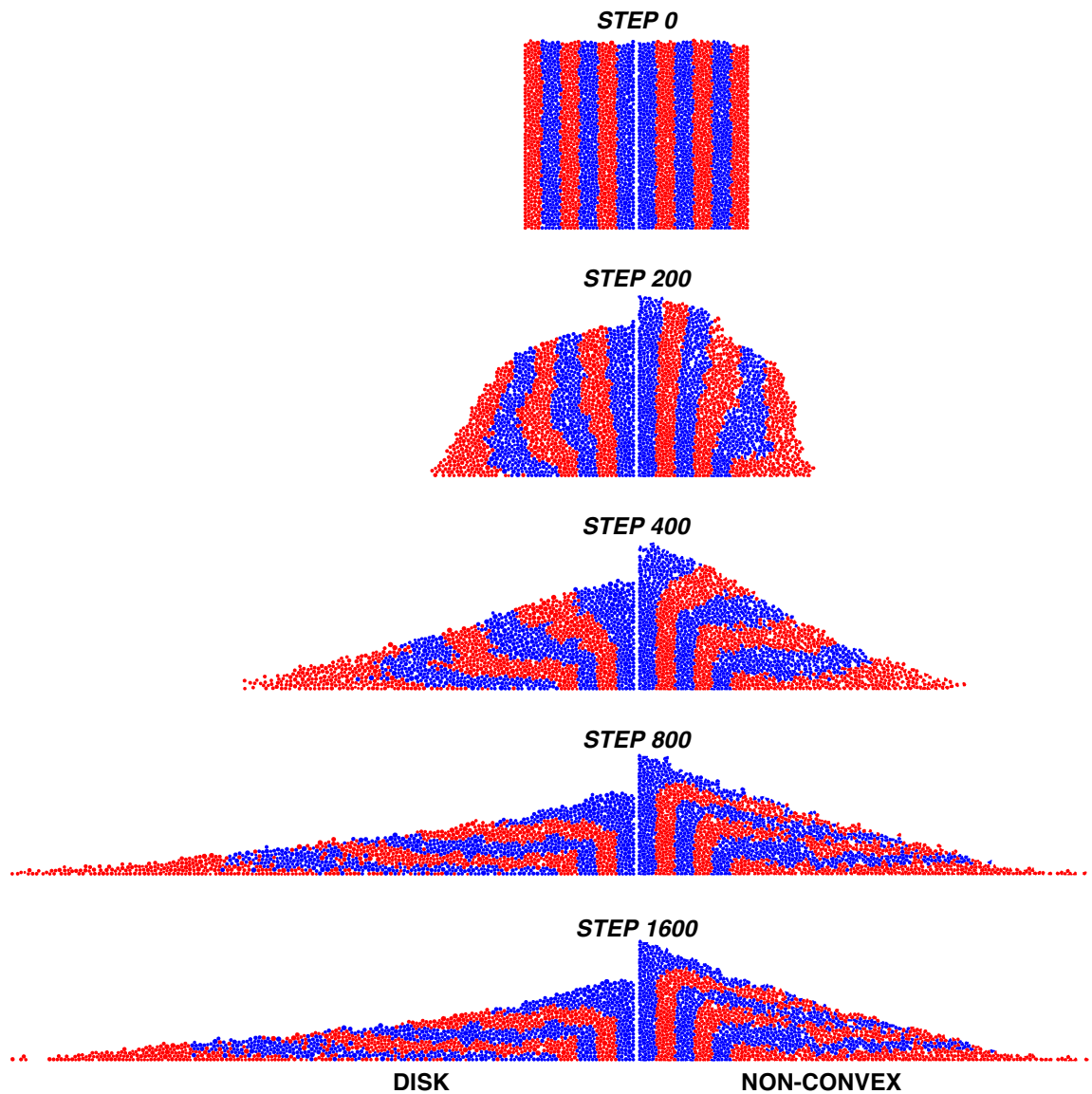


Figure 4.9: Column drop test with interparticle friction coefficient of $\mu = 0.5$: comparison between non-convex and disk particles.

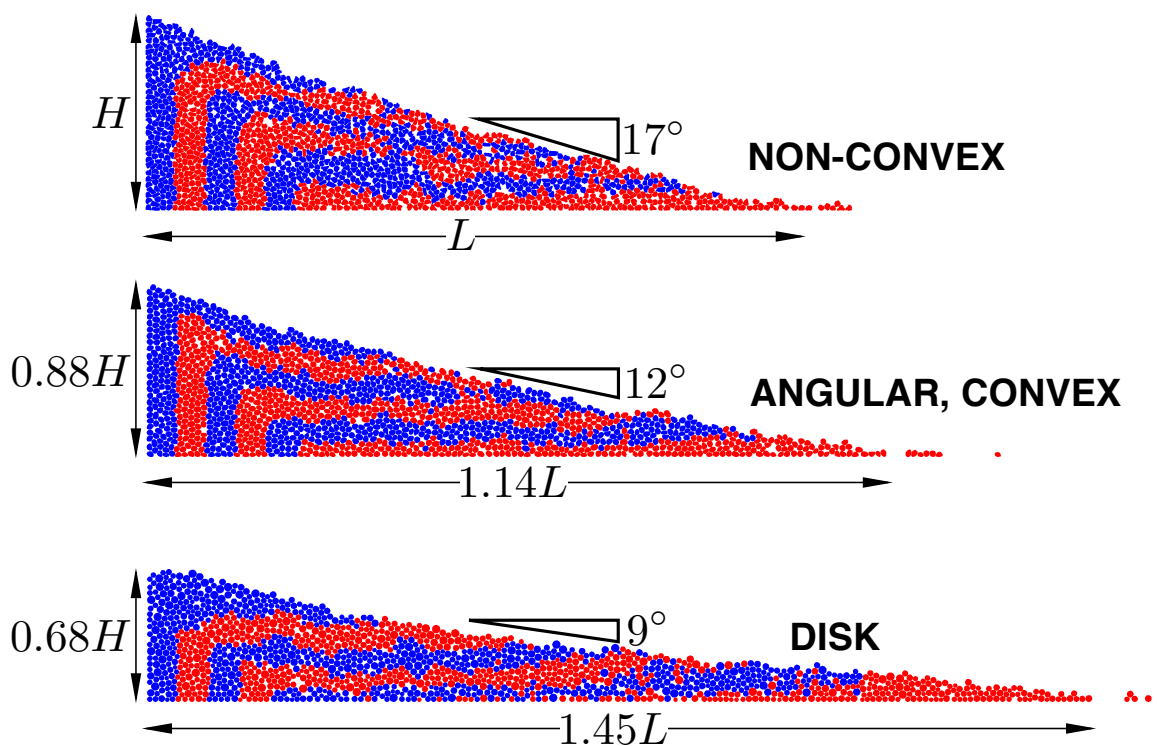


Figure 4.10: Configurations of columns with interparticle friction coefficient of $\mu = 0.5$ at step 1600: approximate dimensions relative to column with non-convex particles.

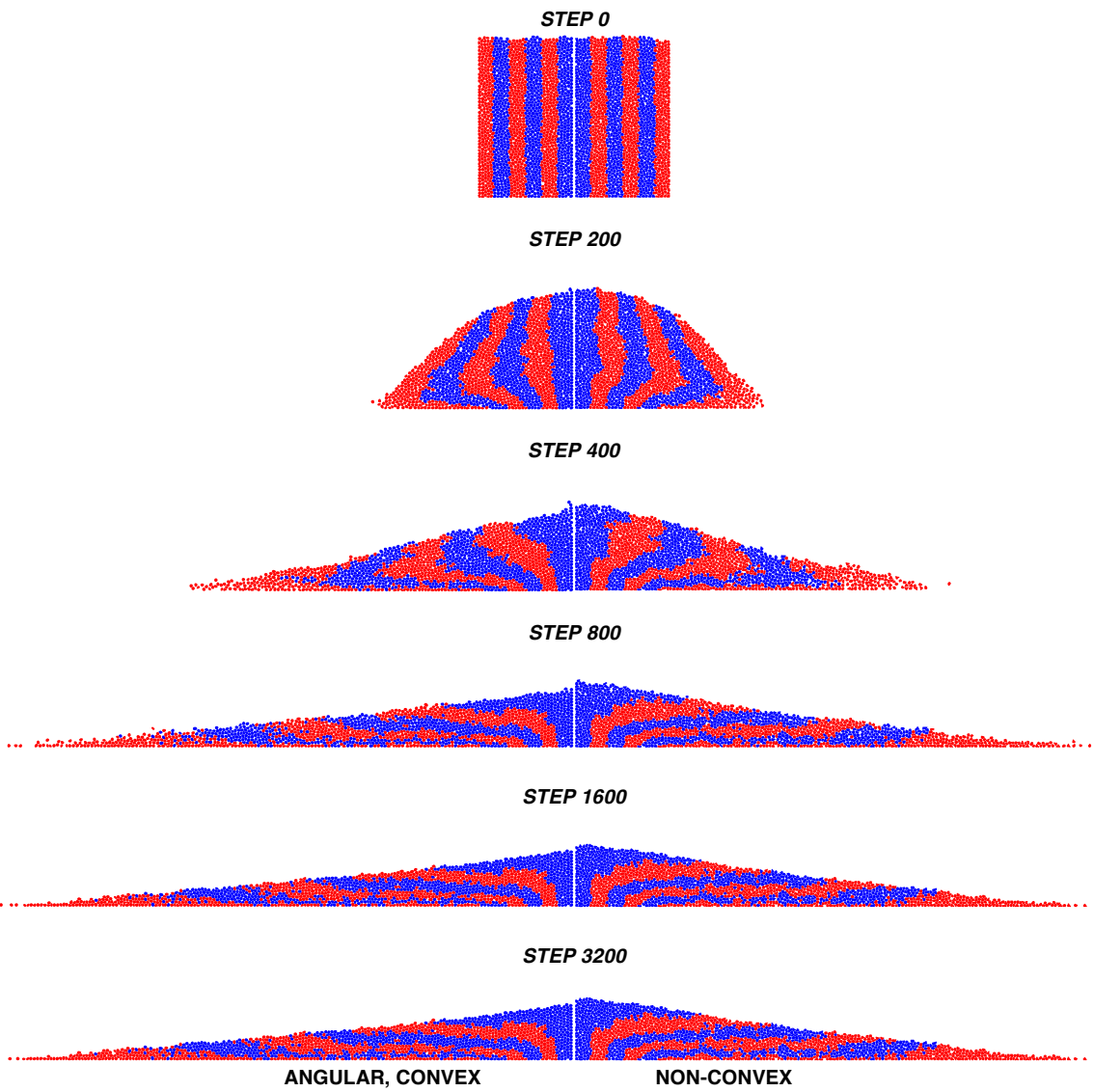


Figure 4.11: Column drop test with interparticle friction coefficient of $\mu = 0$: comparison between non-convex and angular particles.

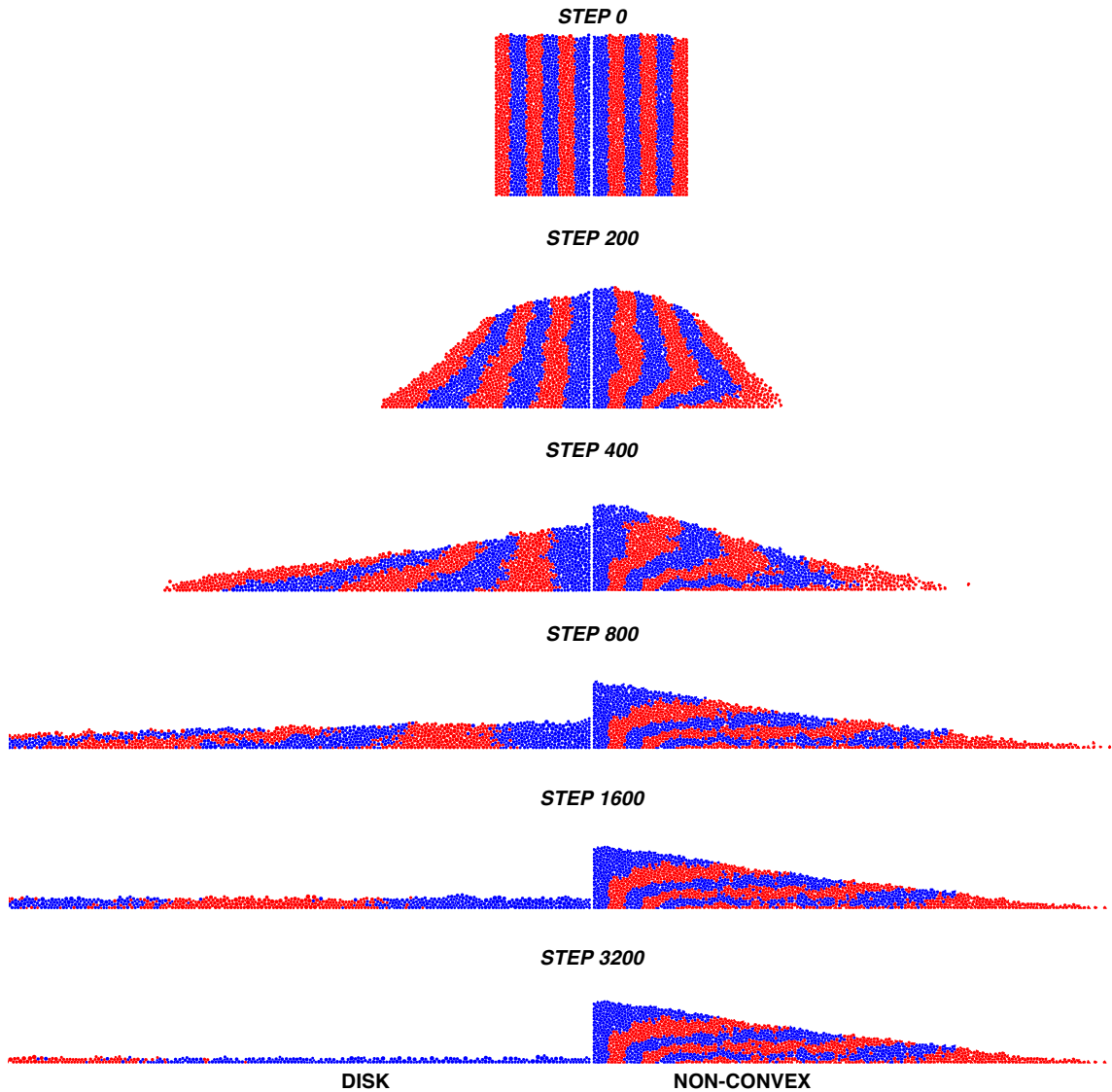


Figure 4.12: Column drop test with interparticle friction coefficient of $\mu = 0$: comparison between non-convex and disk particles. We note that at step 3200, the column with disk particles continues to flow; a final layer thickness of 1 particle is reached as the simulation is progressed.

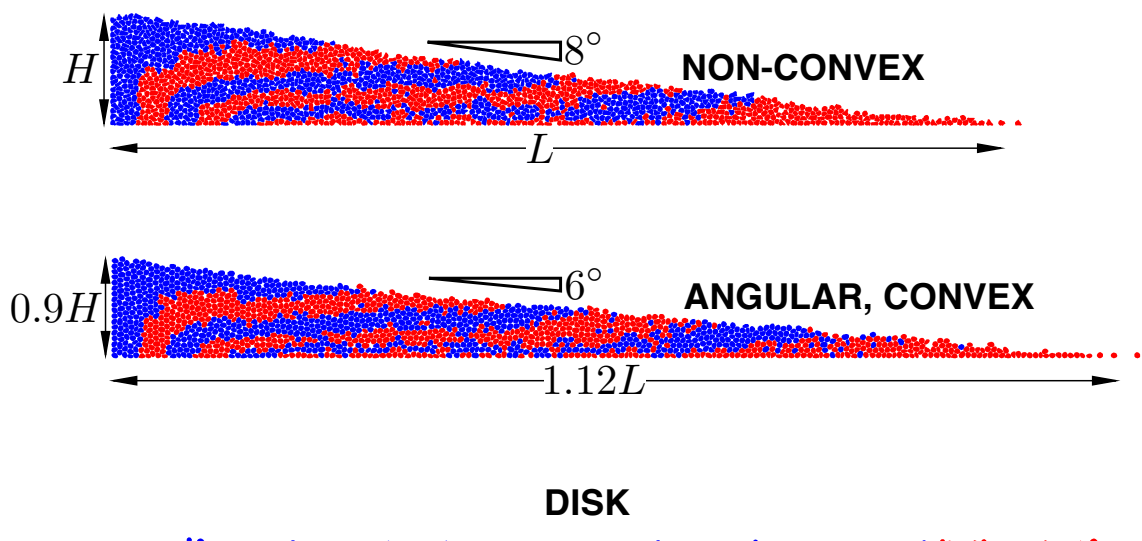


Figure 4.13: Configurations of columns with interparticle friction coefficient of $\mu = 0$ at step 3200: approximate dimensions relative to column with non-convex particles. We note that at this point in time the column with disk particles continues to flow; a final layer thickness of 1 particle is reached as the simulation is progressed.

Chapter 5

Multiscale Characterization and Modeling of Granular Materials through a Computational Mechanics Avatar: A Case Study with Experiment

5.1 Introduction

In recent times, much of solid mechanics research has focused around the ‘microstructures’ theme, which is predicated on the importance of lower-scale geometry, defects, and interaction to inform macroscopic behavior [114]. Crystalline solids have received significant attention, and progress in theory, experiment, and computation has been made to the extent that much of the research results can now be routinely applied in the design of such materials for real engineering applications. Granular materials also possess microstructures, which have far-reaching implications on macroscopic properties such as strength, permeability, and energy dissipation. Unlike crystalline solids, however, microstructures in granular materials lack order and cannot be elegantly quantified as in crystalline solids. Moreover, these microstructures operate at the grain scale, which neither atomistic nor continuum models can help in providing quantitatively meaningful results for real applications. To understand and predict the behavior of granular materials at the continuum scale, one must recognize that their mechanical behavior is encoded at the grain scale. We often point to this fact, despite the common knowledge that more than three decades of research has not led to significant advances in terms of performing grain-scale analysis and characterization

of real granular materials.

There are broadly two camps in the study of granular materials at the grain scale: that which seeks to characterize granular assemblies, often through imaging techniques such as X-ray computed tomography (XRCT), and that which seeks to simulate granular behavior, typically through the discrete element method (DEM). Characterization of granular materials has come a long way since the days of so-called ‘destructive’ methods, which involved dismantling experimental specimens to measure grain-scale quantities [115]. XRCT and other methods of digital imaging of experiments are now the norm in experimental grain-scale mechanics [17; 116], able to measure quantities such as the void ratio in a shear band [117] and track the motion of grains [118]. Increases in image fidelity and resolution have led to a number of characterization approaches such as level sets [47], spherical harmonics [119; 120] and Fourier analyses [121; 122] that can process image data to quantify grain kinematics and morphological measures (e.g., sphericity and roundness) [1]. Although characterization techniques have seen tremendous progress, they lack the ability to probe one crucial aspect of granular materials from which strength-related quantities are derived: interparticle contact forces. As such, a discrete model such as DEM remains a necessary component for the inference of contact forces. In the several decades following the inception of DEM [24], there were tremendous efforts in the development of shape representation capabilities and associated contact algorithms (e.g., [35–37; 40]). Currently, however, it appears that progress has hit a plateau with shape representations, largely belonging to either the polyhedra or clustering approach, still too crude for real grain-scale calculations. Incidentally, grain morphological measures from characterization rarely make their way into DEM because of incompatibilities between the geometry bases used in characterization and discrete models, and significant degradation of fidelity during the image-to-model process.

Despite great research efforts in each of the two microscopic camps, there is a surprising lack of interaction, and hence integration and validation, between them. In theory, both grain-scale characterization and discrete simulations should work in an integrated manner to provide a consistent set of microscopic information. In practice, however, this consistency is virtually nonexistent and surprisingly, not discussed in the literature. The reason for this void is that much of the problems making integration and validation difficult stem from the complexity of real grain geometries. For example, we described in an earlier work [22] two possible routes to using grain-scale information at the continuum level by means of a

hierarchical multiscale scheme: one using XRCT data and the other using discrete analysis. The consistency between the two routes, however, could not be established at the time since there was no DEM technology to account for the level of complexity of grain geometries found in experiment.

At the other end of the spectrum, multiscale methods are emerging to enable the use of grain-scale information at the continuum level. At this point, techniques linking the grain and continuum scales are based on homogenization theory [23]. It is important to point out that multiscale modeling is not just about developing algorithms but also about developing better physical models [123]. In the context of real granular materials, the effects of grain morphology on strength of granular materials have already been well established [1]. Although there have been significant efforts in constructing multiscale procedures (e.g., [124–131]), the predictive capabilities of these procedures on real granular materials have not been assessed due to the absence of any discrete model that is morphologically representative of real granular materials. Currently, the fidelity of the discrete model appears to be the missing ingredient to achieving a breakthrough in the predictive power of multiscale methods.

Here, we tackle the above challenges head-on by developing an overarching computational mechanics avatar that has enabled us to make the first steps in bridging the gap between characterization and discrete analysis, and potentially improving the predictive capabilities of multiscale methods. We integrate two major components of the proposed avatar, namely the level-set characterization technique and our NURBS-based DEM, and significantly enhance their capabilities to handle real grain morphologies. We then apply the avatar to characterize and model the grain-scale response inside the shear band of a real triaxial specimen. The avatar has enabled, for the first time, the transition from faithful representation of grain morphologies in X-ray tomograms of granular media to a morphologically accurate discrete computational model. Grain-scale information is extracted and upscaled into a continuum finite element model through a hierarchical multiscale scheme, and the onset and evolution of a persistent shear band is modeled, showing excellent quantitative agreement with experiment in terms of both grain-scale and continuum responses in the post-bifurcation regime. More importantly, consistency in results across characterization, discrete analysis, and continuum response from multiscale calculations is found, achieving the first and long sought-after quantitative breakthrough in grain-scale analysis

of real granular materials.

This chapter is organized as follows. First, we describe the characterization and computational components of the avatar, and the associated algorithmic improvements that enable faithful representation of grain morphologies directly from X-ray tomograms. Next, we present a case study where we describe the experiment of interest, followed by the characterization and modeling steps taken to arrive at the relevant grain-scale information and predicted continuum response. Finally, we close by providing an assessment of the strengths and validity of the components of the avatar, as well as limitations that are to be addressed in the future.

5.2 The Avatar Framework

A computational avatar aims to be the virtual twin of a granular assembly (e.g., sand), a digital mirror of grains as they are found in-situ. The avatar should also possess realistic mechanical properties (e.g., elasticity) and in a mechanistic context, behave similarly to the real grain assembly, so that grain morphologies, kinematics, arrangement, and elastostatics are all comparable to those of the physical assembly. The avatar opens the door for the use of the experimentally-derived grain-scale quantities in either forward simulation techniques (e.g., DEM) or inverse elastostatics analyses [2; 3]. These analyses would yield the quantitative measurements of contact forces throughout a granular assembly, allowing access to force chains or fabric evolution in real time in real granular assemblies.

In this section, we summarize the two major components of the proposed computational mechanics avatar that has made the image-to-model transition possible, namely the characterization toolbox used to capture grain morphologies and our NURBS-based DEM for discrete analysis. In particular, we focus on the relevant algorithmic improvements. Earlier, these components have been briefly discussed in [4] and developed independently [47; 49]. Here, we integrate these two components for the first time to enable the application of the avatar to a real problem.

5.2.1 Characterization toolbox

Successful inference of kinematics and contacts provides several important applications concerning the evolution of strength in granular systems, namely:

1. Determination of grain kinematics and grain fabric, including contact evolution during loading.
2. Inference of contacts locations. Together with strains or stresses from X-ray diffraction [19], contact locations provide necessary input for a technique for quantitative inference of contact forces in opaque granular systems [2; 3].
3. Inference of grain morphologies that are representative of true grains (to within imaging resolution). These serve as geometry input to discrete methods that can account for arbitrary grain shapes (see Section 5.2.2).

The use of XRCT in an experiment (e.g., triaxial test) provides, in addition to macroscopic stress and strain data, a sequence of three-dimensional (3D) of voxelated images (see Figure 5.1), each containing tens of thousands of grains, collected over the course of the specified loading regime. The challenge in applying XRCT is in translating the 3D images into quantities that can be used for mechanical analysis, i.e., to translate image voxels into grain fabric and morphology. The key difficulty underlying this translation process lies in the irregularity of individual grains and that they are in contact with each other.

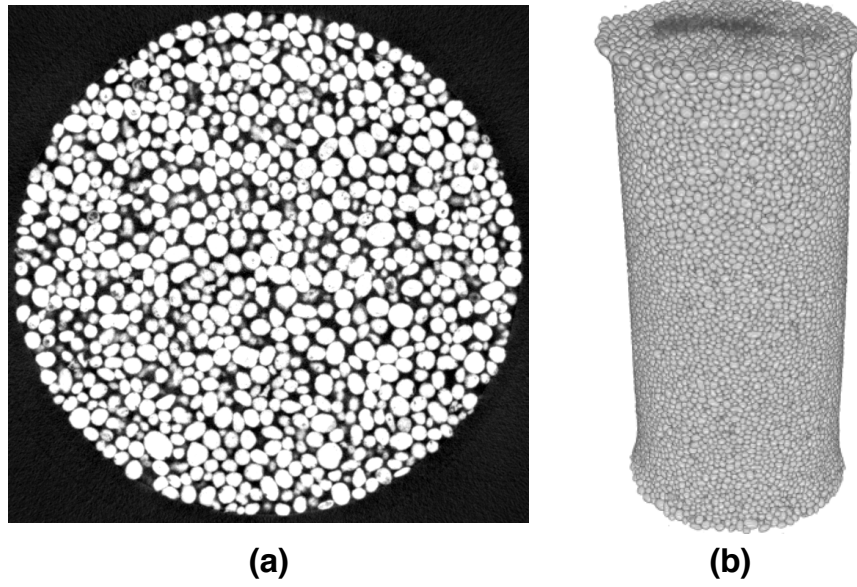


Figure 5.1: Grain-scale imaging using XRCT: (a) slice of triaxial specimen and (b) 3D reconstruction by stacking slices.

The watershed technique [132] has been a trusted workhorse for segmenting grains from the voids, and from each other. Watershed, however, has the drawback of generally oper-

ating on and outputting binary images. This is problematic for two reasons. The first is that binary images introduce artificial roughness to grain surfaces, complicating a direct tomography-to-simulation paradigm [4]. The second, and more critical, drawback is the removal of details about the location and orientation of interparticle contact, which impedes our understanding of the physical sources of mechanical strength.

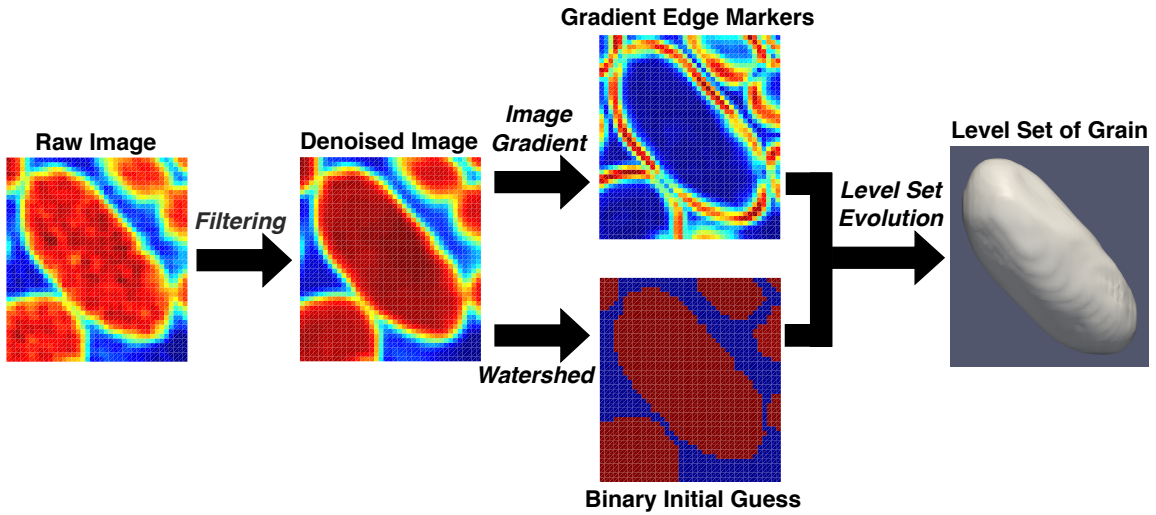


Figure 5.2: Summary of characterization steps: (left) slice of 3D XRCT volume of voxels, (middle two) application of proposed characterization technique, and (right) generated grain.

We overcome the above difficulties by applying the characterization methodology proposed in [47] to operate on the following key areas to delineate grain surfaces and contact locations. Briefly, the steps in the proposed methodology are:

1. Use of full-fidelity 3D XRCT image instead of binary images. The image is filtered to furnish precise edge markers via the first and second gradients of X-ray attenuation.
2. Noise removal. The use of image gradients necessitates the removal of noise. Non-local de-noising is utilized and guided by input parameters across different materials and X-ray attenuation spectra.
3. The search for grain edges via level sets. Speed up in convergence is obtained using the edge markers and current segmentation techniques (e.g., watershed) as initial conditions. The level sets are allowed to evolve until the boundary of grain is identified and, consequently, mathematically characterized.

The above steps produce grain boundaries that are smooth and representative of true grain shapes to sub-voxel accuracy, and without ‘melt’ near contact, as shown in Figure 5.2. In essence, the proposed methodology converts digital computed tomographic images into a collection of grain avatars, i.e., digitized versions of natural grains, which are transferred into a discrete computational model, as described next.

5.2.2 NURBS-based discrete element method

We employ a discrete element method that uses Non-Uniform Rational Basis-Splines (NURBS) as the mathematical basis for representing grain geometries [49]. The initial developments of this approach focused on strictly convex grains [49–51]. The generation of strictly convex NURBS shapes, however, is very difficult and restrictive from a modeling perspective. This is even more so when dealing with image data of real grain shapes and obtaining strictly convex shapes is not possible in most cases. This difficulty is not due to some limitation of NURBS but to the state of the contact algorithm for NURBS, which were undeveloped at the time.

A contact algorithm capable of dealing with general non-convex NURBS surfaces would eliminate the above modeling difficulty. We achieve this by generalizing the node-to-surface approach typically used in the contact treatment of finite element models [92] to a knot-to-surface approach. Following a master-slave approach, a fixed contact point on the slave particle Ω^j is denoted by \mathbf{x} while the contact point on the master particle Ω^i is defined to be the closest point projection of \mathbf{x} onto the boundary of the master particle:

$$\bar{\mathbf{y}} \equiv \bar{\mathbf{y}}(\mathbf{x}) = \min_{\mathbf{y} \in \Gamma^i} \|\mathbf{x} - \mathbf{y}\| \quad (5.1)$$

where Γ^i is the boundary of the master particle. Here, \mathbf{y} is a function of the two variables parametrizing the NURBS surface. Knowing the normal \mathbf{n} at $\bar{\mathbf{y}}$, the gap is then calculated as:

$$g(\mathbf{x}) = (\mathbf{x} - \bar{\mathbf{y}}(\mathbf{x}))^T \mathbf{n} \quad (5.2)$$

from which the effective normal contact force on grain Ω^i at $\bar{\mathbf{y}}$, assuming a linear elastic

stiffness model, is calculated:

$$\mathbf{f}_n^i = \begin{cases} k_N g \mathbf{n}, & \text{if } g < 0 \\ \mathbf{0}, & \text{otherwise} \end{cases} \quad (5.3)$$

where k_N is the normal elastic stiffness and $g \mathbf{n}$ measures the penetration or overlap in vector form.

The above approach is described in [52] for the two-dimensional (2D) case and here, we generalize this to 3D as follows. As a pre-processing step, we first perform a least-squares NURBS fitting procedure on the level set surfaces generated from the characterization step. Then, we apply a NURBS recursive subdivision procedure [50] to generate a set of fixed knots or nodes on each grain. The NURBS surface is subdivided until the following termination criteria (see Figure 3.3) are met:

1. Real space arc distance corresponding to each parametric direction of less than ϵ_d
2. Acute angle between normal vectors at adjacent knot positions of less than ϵ_θ

and a knot or node is positioned at the center of the subdivided surface at the terminated level (see Figure 3.3).

During simulation, we take advantage of the parametric nature of NURBS and solve the 3D closest point projection problem (5.1) using a two-stage optimization strategy: the proximity of the location of the closest projected point is established, followed by a local constrained optimization step to finalize the closest point location. The first optimization stage is handled using the DIviding RECTangles (DIRECT) global optimization algorithm [94], which effectively deals with non-convex objective functions and hence, non-convex grain shapes, while the second stage is handled using standard derivative-free optimization techniques [98]. This two-stage strategy eliminates all the major problems associated with intersection-based approaches to computing the interparticle gap or overlap (high computational cost, data proliferation, and convexity restriction) in the early version of our NURBS-based DEM [50]. Moreover, this procedure can be formulated and implemented with equal ease as in the 2D case.

5.3 Case Study

The purpose of the case study is to apply and assess the predictive capabilities of the avatar in a real experiment. This is achieved as follows. First, the localized incremental displacement fields and global stress-strain curve are extracted from experiment and used in a hierarchical multiscale computation to reproduce the continuum response. In this process, we obtain two quantities of interest in the shear band, namely the average dilatancy evolution and residual shear strength. Then, unit cells in the shear band are modeled using NURBS, and the same two quantities above are extracted and compared with those inferred from experiment. Below, we describe the experiment setup followed by the characterization and modeling steps leading to the final assessment.

5.3.1 Experiment setup

A cylindrical specimen (11 mm diameter by 24 mm height) of Caicos ooids (a natural granular material with well-rounded grains) was sheared at a constant axial strain rate of 0.1%/min under a constant cell pressure of 100 kPa in a specially designed triaxial cell in Laboratoire 3SR [133]. Tomographic images were captured at 18 stations during the test with a voxel size of $15.56^3 \mu\text{m}^3$, to be compared to a mean grain diameter $420 \mu\text{m}$. The global deviator stress as a function of the axial strain is shown in Figure 5.3. The behavior is typical of a dense sand, with a peak in the deviator stress followed by softening and subsequent residual or critical state and dilatant behavior throughout. The progressive formation of a shear band was observed during the test, with a final shear band inclination of approximately 52° with respect to the horizontal, and a thickness of approximately 8 grains.

5.3.2 Dilatancy inference

The dilatancy evolution in the shear band is inferred from grain-scale kinematics. Digital image correlation (DIC) is used in concert with tomographic images to compute incremental displacement vectors in elements containing 3^3 grains on average. The result is a 3D incremental displacement field for the entire triaxial specimen at all tomographic measurement stations. For example, Figure 5.4 shows the incremental displacement field between tomographic stages 6 and 7 (post-peak in the load-displacement curve). Some large incre-

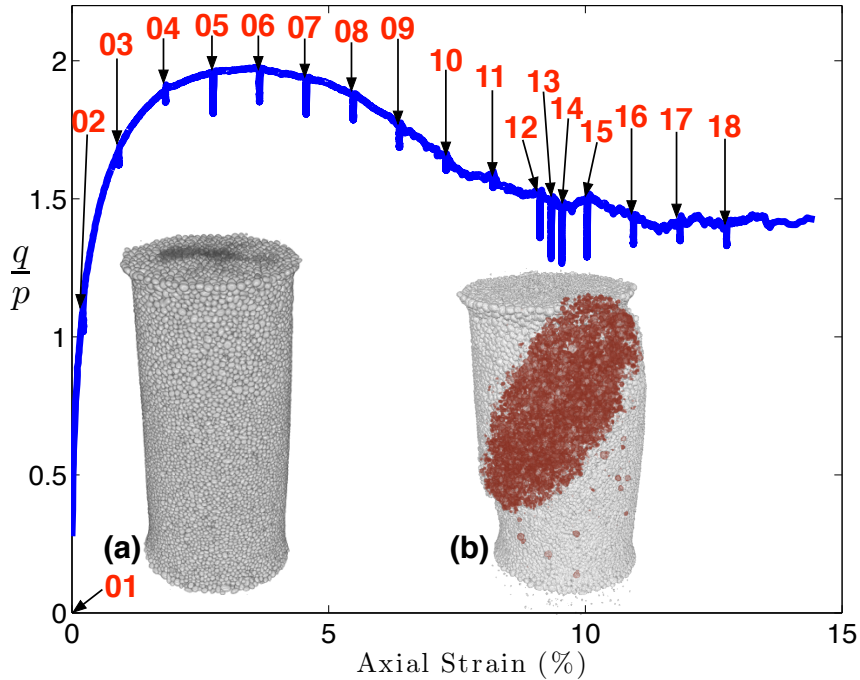


Figure 5.3: Macroscopic load-displacement response. Inserts: triaxial specimen at (a) initial state and (b) 9.11 % axial strain, with shear band highlighted. Station numbers are labeled in red.

mental displacements are observed in the elements at the specimen boundary, a product of the boundary effects stemming from the DIC technique itself and the specimen membrane; these edge elements are excluded from subsequent dilatancy calculations.

Following a finite element interpolation approach, we calculate the incremental strain over an element e as:

$$\Delta\boldsymbol{\epsilon}^e = \mathbf{B}^e \Delta\mathbf{d}^e \quad (5.4)$$

where $\Delta\mathbf{d}^e$ is the incremental displacement vector containing the nodal incremental displacements (from experiment as described above) and \mathbf{B}^e is the strain-displacement matrix in Voigt notation. Incremental strains are calculated over each Gauss point (eight integration points per trilinear brick element) and then used to compute the average incremental strain over the element as:

$$\Delta\boldsymbol{\epsilon}_v^e = \text{tr}\Delta\boldsymbol{\epsilon}^e \quad (5.5)$$

$$\Delta\boldsymbol{\epsilon}_s^e = \sqrt{\frac{2}{3}} \|\text{dev}\Delta\boldsymbol{\epsilon}^e\| \quad (5.6)$$

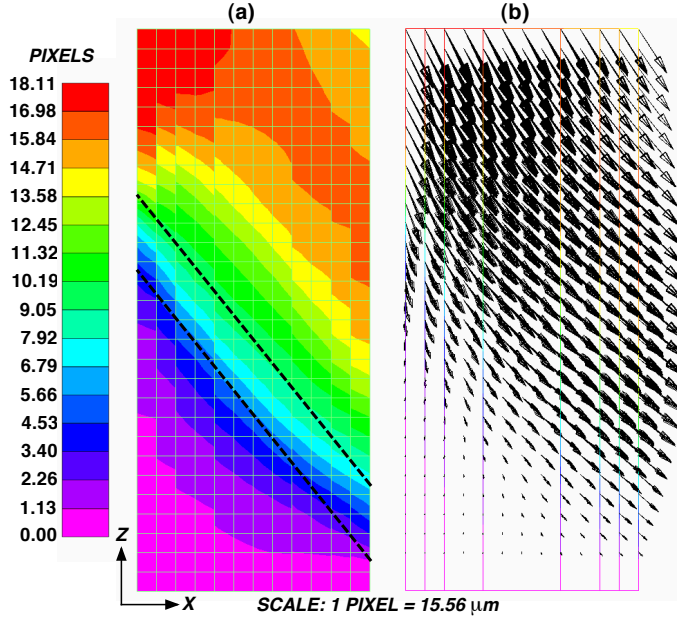


Figure 5.4: Incremental displacement field between tomographic stages 6 and 7 obtained from DIC: (a) contour of magnitude of incremental displacement vector with shear band within the region indicated by dashed lines and (b) incremental displacement arrows.

Based on the displacement field obtained from DIC, we identify the shear band region and all the elements within it. We note that the data shows that the deformations are fairly homogeneous throughout the shear band. With this, the average dilatancy in the shear band is calculated as:

$$\beta = \frac{\Delta \bar{\epsilon}_v}{\Delta \bar{\epsilon}_s} \quad (5.7)$$

and shown in Figure 5.5. Here, we have assumed that the elastic strain increments are negligible and their plastic counterparts dominate, allowing us to use the measured increments directly to quantify dilatancy.

5.3.3 Multiscale computation

To check that the average dilatancy evolution inferred from experiment is correct, an experimentally-driven multiscale computation was performed. Applying the hierarchical multiscale scheme proposed in [22], we upscaled the experimental average dilatancy evolution into a continuum finite element model of the triaxial specimen and the global structural responses of the model and experiment were compared.

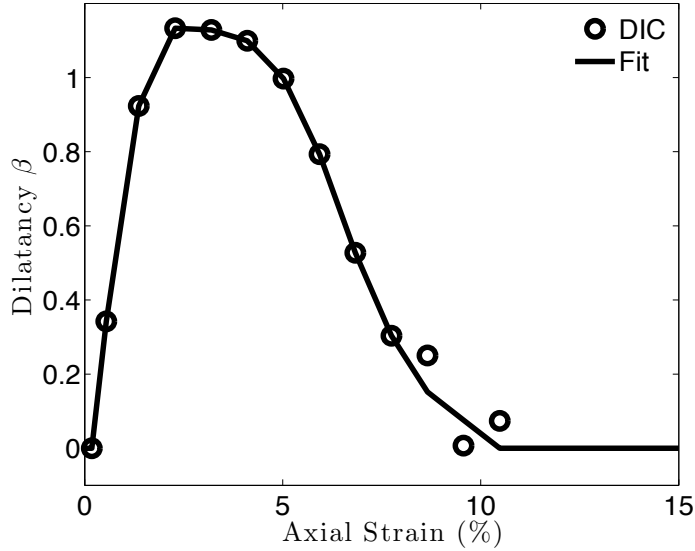


Figure 5.5: Dilatancy inferred from DIC data with fit for multiscale calculation (see Section 5.3.3).

Underlying the multiscale scheme, we use a Drucker-Prager constitutive model with the yield surface and plastic potential being:

$$F(p, q, \mu) = q + \mu p = 0 \quad (5.8)$$

$$Q(p, q, \beta) = q + \beta p - \bar{c} = 0 \quad (5.9)$$

respectively, where p, q are the pressure and shear invariants of the stress tensor, μ is the generalized friction coefficient, β is the (plastic) dilatancy, and \bar{c} is a free parameter such that the plastic potential crosses the yield surface at the same stress state (p, q) . Generally, the microscopic variables μ and β are obtained either through an experiment or a discrete model. For simplicity and convenience, however, we can invoke the stress-dilatancy relation $\mu = \beta + \mu_{cv}$ and express β as a function of μ . The resulting multiscale scheme would then require three calibrated material parameters — the elastic modulus E , Poisson's ratio ν , and residual shear strength μ_{cv} — plus a dilatancy evolution β inferred from experiment. For the experiment considered here, the calibrated parameters are $E = 125$ MPa and $\nu = 0.3$, $\mu_{cv} = 0.81$. When these parameters and the shear band dilatancy evolution β in Figure 5.5 are upscaled into the finite element model, the global response of the experiment is reproduced as shown in Figure 5.6.

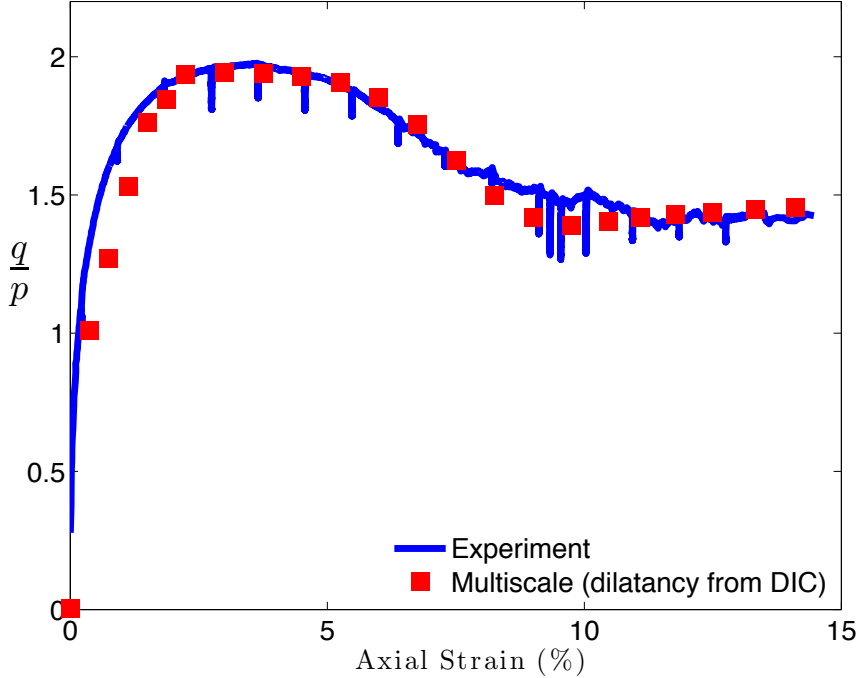


Figure 5.6: Global response from multiscale computation using dilatancy evolution information inferred from DIC (refer to Figure 5.5).

Remark 5.3.1 The elastic parameters E and ν are determined based on the assumption that the material is linear-elastic and homogeneous up to about 0.09% global axial strain, as is apparent from the initial steep linear portion of the global stress-strain curve. We further assume that the dilatancy in the shear band is zero during the elastic stage and evolves as shown in Figure 5.5. The elements outside the shear band are assumed to evolve identically except that the dilatancy value is maintained once the peak is attained. This produces a state of inhomogeneous deformation after stage 6 (around 4% axial deformation), where the bulk of the deformation and global response of the specimen starts to be governed by the evolution of the shear band.

Remark 5.3.2 We note that the above experiment cannot be used to probe the stresses locally and only local deformation fields can be reconstructed from the experimental data. Hence, only dilatancy β can be inferred from the experimental data. As such, a comparison of the evolution of frictional resistance μ inside the shear band between experiment and a discrete model cannot be directly made. One can, however, determine the adequacy of a discrete model by checking if the model residual strength is close to this calibrated value of μ_{cv} (see Section 5.3.4).

5.3.4 Discrete modeling

In the shear band identified in Section 5.3.2, two locations are arbitrarily selected for unit cell extraction. Starting from a 3D XRCT image at these locations, we apply the characterization step described in Section 5.2.1 to capture the morphologies of the grains. Subsequently, NURBS surfaces are fitted over the characterized grains for use in our NURBS-based DEM. Two discrete models are constructed (see Figure 5.7), each comprising of about 10^3 grains and with model thickness (~ 10 grains) that extends the full shear band thickness. We then apply the node generation procedure described in Section 5.2.2 with $\epsilon_d = 5$ voxels and $\epsilon_\theta = 10^\circ$, resulting in between 400 and 500 nodes per grain. For simplicity, we have constructed our model in voxel space. In this exercise, we have considered two unit cells due to limited computational resources.

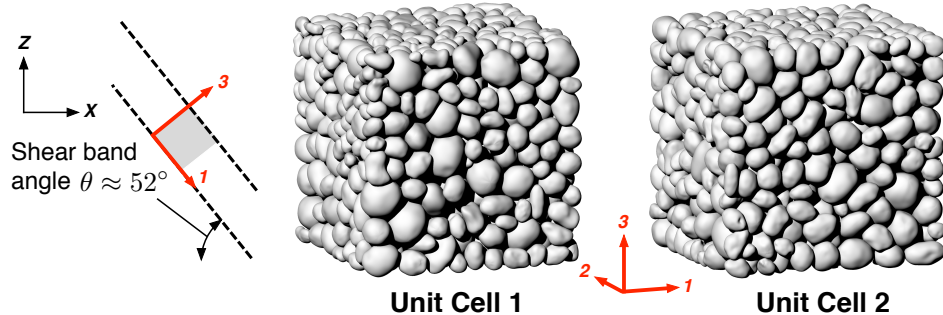


Figure 5.7: Unit cells 1 and 2, generated through the characterization step using 3D XRCT data. The shaded grey region shows cell orientation in local coordinate system with respect to the global coordinate system.

The DIC data indicate that the homogeneous deformation of the shear band region is accompanied by dilation normal to the shear band plane. Therefore, we idealize the loading protocol for the discrete models (in the rotated coordinate system shown in Figure 5.8) as a plane strain shear with a vertical (along the 3-axis) confinement stress. It is known that dilatancy is affected by the confinement stress. For simplicity, however, the vertical stress was calibrated to be a constant. The assumption of a constant vertical stress does not affect the residual strength μ_{cv} since it is determined by particle morphology, and this has already been captured through the characterization process. Movement of grains on the model boundary in the shearing process is prescribed using two rotating smooth side walls, and a feedback loop is used to maintain a constant vertical stress on the top wall. Dynamic relaxation [57] is used where sufficient damping is introduced and the wall movements are

sufficiently slow to remain close to the quasi-static condition. Calibration of the discrete model parameters is performed on one of the cells (Unit Cell 1) while the second cell (Unit Cell 2) serves as a reproducibility check using the same calibrated parameters. The calibrated parameters are normal stiffness $k_n = 3 \times 10^6$, shear stiffness $k_s = 2k_n/3$, interparticle friction coefficient $\mu_p = \tan \phi_p = 0.18$, and vertical stress of 2 units (corresponding to 130 kPa). Due to the explicit time integration used in our NURBS-based DEM, we have made a trade-off between a high normal stiffness (which results in smaller time steps) and a shorter simulation turnaround time.

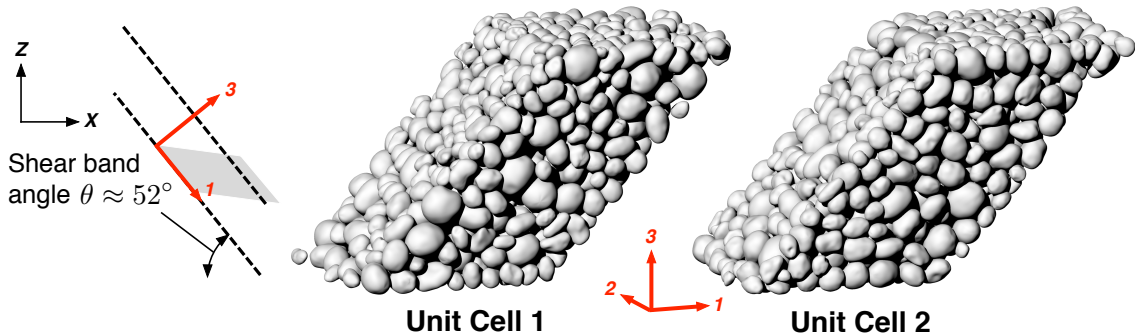


Figure 5.8: Deformed configurations for unit cells 1 and 2. Shaded grey region shows cell orientation in local coordinate system with respect to the global coordinate system: final applied shear angle is 40° from the 3-axis.

From the DIC data, a one-to-one correspondence between the axial global strain and applied shear angle can be established. The shear angle is approximately 40° (from the vertical 3-axis) corresponding to a global axial strain of about 12%. The average dilatancy evolutions calculated from the discrete models are compared with those inferred from DIC and as shown in Figure 5.9, the evolutions from both models match well with experiment. Also plotted in Figure 5.9 are the evolutions of stress ratio q/p , which reach approximately 0.8 at critical state and are close to the calibrated μ_{cv} value of 0.81 in the experimentally-driven multiscale calculation. Assuming that the two unit cells provide an adequate representation of the average dilatancy evolution and residual strength in the shear band, we can use this information and proceed with the same multiscale calculation described in Section 5.3.3. The calculation result (see Figure 5.10) shows that the predicted global structural response that uses discrete information is in excellent agreement with that which uses experimental data (refer to Figure 5.6). The above results point to the importance of and need for accurately capturing grain morphologies in order to improve the predictive capabilities of

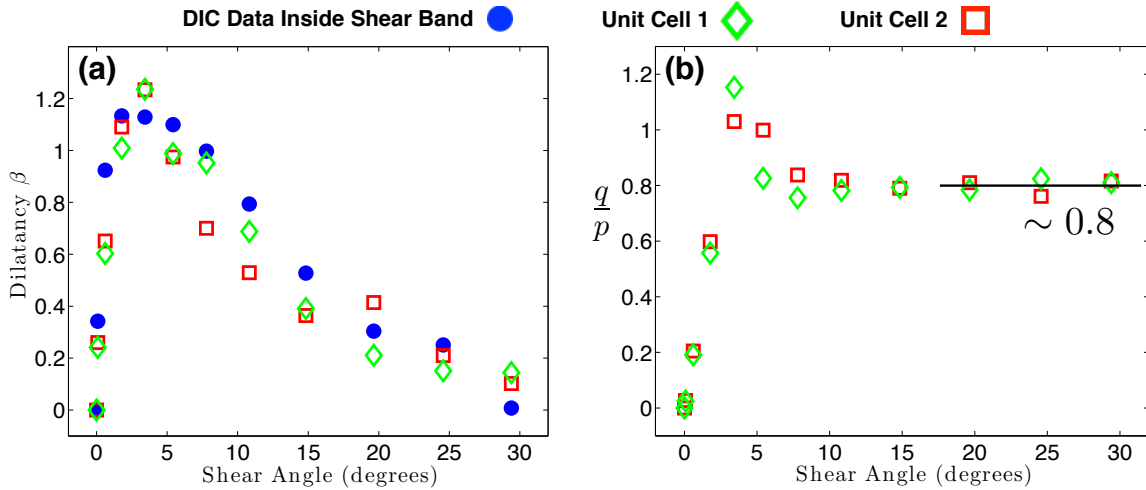


Figure 5.9: Results from discrete computations: evolution of (a) dilatancy and (b) stress ratio.

discrete simulation and multiscale techniques.

5.4 Closure

We have presented a computational mechanics avatar to probe the grain-scale behavior of granular materials. We have discussed the improvements in the characterization and discrete simulation components that have enabled us to transition from faithful representation of grain morphologies in X-ray tomograms of granular media to a morphologically accurate discrete computational model. We then applied and assessed the predictive capabilities of the avatar through a case study on a real experiment. We found good agreement between the microscopic quantities, namely the dilatancy evolution and residual strength, obtained from discrete simulations and those inferred from experiment. To our knowledge, this is the first quantitative comparison of microscopic quantities from discrete simulation and experiment in real sands. In addition, we found excellent agreement between the global continuum response calculated from multiscale computation using the extracted microscopic quantities and that measured in experiment. Overall, we found consistency in results across characterization, discrete analysis, and continuum response from multiscale calculations, providing the first and long sought-after quantitative breakthrough in grain-scale analysis of real granular materials.

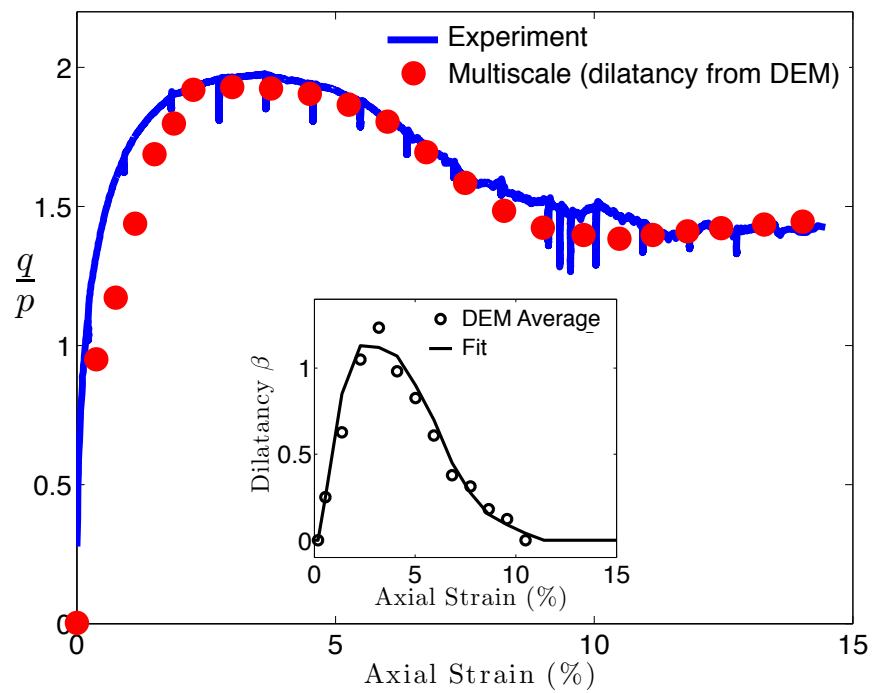


Figure 5.10: Global response from multiscale computation using dilatancy evolution information from discrete models (insert).

Chapter 6

Conclusions and Future Work

6.1 Conclusions

This thesis presented the development of a new discrete element method (DEM) based on Non-Uniform Rational Basis Splines (NURBS). Through NURBS, the new DEM is able to capture sphericity and angularity, the two particle morphological measures used in characterizing real grain geometries.

By taking advantage of the parametric nature of NURBS, the Lipschitzian *dividing rectangle* (DIRECT) global optimization procedure is employed as a solution procedure to the closest-point projection problem, which enables the contact treatment of non-convex particles. Indeed, the implementation ease of the new DEM is largely attributed to the DIRECT algorithm.

A contact dynamics (CD) approach to our NURBS-based discrete method is also formulated. By combining particle shape flexibility, properties of implicit time integration (e.g., larger time steps), and non-penetrating constraints, as well as a reduction to a static formulation in the limit of an infinite time step, we target applications in which the classical DEM either performs poorly or simply fails, i.e., in granular systems composed of rigid or highly stiff angular particles and subjected to quasistatic or dynamic flow conditions. The CD implementation is made simple by adopting a variational framework, which enables the resulting discrete problem to be readily solved using off-the-shelf mathematical programming solvers.

We demonstrated the capabilities of our NURBS-based DEM through 2D numerical examples that highlight the effects of particle morphology on the macroscopic response of granular assemblies under quasistatic and dynamic flow conditions, and a 3D characteriza-

tion of material response in the shear band of a real triaxial specimen. In the latter case, we performed the first quantitative comparison of microscopic quantities from discrete simulation and experiment, and we found excellent agreement between the global continuum response calculated from multiscale computation using the extracted microscopic quantities and that measured from experiment.

6.2 Future Work

Many possible directions can be taken in the future to further the scope of application of our NURBS-based DEM. An immediate step would be the 3D CD implementation, which will enable a robust treatment of quasistatic loading conditions typically encountered in real triaxial experiments. The computational expense in our current implementation prohibits large calculations. Further algorithmic improvements, as well as a parallel computational scheme, are necessary to move forward with larger calculations and obtain more realizations for homogenization. We note that the unit cells considered in the 3D application are only an idealization of the actual system in terms of the boundary conditions, and we have made simplifying modeling assumptions to make the simulations tractable. The ability to perform a full specimen-level calculation would remedy this and provide us with quantities such as the complete stress state inside the shear band, which is currently inaccessible by experiment. A full specimen-level calculation will also allow one to look into the effects of specimen heterogeneity on the conditions for the development and propagation of shear bands, a study that is incomplete with only unit cell calculations. Finally, an improved computational scheme would allow us to study specimens composed of more angular grain geometries (e.g., Hostun sand).

From the 3D application described in the previous chapter, it is clear that our NURBS-based DEM has a great potential for complementing experimental problems related to the characterization of granular micromechanical properties. Currently, we have used data from only one triaxial experiment, which is severely limited. To make the characterization process more comprehensive, more experiments should be performed to probe how specific microscopic quantities or plastic internal variables may respond under different conditions (e.g., confinement pressure), and these would provide further validation cases for our method. Physical grain-scale experiments such as compression tests for contact response and scratch

tests for interparticle friction can also be carried out. In general, both macro- and grain-scale experiments would serve to provide tighter bounds or constraints on the discrete model parameters.

We close this thesis by asking the following (hard) questions concerning the representation of particle geometry for grain-scale analysis, in which the answers are currently unclear and may become important when more angular geometries are considered:

1. How much geometric resolution does one need for grain-scale DEM to be accurate?
2. How sensitive is the macroscopic response to the level of geometric resolution?
3. Is there a scale separation between roundness and surface roughness? If not, how does one decide the spatial resolution cutoff below which the asperities are accounted for by interparticle friction.

Here, ideas from signal processing and statistical methods may provide quantitative means to start addressing these questions.

Doesn't talk about drawback actually

Appendix A

Verification Tests

A.1 Classic DEM Tests

The example described here is the classic nine-disk test performed in [24], which serves as a verification of the explicit time integration algorithm for the 2D case described in Section 2.1. A simple NURBS intersection-based contact approach is utilized so that the particle overlap is identical with that calculated using equation (2.5). An assembly of nine (9) disks is packed in simple cubic configuration within rigid walls, as shown in Figure A.1. All nine disks are identical, with radius of 50 units and density of 1000 units. Two different contact stiffnesses are used in these calculations: $k_n = 1.35e9$ and $k_n = 1.5e8$, with the shear contact stiffness taken as $k_s = k_n$, unless otherwise noted. Also, the interparticle friction coefficient $\mu = \tan \phi$, where ϕ is the internal friction angle. In this test, $\phi = 15^\circ$, unless otherwise noted. The nine-disk test is subdivided into two loading scenarios: uniform compression and pure distortion.

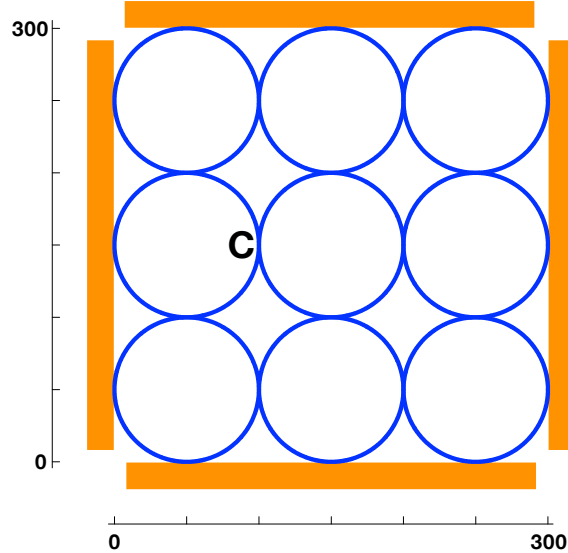


Figure A.1: Initial configuration for nine-disk test.

A.1.1 Uniform compression test

In this test, all four walls are moved inwards with speed v_{wall} for a total duration T_{wall} . Wall motion is then stopped at that point T_{wall} and the test is allowed to continue until a total of 200 cycles is reached. The loading sequences in this test are summarized in Table A.1.

Table A.1: Loading cases for uniform compression test

Case	No.	Disk Stiffness $k_n = k_s$	Δt	T_{wall} (cycles)	v_{wall}
(a)	1	1.35e9	0.01525	40	0.12
	2			120	0.04
(b)	1	1.5e8	0.04576	40	0.36
	2			120	0.12

In this test, the effect of global numerical damping ξ , as it appears on the global equations of motion (see Section 2.1.3), is investigated. Figure A.2 shows the evolution of normal force at point C for case (a) number 1 (see Table A.1). Normal force evolution is reported for the case when there is global numerical damping ($\xi = 3$) and for the case when there is no global damping ($\xi = 0$). No contact damping β is used on any of the results reported herein. The results shown in Figure A.2 exactly match those reported in [24] and clearly show the effect of damping in reducing the amplitude of oscillations, allowing kinematics and corresponding forces to reach steady-state equilibrium. Finally, the evolution of the normal force F_n at point C is shown in Figure A.3. It can be seen from this figure that

all loading cases converge to roughly the same value of force after a number of cycles when steady equilibrium is achieved.

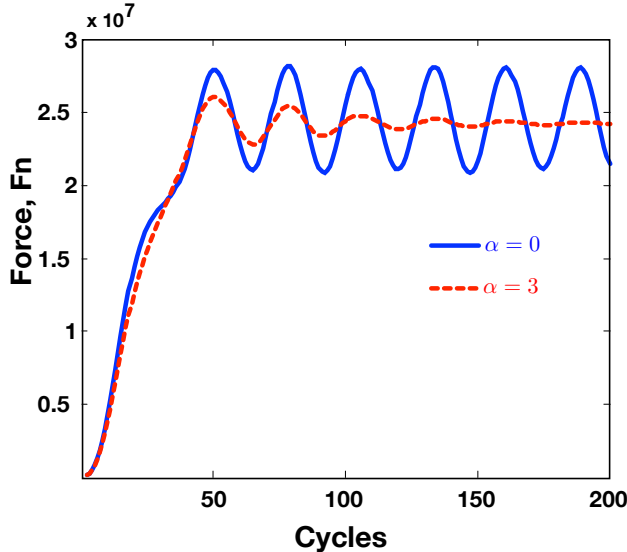


Figure A.2: Normal force F_n evolution at C for loading case (a) No. 1 at different values of global numerical damping.

A.1.2 Distortion test

Here, we reproduce the distortion test for the nine-disk configuration reported in [24]. This constitutes the second half of the verification process and it is performed following the loading sequence reported in [134], which thoroughly describes the distortion test shown in the original work of Cundall and Strack [24]. Similar characteristics, as in Case (a) No. 1 shown in Table A.1, are used here, with $k_n = 1.35e9$ and $\Delta t = 0.01525$. The sample is initially uniformly compressed, as in the uniform compression test, for 4000 cycles with wall speed $v_{wall} = 0.12$, as before. Wall motion is then stopped, followed by 1000 cycles where oscillations are allowed to settle via global numerical damping $\xi = 3.0$. As before, no contact damping was used (i.e., $\beta = 0$). After this uniform and settlement stage (total of 5000 cycles), constant volume distortion is prescribed by rotating the side walls at a constant angular velocity of 0.0175 for 500 cycles. The deformed configuration of the assembly after the first 5000 cycles of uniform compression and settlement, and the subsequent 500 cycles of constant-volume distortion are shown in Figure A.4.

The evolution of the normal force F_n and shear force F_s is shown in Figure A.5. Curves

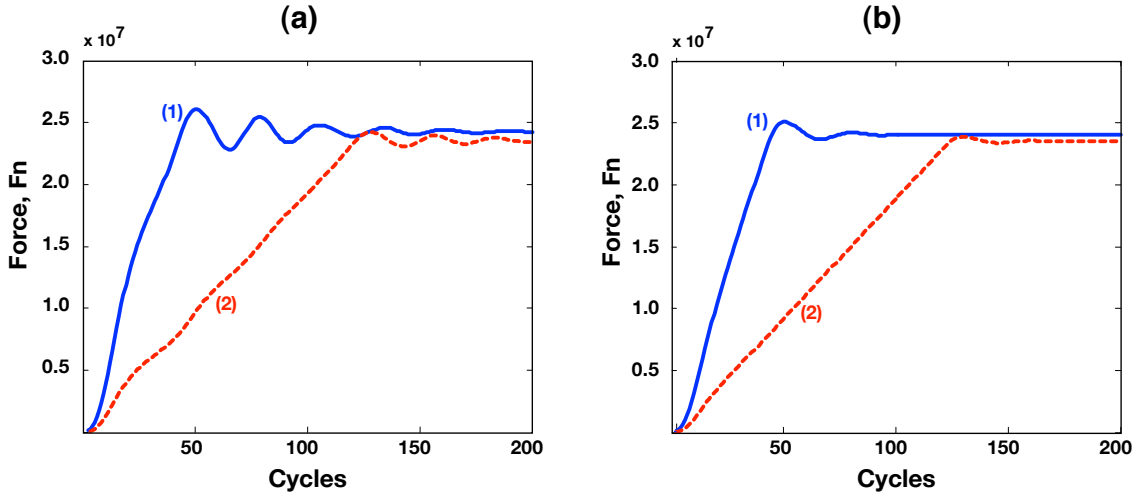


Figure A.3: Evolution of normal force F_n for all loading cases reported in Table A.1 with global numerical damping $\xi = 3$.

are shown for different values of interparticle friction coefficient $\mu = \tan \phi$ at various ratios of normal to shear contact stiffness k_s/k_n . The ratio k_s/k_n was shown by Mindlin [113] to vary from $2/3$ to 1 for the case of linear elastic bodies in contact with elliptical contact areas. The extreme values of this range were investigated in [24] and are also reported here in Figure A.5. The evolutions shown in Figure A.5 agree quantitatively with the results obtained in [24; 134] and show the importance of interparticle friction (particle roughness) and the role of contact stiffness as modeled by the ratio k_s/k_n .

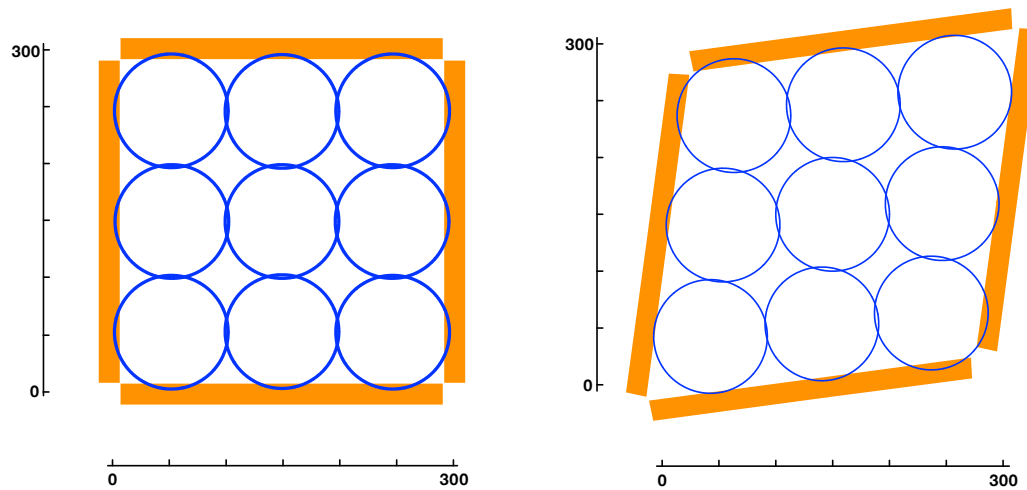


Figure A.4: Distorted configurations for nine-disk assembly after 5000 cycles of uniform compression and settlement, and after a subsequent 500 cycles of constant volume (shear) distortion. Results shown correspond to case when $k_n = k_s$ and interparticle friction angle $\phi = 30^\circ$.

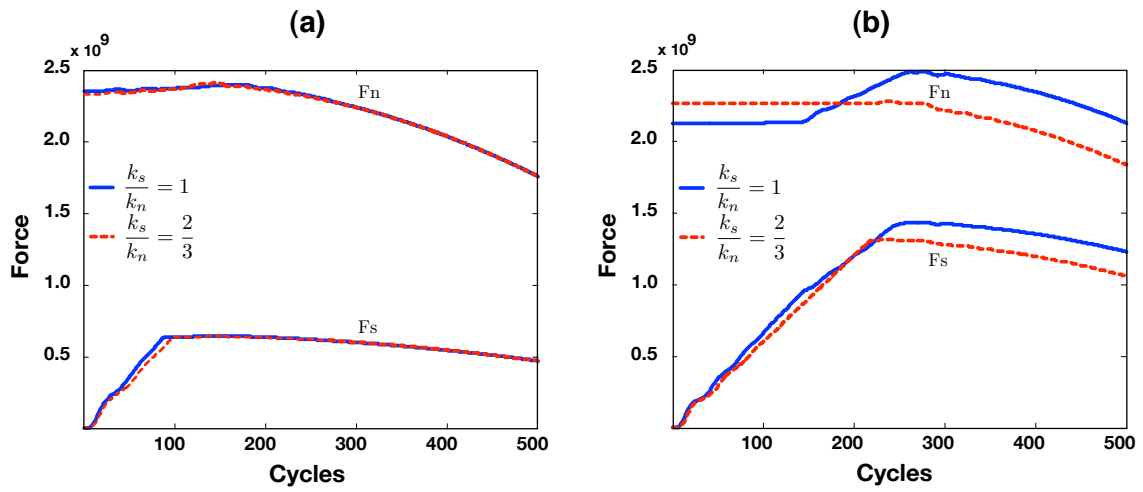


Figure A.5: Normal and shear force evolution at point C in nine-disk assembly during 500 cycle shear distortion at various k_s/k_n ratios. (a) Interparticle friction angle $\phi = 15^\circ$. (b) Interparticle friction angle $\phi = 30^\circ$.

A.2 Contact Dynamics Binary Collision Tests

We check the conservation of energy and momentum under elastic and plastic binary collisions. The left disk (Disk 1) is given an initial velocity of $v_x = 1$ moving towards the right disk (Disk 2), which is stationary. The properties for this problem are mass $m = \pi$, time step $\Delta t = 0.01$, and time stepping parameter $\theta = 0.5$ for elastic collision and $\theta = 1$ for plastic collision.

For elastic collision, the results are shown in Figures A.6 through A.9. We see that both energy and momentum are conserved. After collision, Disk 1 becomes stationary and Disk 2 takes on the velocity $v_x = 1$. For plastic collision, the results are shown in Figures A.10 through A.13. In this case, momentum is conserved, but energy is not. After collision, the Disk 1 and Disk 2 move together at $v_x = 0.5$. These results show that both momentum and energy behave correctly under binary collision.

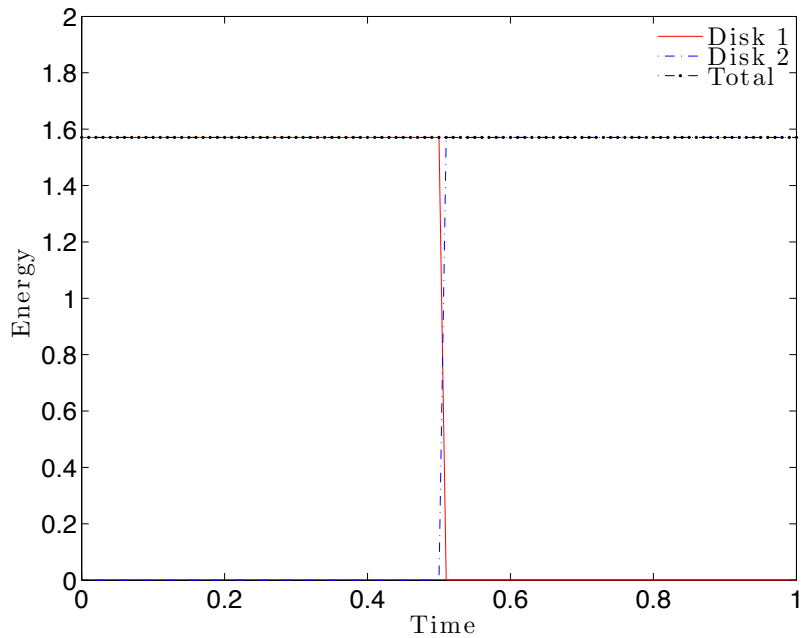


Figure A.6: Elastic collision: energy history.

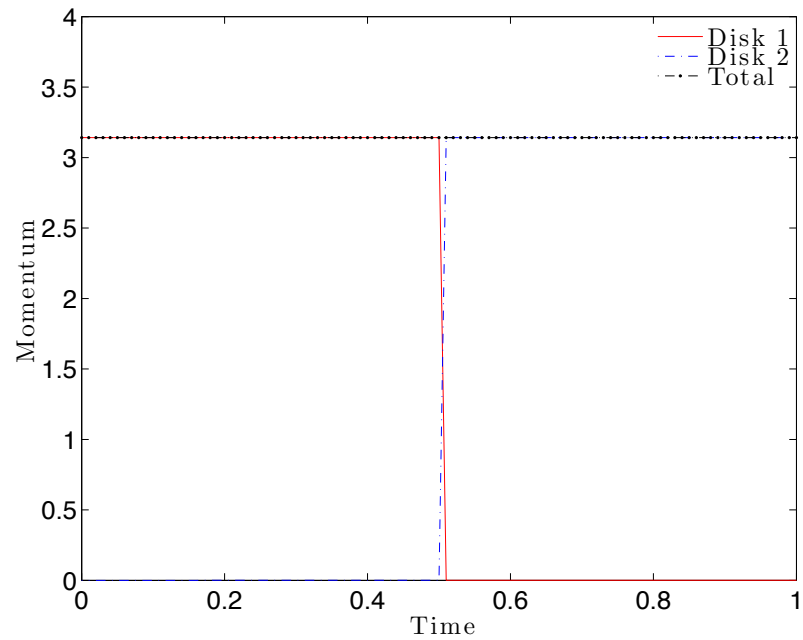
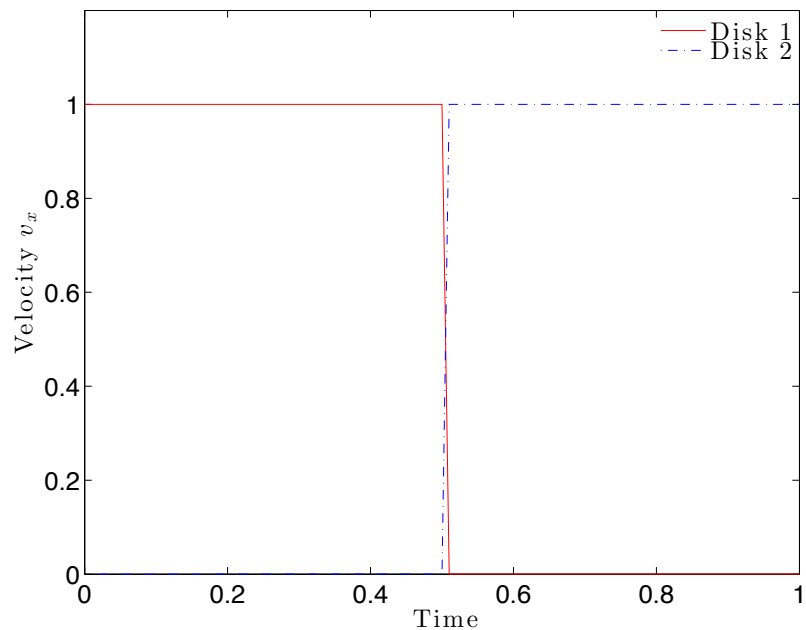


Figure A.7: Elastic collision: momentum history.

Figure A.8: Elastic collision: velocity v_x history.

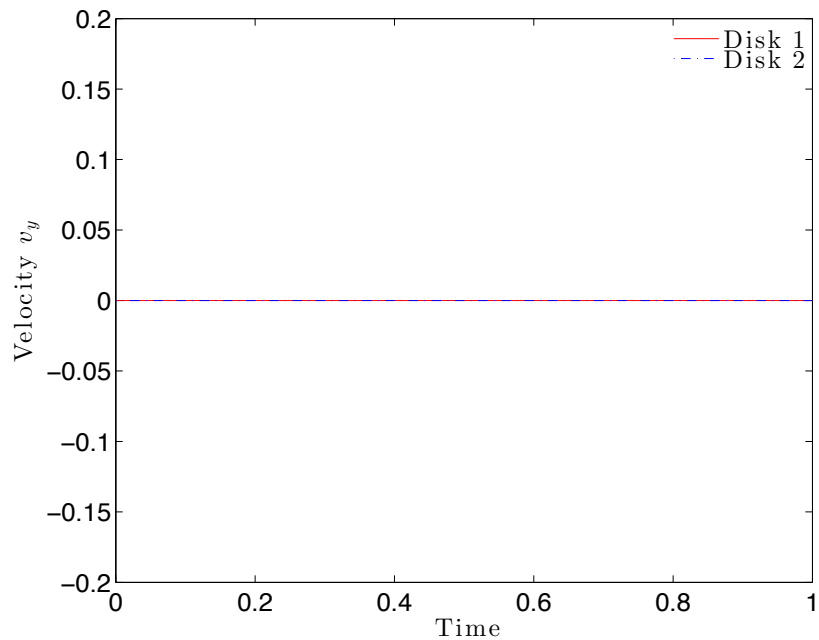


Figure A.9: Elastic collision: velocity v_y history.

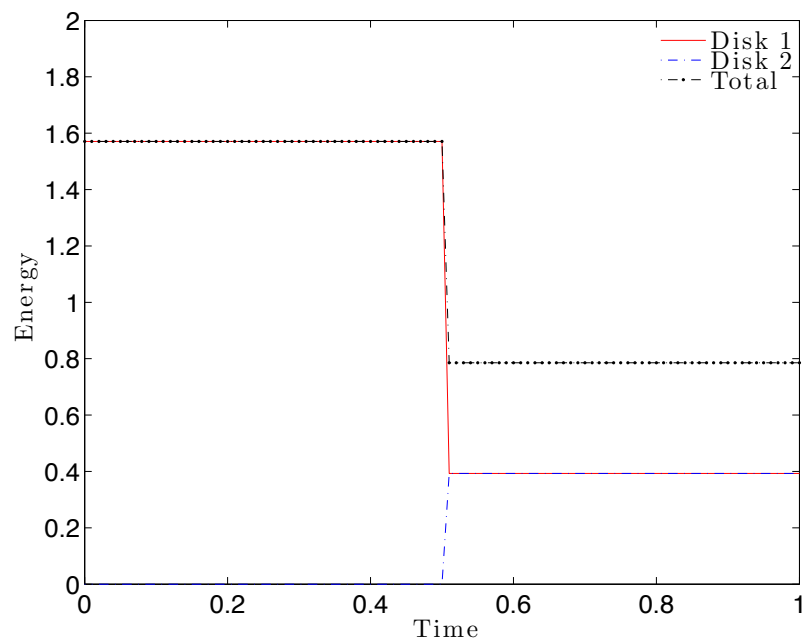


Figure A.10: Plastic collision: energy history.

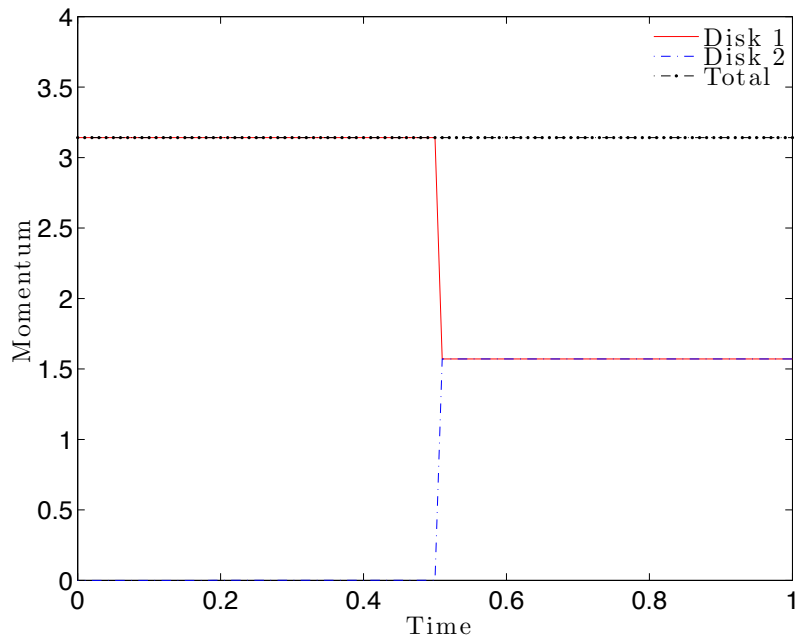
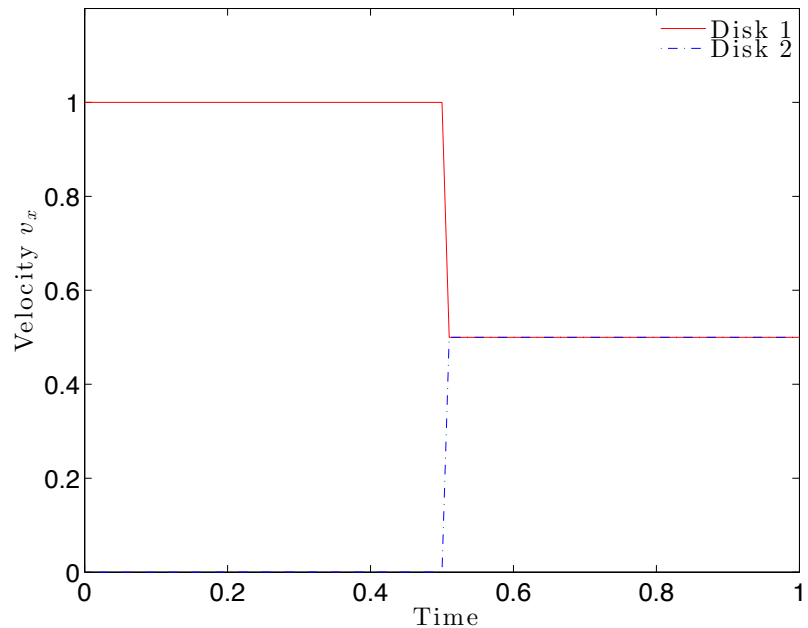


Figure A.11: Plastic collision: momentum history.

Figure A.12: Plastic collision: velocity v_x history.

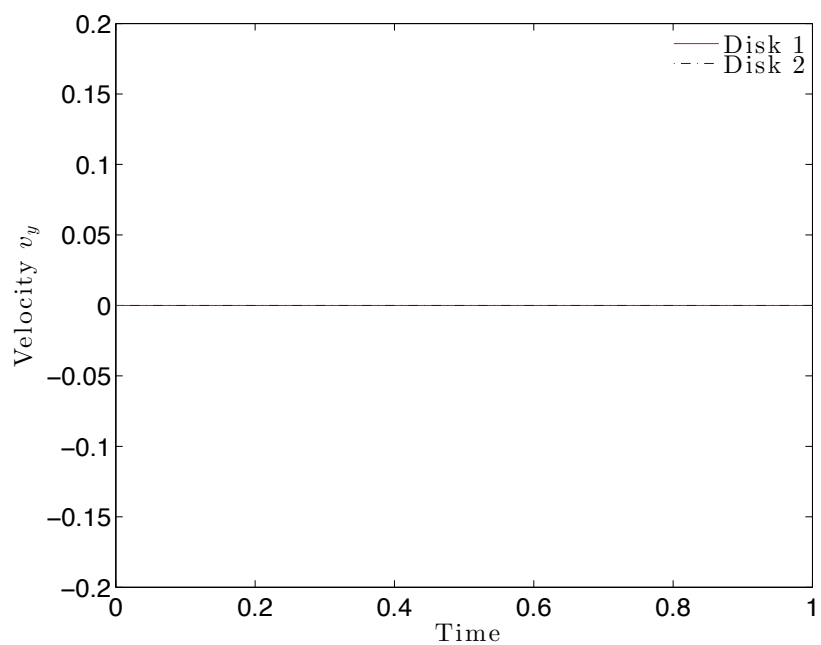


Figure A.13: Plastic collision: velocity v_y history.

A.3 Kinematics with Associated Sliding Rule

In Chapter 4, we presented a CD formulation with an associated sliding rule that introduces a ‘dilation layer’ between two sliding bodies. Here, we discuss the applicability of this sliding rule. We first discuss the resulting kinematics followed by numerical tests to show that the effects of this rule are very minor, and the slight error made is deemed to be a small price to pay for maintaining a standard convex variational problem. In following the discussion below, the reader should bear in mind the applications in which the associated sliding rule is used, i.e., dense granular media composed of many particles that are being constantly rearranged either with confinement under quasistatic conditions or under dynamic flow conditions. We note that a similar sliding rule, which also introduces a dilation effect, was used by Tasora and Anitescu in their CD formulation [135–139].

A.3.1 Quasistatic case

The presentation here is based on [99]. For clarity, we have excluded rotations and contact elasticity. With this, equation (4.8) reduces to:

$$\begin{aligned} \min_{\Delta\boldsymbol{x}, \Delta\boldsymbol{\alpha}} \max_{\boldsymbol{p}, \boldsymbol{q}} & \left\{ \frac{1}{2} \Delta\boldsymbol{x}^T \bar{\boldsymbol{M}} \Delta\boldsymbol{x} - \Delta\boldsymbol{x}^T \bar{\boldsymbol{f}}_0 \right\} \\ & + \left\{ \Delta\boldsymbol{x}^T (\boldsymbol{N}_0 \boldsymbol{p} + \widehat{\boldsymbol{N}}_0 \boldsymbol{q}) - \boldsymbol{g}_0^T \boldsymbol{p} \right\} \end{aligned} \quad (\text{A.1})$$

subject to $\|\boldsymbol{q}\| - \mu\boldsymbol{p} \leq \mathbf{0}, \quad \boldsymbol{p} \geq \mathbf{0}$

The kinematics associated with equation (A.1) are recovered by solving the max part of the problem which leads to the following set of optimality conditions:

$$\begin{aligned} \Delta\boldsymbol{u}_N &= \boldsymbol{N}_0^T \Delta\boldsymbol{x} = -\mu\boldsymbol{\lambda} + \boldsymbol{g}_0 \\ \Delta\boldsymbol{u}_T &= \widehat{\boldsymbol{N}}_0 \Delta\boldsymbol{x} = \text{sgn}(\boldsymbol{q})\boldsymbol{\lambda} \end{aligned} \quad (\text{A.2})$$

where subscripts N and T denote the normal and tangential directions, respectively, and $\boldsymbol{\lambda}$ are Lagrange multipliers such that $\lambda^I(|q^I| - \mu p^I) = 0, I \in C$, where C is the set of potential contacts. The important point regarding the above kinematic equations is that the gap g_0 in time discrete processes tends to cancel the dilation and in such a way that is entirely eliminated in the limit of the time step tending to zero. This can be illustrated by the simple example shown in Figure A.14. We here consider a single particle on a rigid

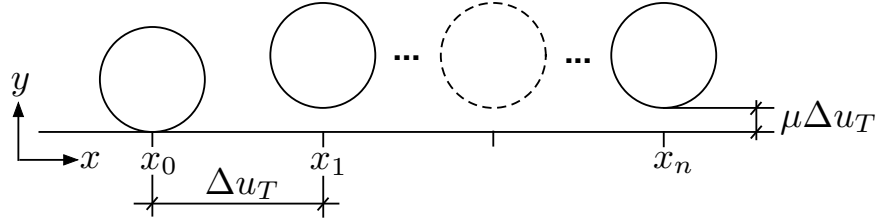


Figure A.14: Quasistatic sliding along a rigid frictional surface.

frictional surface. The particle is initially at rest on the surface at $(x_0, y_0) = (x_0, 0)$. As such, the gap between the particle and the surface is $g_0 = 0$. A series of tangential displacements $\Delta u_T = \Delta u_x$ of equal size are then imposed in a quasistatic manner. With the application of the first increment, the normal displacement is $-\Delta u_{N,1} = \Delta u_{y,1} = \mu\Delta u_{x,T}$ which brings the particle to position $(x_1, y_1) = (x_0 + \Delta u_T, \mu\Delta u_T)$. To continue the time stepping, the new gap is calculated as $g_1 = \mu\Delta u_T$. From equation (A.2), the new normal displacement then follows as $\Delta u_{N,2} = g_1 - \mu\Delta u_T = 0$. In other words, no further dilation occurs and the particle slides parallel to the surface at a distance $\mu\Delta u_T$ above it such that an artificial dilation layer — which can be made arbitrarily thin — separates the particle from the surface. Despite this physical separation, contact forces still exist and the behavior of the particle is in every way equal to what it would be with a gap identically equal to zero.

A.3.2 Dynamic case

To study the more general dynamic case, we consider a particle as shown in Figure A.15. The particle is initially at a distance g_0 from the rigid frictional surface located at $y = 0$

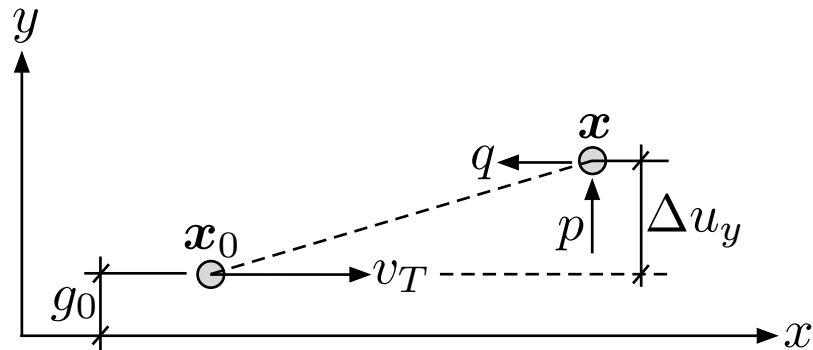


Figure A.15: Dynamic sliding along a rigid frictional surface.

and has an initial horizontal velocity v_T . It is assumed that the particle is within the zone of contact, i.e., within the dilation layer introduced above. This will possibly bring about a further dilation such that the gap increases or the particle may slide along the initial dilation layer as in the quasistatic case. The time discrete governing equations (for $\theta = 1$) are given by (see Section 4.2.3)

$$\begin{aligned} m\Delta u_x &= -q\Delta t^2 + mv_T\Delta t \\ m\Delta u_y &= p\Delta t^2 \\ q &= \mu p \\ \Delta u_x &= \lambda \\ \Delta u_y &= \mu\lambda - g_0 \end{aligned} \tag{A.3}$$

From these equations, the vertical displacement is found to be

$$\Delta u_y = \frac{\mu v_T \Delta t - g_0}{1 + \mu^2} \tag{A.4}$$

Equating the numerator to zero leads us to define a critical time step:

$$\Delta t_{\text{cr}} = \frac{g_0}{\mu v_T} \tag{A.5}$$

such that the initial gap will not grow any further for $\Delta t \leq \Delta t_{\text{cr}}$ while it will increase for $\Delta t > \Delta t_{\text{cr}}$. In other words, for a finite initial gap, a time step can always be chosen to produce a non-dilative response. This property breaks down for an initial gap identically equal to zero. In this case, the response will be dilative, regardless of the time step. In practice, however, the effects of this possible dilation are in most cases very limited as will be shown in Section A.3.4.

A.3.3 The case with rotations included

From equation (4.14), the kinematic relations with rotations included (but without contact elasticity) are:

$$\begin{aligned} \Delta \mathbf{u}_N &= \mathbf{N}_0^T \Delta \mathbf{x} = \mathbf{g}_0 - \mu \boldsymbol{\lambda} \\ \Delta \mathbf{u}_T &= \widehat{\mathbf{N}}_0^T \Delta \mathbf{x} = \text{sgn}(\mathbf{q}) \boldsymbol{\lambda} + (\mathbf{R}_0^{qT} + \mathbf{R}_0^{pT}) \Delta \boldsymbol{\alpha} \end{aligned} \tag{A.6}$$

In this case, the inclusion of rotations further limits dilation in the sense that tangential motion can be accommodated not only by sliding ($\lambda > 0$), but also by rolling ($|\Delta\alpha| > 0$). This lends further credence to the approach of using an associated sliding rule. Indeed, in the quasistatic deformation of granular materials, such as in triaxial tests, it has long been recognized that sliding occurs only at a small fraction of the contacts [82].

A.3.4 A numerical test

To see the consequence of the associated sliding rule, and show that its effects are very minor for the types of granular media applications mentioned above, consider the problem of a block on an incline as shown in Figure A.16. We solve this problem using the CD formulation described in Chapter 4, without contact elasticity in which the effects of the associated sliding rule are most prominent. The properties for this problem are incline angle $\theta_s = 20^\circ$, block mass $m = 7.854$, and acceleration of gravity $g = 10$. The critical friction coefficient is $\mu_{\text{crit}} = \tan \theta_s = 0.364$. The friction coefficient between the block and incline is

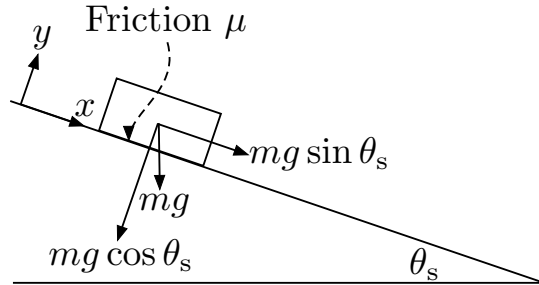


Figure A.16: Block on an incline.

denoted by μ . We consider two cases:

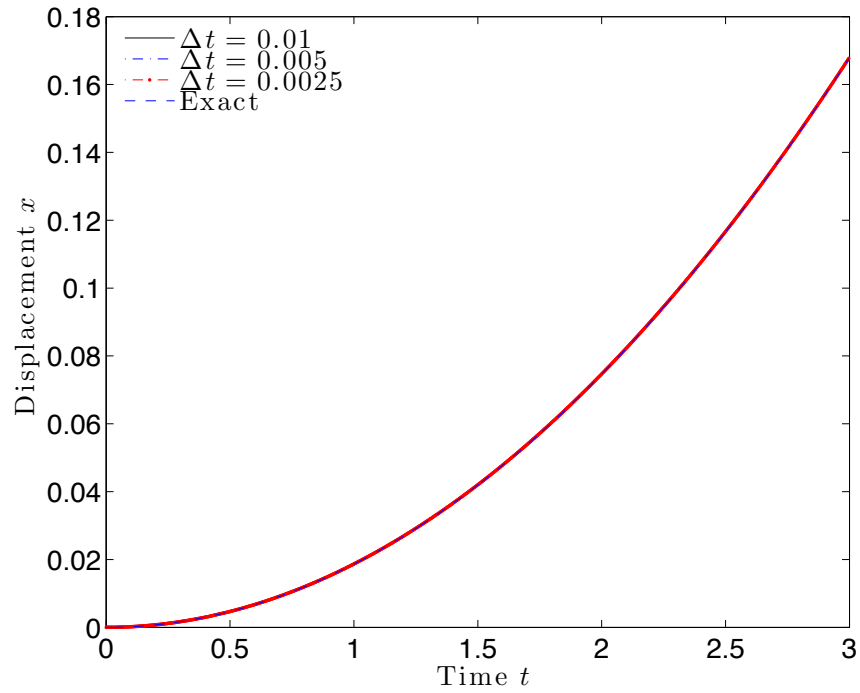
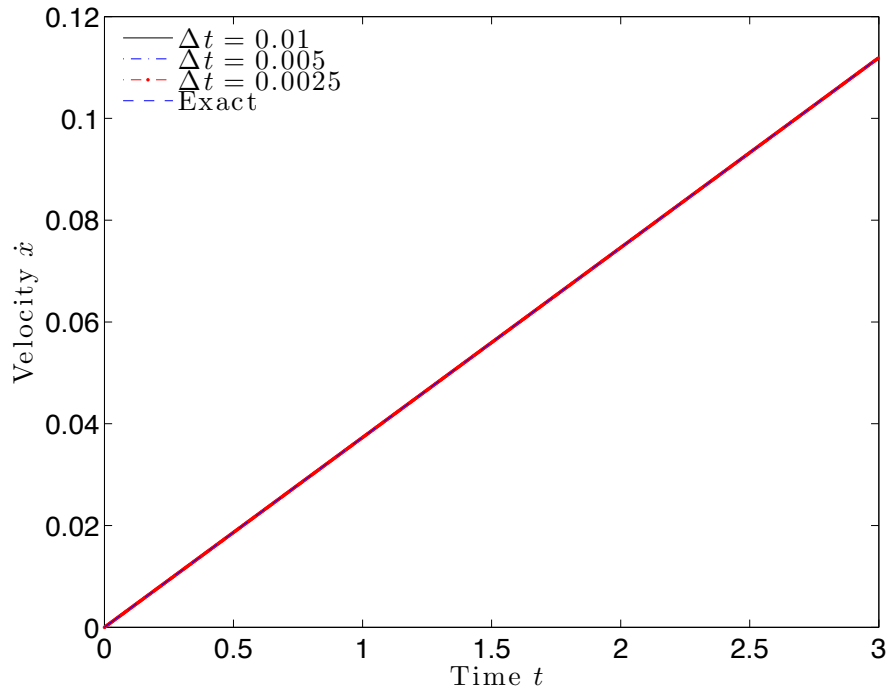
1. $\mu = 0.36 < \mu_{\text{crit}}$, which means that the block should slide down
2. $\mu = 0.4 > \mu_{\text{crit}}$, which means that the block should remain stationary

For the block starting from rest, the exact solution is:

$$x(t) = \begin{cases} 0 & : \mu > \mu_{\text{crit}} \\ 0.5(\sin \theta_s - \mu \cos \theta_s)gt^2 & : \mu < \mu_{\text{crit}} \end{cases} \quad (\text{A.7})$$

$$\dot{x}(t) = \begin{cases} 0 & : \mu > \mu_{\text{crit}} \\ (\sin \theta_s - \mu \cos \theta_s)gt & : \mu < \mu_{\text{crit}} \end{cases}$$

The time stepping parameter is set at $\theta = 1$ and we consider three time steps $\Delta t = 0.01, 0.005$ and 0.0025 . We observe that for Case 1 (see Figures A.17 through A.21), the sliding block is accompanied by a negligible dilation that grows at a very small rate as shown in Figure A.19, and this dilation decreases as the time step gets smaller. These observations are consistent with the kinematic analysis for the dynamic case with zero initial gap described in the previous section. The dilatation did not affect the calculated contact normal and shear forces, which match mg and μmg , respectively. Again, we emphasize that in the aforementioned granular applications, a sliding particle would typically move for a very short distance before kinematically affected by its neighboring particles in the next time step, and the associated dilation within a time step would be a negligible fraction of the particle size. For Case 2 (see Figures A.22 through A.26), the block remained stationary as expected.

Figure A.17: Displacement along x ($\mu = 0.36$).Figure A.18: Velocity along x ($\mu = 0.36$).

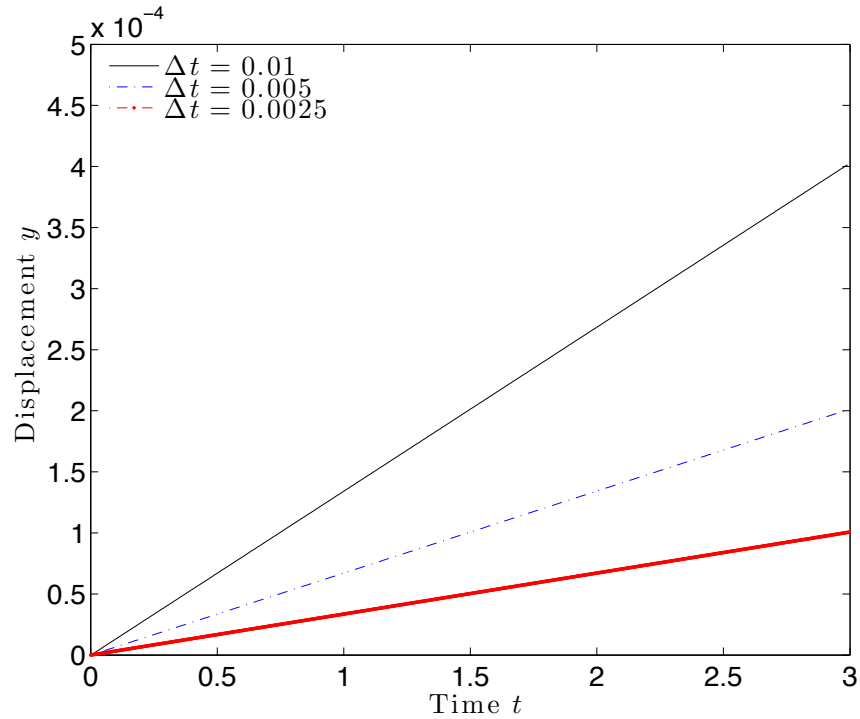


Figure A.19: Displacement normal to plane or gap ($\mu = 0.36$).

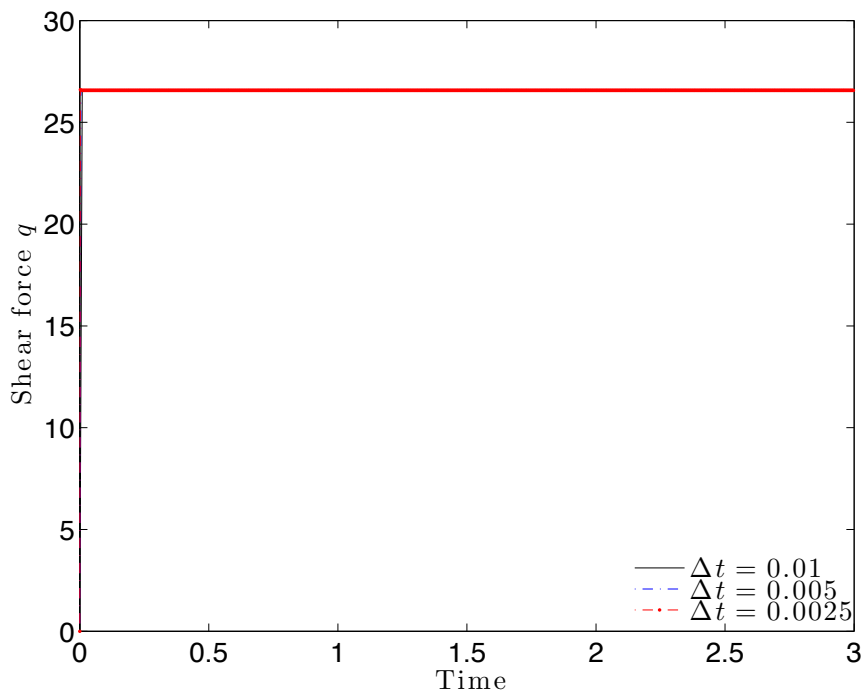
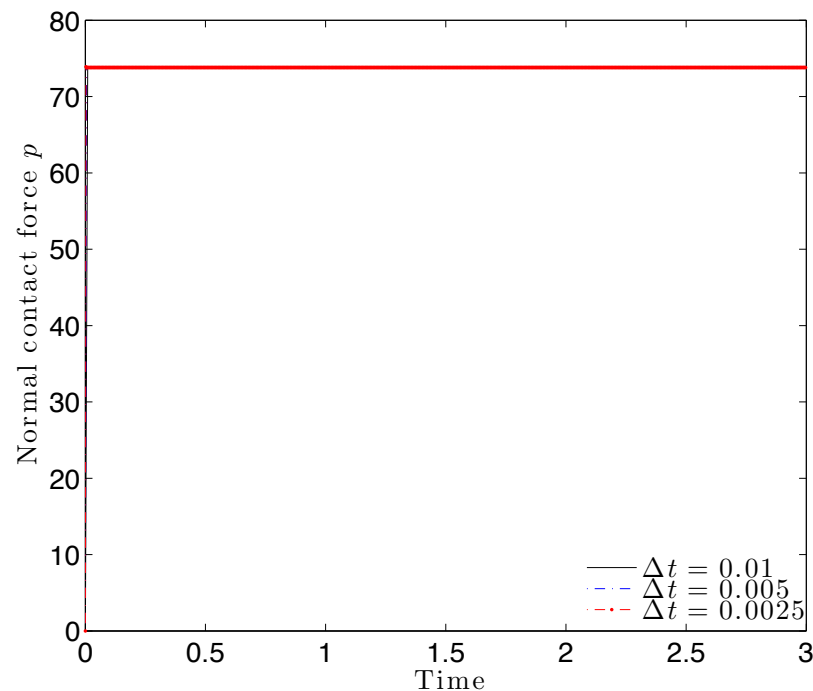
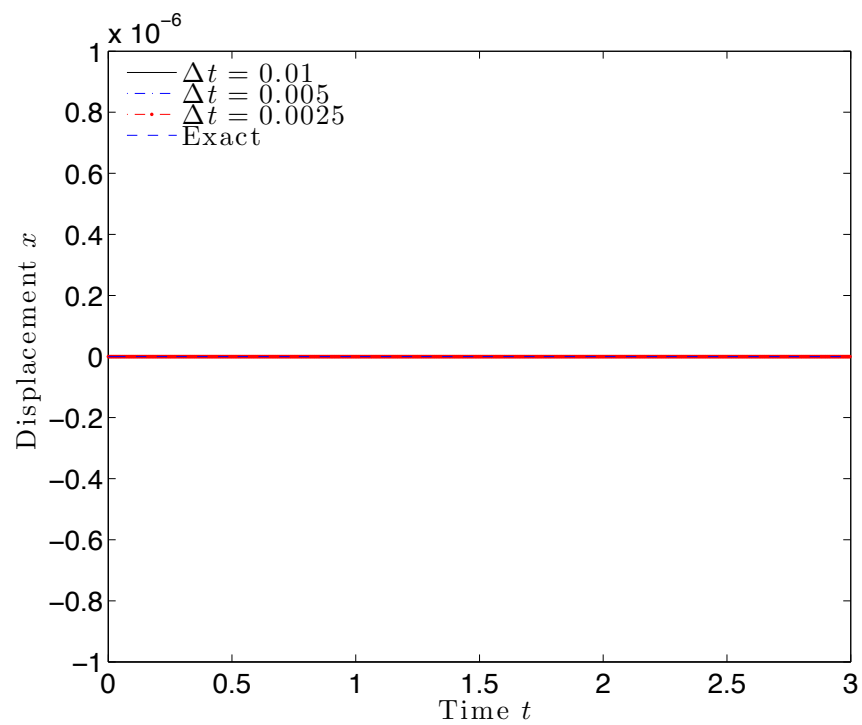
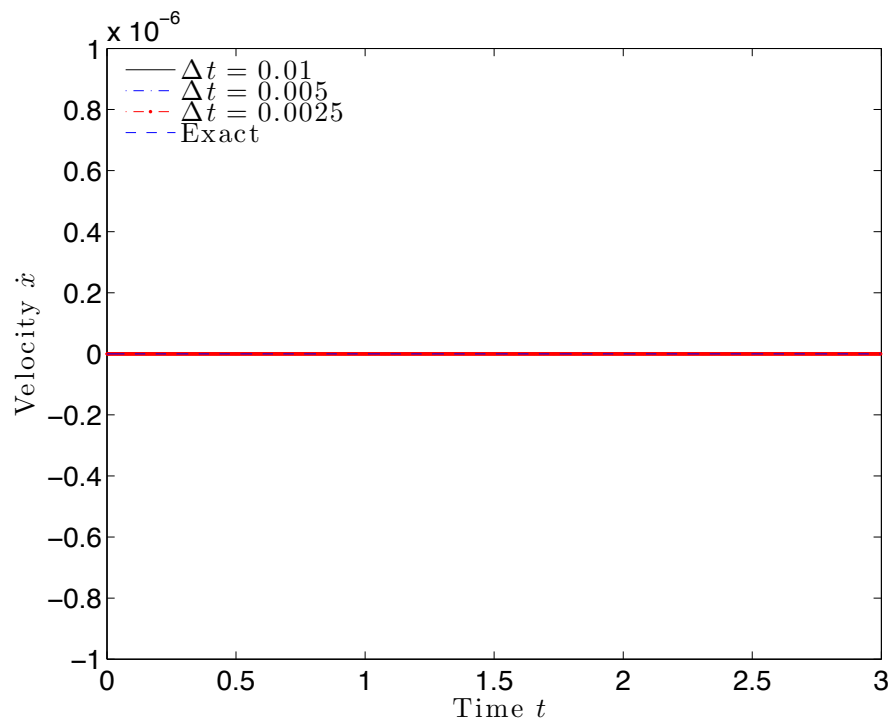
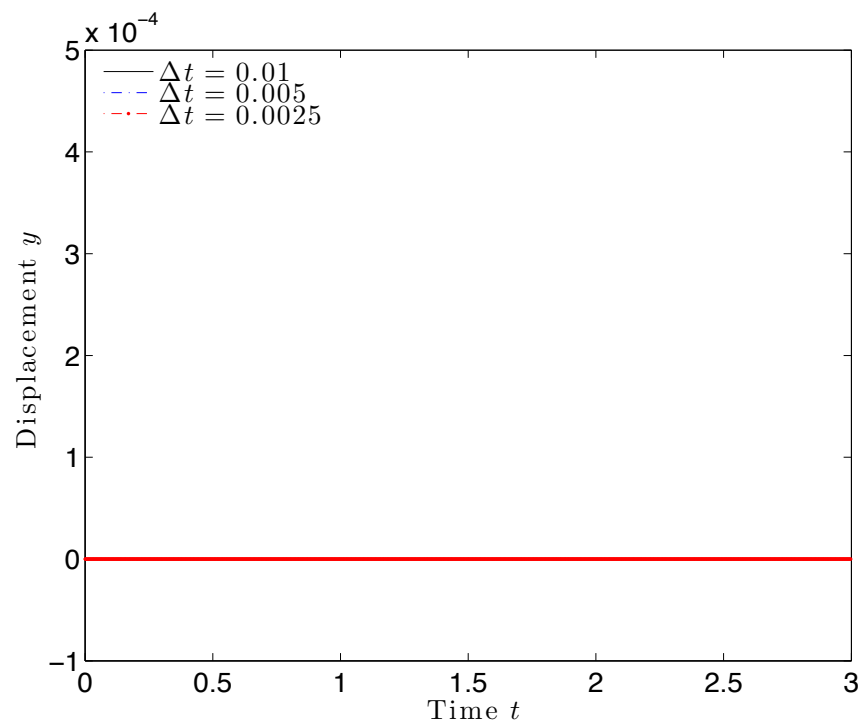
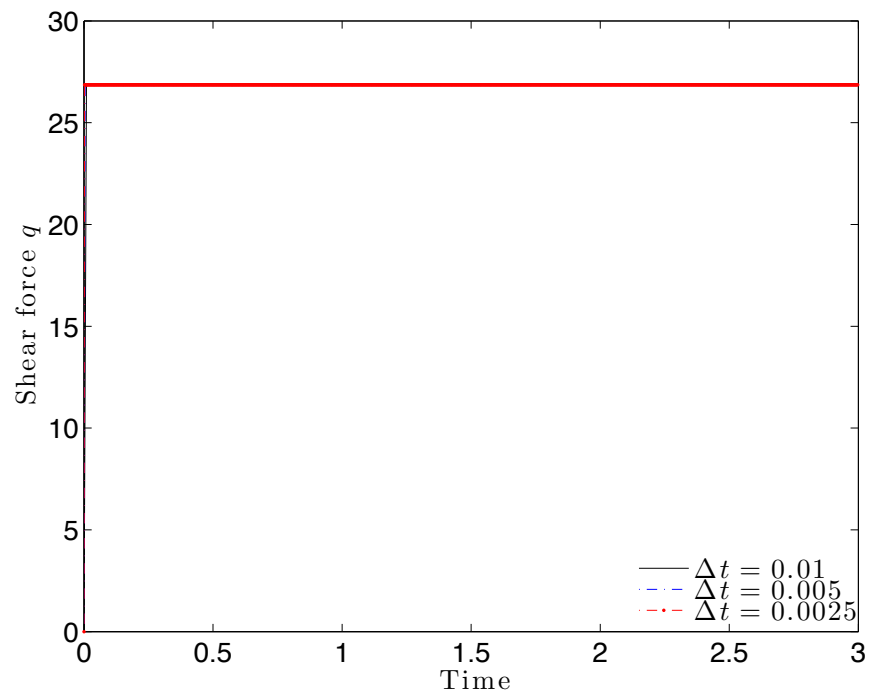
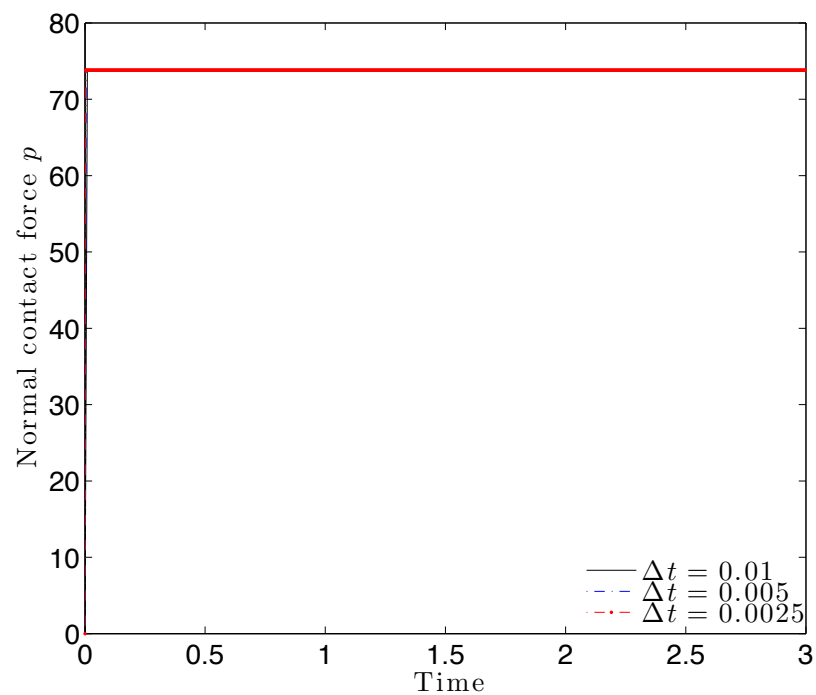


Figure A.20: Shear force ($\mu = 0.36$).

Figure A.21: Normal contact force ($\mu = 0.36$).Figure A.22: Displacement along x ($\mu = 0.4$).

Figure A.23: Velocity along x ($\mu = 0.4$).Figure A.24: Displacement normal to plane or gap ($\mu = 0.4$).

Figure A.25: Shear force ($\mu = 0.4$).Figure A.26: Normal contact force ($\mu = 0.4$).

Appendix B

Three-Dimensional Contact Dynamics Formulation

The two-dimensional formulation discussed in Chapter 4 may be extended to three dimensions in a number of ways. All appropriate physical constraints of the three-dimensional contact problem can be found in [99] and hence, will not be repeated here. The exception is that the integration of rotational degrees of freedom needs special attention.

Kinematically, the non-trivial difference between the two- and three-dimensional case is a result of rotations of arbitrary-shaped particles. In the following, we outline one possible approach to integrate the rotational degrees of freedom in three dimensions. Without loss of generality, we consider the dynamic problem without contact elasticity. Unless otherwise noted, all quantities pertain to a single particle in the principal body frame.

The discretization of rotational equilibrium equations using the θ -method gives

$$\boldsymbol{I} \frac{\boldsymbol{\omega} - \boldsymbol{\omega}_0}{\Delta t} + \text{skew}[\boldsymbol{\omega}] \boldsymbol{I} \boldsymbol{\omega} = \boldsymbol{m}_0 \quad (\text{B.1})$$

with the update equation for the (body frame) rotational degrees of freedom as (analogous to equation (4.6)b):

$$\boldsymbol{\omega} = \frac{1}{\theta} \left[\frac{\boldsymbol{\alpha} - \boldsymbol{\alpha}_0}{\Delta t} - (1 - \theta)\boldsymbol{\omega}_0 \right] \quad (\text{B.2})$$

and where \boldsymbol{I} is the time-independent tensor of (principal) inertia in the body frame, \boldsymbol{m}_0 are the external moments in the body frame, and $\text{skew}[\boldsymbol{\omega}]$ is the skew-symmetric matrix defined by $\text{skew}[\boldsymbol{\omega}] \boldsymbol{\omega} = 0$. We observe that the rotational equilibrium equations are nonlinear due to the presence of the products of angular velocities. This nonlinearity can be accounted

for within the mathematical programming framework proposed in this paper as follows. We first define the (nonlinear) residual equations as

$$\mathbf{r}(\boldsymbol{\omega}) = \mathbf{m}_0 - \mathbf{I} \frac{\boldsymbol{\omega} - \boldsymbol{\omega}_0}{\Delta t} - \text{skew}[\boldsymbol{\omega}] \mathbf{I} \boldsymbol{\omega} \quad (\text{B.3})$$

A truncated Taylor expansion about the k -th iterate $\boldsymbol{\omega}_k$ then gives the following iterative procedure for the (unconstrained) solution of $\boldsymbol{\omega}$

$$\begin{aligned} \mathbf{J}|_{\boldsymbol{\omega}_k} \delta \boldsymbol{\omega} &= \mathbf{r}(\boldsymbol{\omega}_k) \\ \boldsymbol{\omega}^{k+1} &= \boldsymbol{\omega}^k + \delta \boldsymbol{\omega}, \quad \boldsymbol{\omega}^{k=0} = \boldsymbol{\omega}_0 \end{aligned} \quad (\text{B.4})$$

where $\mathbf{J} = -\frac{\partial \mathbf{r}}{\partial \boldsymbol{\omega}}$. To cast this iterative procedure along with all the physical constraints of the problem as a quadratic programming problem, we note from equation (B.2) that the variation of $\boldsymbol{\omega}$ is simply (since $\boldsymbol{\omega}_0$ and $\boldsymbol{\alpha}_0$ are fixed)

$$\delta \boldsymbol{\omega} = \frac{\delta \boldsymbol{\alpha}}{\theta \Delta t} \quad (\text{B.5})$$

which allows us to rewrite the iterative procedure in equation (B.4) as

$$\begin{aligned} \bar{\mathbf{J}}|_{\boldsymbol{\omega}_k} \delta \boldsymbol{\alpha} &= \mathbf{r}(\boldsymbol{\omega}_k) \\ \boldsymbol{\alpha}^{k+1} &= \boldsymbol{\alpha}^k + \delta \boldsymbol{\alpha}, \quad \boldsymbol{\alpha}^{k=0} = \boldsymbol{\alpha}_0 \end{aligned} \quad (\text{B.6})$$

where $\bar{\mathbf{J}}$ is the effective tensor of inertia, calculated to be

$$\bar{\mathbf{J}} = \frac{1}{\theta \Delta t} \mathbf{J} = \begin{pmatrix} \frac{I_1}{\theta \Delta t^2} & \frac{-\omega_3(I_2 - I_3)}{\theta \Delta t} & \frac{-\omega_2(I_2 - I_3)}{\theta \Delta t} \\ \frac{-\omega_3(I_3 - I_1)}{\theta \Delta t} & \frac{I_2}{\theta \Delta t^2} & \frac{-\omega_1(I_3 - I_1)}{\theta \Delta t} \\ \frac{-\omega_2(I_1 - I_2)}{\theta \Delta t} & \frac{-\omega_1(I_1 - I_2)}{\theta \Delta t} & \frac{I_3}{\theta \Delta t^2} \end{pmatrix} \quad (\text{B.7})$$

We see that equation (B.6)a has an identical structure to equation (4.10) except now the problem needs to be solved incrementally within each time step. The necessary modification to the formulation then entails defining an incremental problem within each time step and replacing the rotational equilibrium equations of the form given by equation (4.10) with equation (B.6)a.

We note several properties of the effective tensor of inertia given by equation (B.7) in relation to the proposed mathematical programming framework. First, the terms are functions of the body frame angular velocities. Second, the effective tensor of inertia is no longer diagonal. In the force-based problem described by equation (4.15), the inverse of the global moment of inertia matrix is required. However, recognizing that the global moment of inertia is now block diagonal, the inverse of the global moment of inertia is another block diagonal matrix, which is composed of the inverse of 3×3 blocks and these can be calculated efficiently. Finally, the non-symmetry of $\bar{\mathbf{J}}$ poses no problem since the associated quadratic term for a non-symmetric matrix \mathbf{Q} can be written as

$$\delta\boldsymbol{\alpha}^T \mathbf{Q} \delta\boldsymbol{\alpha} = \frac{1}{2} \delta\boldsymbol{\alpha}^T (\mathbf{Q} + \mathbf{Q}^T) \delta\boldsymbol{\alpha} \quad (\text{B.8})$$

which implies that a non-symmetric matrix \mathbf{Q} can be replaced by $\frac{1}{2}(\mathbf{Q} + \mathbf{Q}^T)$.

Computationally, a sequence of quadratic programming problems is solved within a time step for the incremental unknowns $(\delta\mathbf{x}, \delta\boldsymbol{\alpha})$ until a prescribed tolerance is reached. We note that we can formulate the translational problem incrementally by simply replacing $\Delta\mathbf{x}$ with $\delta\mathbf{x}$; this is possible because the translational equilibrium equations already have a linear structure. Finally, we need to update the orientation of each particle. Here, a singularity-free quaternion approach [55] may be taken. We denote the quaternion vector representing the orientation of the particle as $\mathbf{z} = (z_i), i = 1, \dots, 4$. The required orientation matrix of each particle can be calculated as a function of quaternion values as

$$\mathbf{A}(\mathbf{z}) = \begin{pmatrix} -z_1^2 + z_2^2 - z_3^2 + z_4^2 & -2(z_1 z_2 - z_3 z_4) & 2(z_2 z_3 + z_1 z_4) \\ -2(z_1 z_2 + z_3 z_4) & z_1^2 - z_2^2 - z_3^2 + z_4^2 & -2(z_1 z_3 - z_2 z_4) \\ 2(z_2 z_3 - z_1 z_4) & -2(z_1 z_3 + z_2 z_4) & -z_1^2 - z_2^2 + z_3^2 + z_4^2 \end{pmatrix} \quad (\text{B.9})$$

In turn, the evolution of the quaternions can be expressed as a singularity-free set of equations as

$$\dot{\mathbf{z}} = \Psi \mathbf{z}, \quad \mathbf{z}^T \mathbf{z} = 1 \quad (\text{B.10})$$

where

$$\Psi = \frac{1}{2} \begin{pmatrix} 0 & \omega_3 & -\omega_1 & -\omega_2 \\ -\omega_3 & 0 & -\omega_2 & \omega_1 \\ \omega_1 & \omega_2 & 0 & \omega_3 \\ \omega_2 & -\omega_1 & -\omega_3 & 0 \end{pmatrix} \quad (\text{B.11})$$

The general solution is given by

$$\mathbf{z} = \exp \left(\int_{t_0}^t \Psi[\omega(s)] ds \right) \mathbf{z}_0 \quad (\text{B.12})$$

Here, several choices of updating \mathbf{z} exist. One possible choice is the generalized trapezoidal rule of the form

$$\int_{t_0}^t \Psi[\omega(s)] ds \approx \Delta t [\theta \Psi + (1 - \theta) \Psi_0] =: \Delta t \Psi_\theta \quad (\text{B.13})$$

where we have used the same θ parameter as in equation (B.2). In this case, one can update \mathbf{z} as

$$\mathbf{z} = \exp(\Delta t \Psi_\theta) \mathbf{z}_0 \quad (\text{B.14})$$

Efficient algorithms for the computation of matrix exponentials can be found in [140].

Bibliography

- [1] G. C. Cho, J. Dodds, and J. C. Santamarina. Particle shape effects on packing density, stiffness, and strength: Natural and crushed sands. *Journal of Geotechnical and Geoenvironmental Engineering*, 132(5):591–602, 2006.
- [2] J. E. Andrade and C. F. Avila. Granular element method (GEM): linking inter-particle forces with macroscopic loading. *Granular Matter*, 14:1–13, 2012.
- [3] R. Hurley, E. Marteau, G. Ravichandran, and J. E. Andrade. Extracting inter-particle forces in opaque granular materials: Beyond photoelasticity. *Journal of the Mechanics and Physics of Solids*, 63(0):154 – 166, 2014.
- [4] J. E. Andrade, I. Vlahinić, K.-W. Lim, and A. Jerves. Multiscale ‘tomography-to-simulation’ framework for granular matter: the road ahead. *Géotechnique Letters*, 2, 2012.
- [5] J. Bonet and R. D. Wood. *Nonlinear Continuum Mechanics for Finite Element Analysis*. Cambridge University Press, Cambridge, UK, 1997.
- [6] C. S. Desai and H. J. Sewardane. *Constitutive Laws for Engineering Materials*. Prentice-Hall, Inc., 1984.
- [7] K. C. Ellison and J. E. Andrade. Liquefaction mapping in finite elements simulations. *Journal of Geotechnical and Geoenvironmental Engineering*. In press. doi:10.1061/(ASCE)GT.1943-5606.0000122, 2009.
- [8] R. I. Borja and J. E. Andrade. Critical state plasticity, Part VI: Meso-scale finite element simulation of strain localization in discrete granular materials. *Computer Methods in Applied Mechanics and Engineering*, 195:5115–5140, 2006.

- [9] E. Grueschow and J. W. Rudnicki. Elliptic yield cap constitutive modeling for high porosity sandstone. *International Journal of Solids and Structures*, 42(16-17):4574–4587, 2005.
- [10] M. T. Manzari and Y. F. Dafalias. A critical state two-surface plasticity model for sands. *Géotechnique*, 43:255–272, 1997.
- [11] Y. F. Dafalias and E. P. Popov. A model of nonlinearly hardening materials for complex loadings. *Acta Mechanica*, 21:173–192, 1975.
- [12] F. L. DiMaggio and I. S. Sandler. Material model for granular soils. *Journal of the Engineering Mechanics Division-ASCE*, 97:935–950, 1971.
- [13] M. Oda, T. Takemura, and M. Takahashi. Microstructure in shear band observed by microfocus X-ray computed tomography. *Géotechnique*, 54:539–542, 2004.
- [14] K. A. Alshibli, S. Sture, N. C. Costes, M. L. Frank, F. R. Lankton, S. N. Batiste, and R. A. Swanson. Assessment of localized deformations in sand using X-ray computed tomography. *Geotechnical Testing Journal, ASCE*, 23:274–299, 2000.
- [15] R. A. Ketcham and W. D. Carlson. Acquisition, optimization and interpretation of X-ray computed tomographic imagery: applications to the geosciences. *Computers & Geosciences*, 27:381–400, 2001.
- [16] L. Wang, J. Y. Park, and Y. Fu. Representation of real particles for DEM simulation using X-ray tomography. *Construction and Building Materials*, 21:338–346, 2005.
- [17] S. A. Hall, M. Bornert, J. Desrues, Y. Pannier, N. Lenoir, G. Viggiani, and P. Bésuelle. Discrete and continuum analysis of localized deformation in sand using X-ray micro CT and volumetric digital image correlation. *Géotechnique*, 60:315–322, 2010.
- [18] R. V. Martins, L. Margulies, S. Schmidt, H. F. Poulsen, and T. Leffers. Simultaneous measurement of the strain tensor of 10 individual grains embedded in an Al tensile sample. *Materials Science and Engineering A*, 387-389:84–88, 2004.
- [19] S. A. Hall, J. Wright, T. Pirling, E. Andò, D. J. Hughes, and G. Viggiani. Can intergranular force transmission be identified in sand? *Granular Matter*, Doi:10.1007/s10035-011-0251-x, 2011.

- [20] M. M. Frocht. *Photoelasticity*, volume 1. John Wiley & Sons Ltd., New York, 1941.
- [21] M. M. Frocht. *Photoelasticity*, volume 2. John Wiley & Sons Ltd., New York, 1941.
- [22] J. E. Andrade, C. F. Avila, N. Lenoir, S. A. Hall, and G. Viggiani. Multiscale modeling and characterization of granular matter: from grain scale kinematics to continuum mechanics. *Journal of the Mechanics and Physics of Solids*, 59:237–250, 2011.
- [23] J. Christoffersen, M. M. Mehrabadi, and S. Nemat-Nasser. A micromechanical description of granular material behavior. *Journal of Applied Mechanics*, 48:339–344, 1981.
- [24] P. A. Cundall and O. D. L. Strack. A discrete numerical model for granular assemblies. *Géotechnique*, 29:47–65, 1979.
- [25] B. Sukumaran and A. K. Ashmawy. Quantitative characterisation of the geometry of discrete particles. *Géotechnique*, 51:619–627, 2001.
- [26] X. Garcia, L. T. Akanji, M. J. Blunt, S. K. Matthai, and J. P. Latham. Numerical study of the effects of particle shape and polydispersity on permeability. *Physical Review E*, 80:021304, 2009.
- [27] K. Iwashita and M. Oda. Rolling resistance at contacts in simulation of shear band development by dem. *Journal of engineering mechanics*, 124(3):285–292, 1998.
- [28] K. Iwashita and M. Oda. Micro-deformation mechanism of shear banding process based on modified distinct element method. *Powder Technology*, 109(1):192–205, 2000.
- [29] A. Tordesillas and D. C. Incorporating rolling resistance and contact anisotropy in micromechanical models of granular media. *Powder Technology*, 124(1):106–111, 2002.
- [30] A. Tordesillas, J. Peters, and M. Muthuswamy. Role of particle rotations and rolling resistance in a semi-infinite particulate solid indented by a rigid flat punch. *ANZIAM Journal*, 46:C260–C275, 2005.
- [31] M. J. Jiang, H.-S. Yu, and D. Harris. A novel discrete model for granular material incorporating rolling resistance. *Computers and Geotechnics*, 32(5):340–357, 2005.

- [32] X. Li, X. Chu, and Y. T. Feng. A discrete particle model and numerical modeling of the failure modes of granular materials. *Engineering Computations*, 22(8):894–920, 2005.
- [33] W. Zhang, J. Wang, and M. Jiang. Dem-aided discovery of the relationship between energy dissipation and shear band formation considering the effects of particle rolling resistance. *Journal of Geotechnical and Geoenvironmental Engineering*, 139(9):1512–1527, 2013.
- [34] J. Ai, J.-F. Chen, J. M. Rotter, and J. Y. Ooi. Assessment of rolling resistance models in discrete element simulations. *Powder Technology*, 206(3):269–282, 2011.
- [35] A.K. Ashmawy, B. Sukumaran, and A. V. Hoang. Evaluating the influence of particle shape on liquefaction behavior using discrete element method. In *Proceedings of the thirteenth international offshore and polar engineering conference (ISOPE 2003) Honolulu, Hawaii*, May 2003.
- [36] X. Garcia, J.-P. Latham, J. Xiang, and J.P. Harrison. A clustered overlapping sphere algorithm to represent real particles in discrete element modelling. *Géotechnique*, 59:779–784, 2009.
- [37] P. A. Cundall. Formulation of a three-dimensional distinct element model - Part I: A scheme to detect and represent contacts in a system composed of many polyhedral blocks. *International Journal of Rock Mechanics and Mining Sciences*, 25(3):107–116, 1988.
- [38] D. Zhao, E. G. Nezami, Y. M. A. Hashash, and J. Ghaboussi. Three-dimensional discrete element simulation for granular materials. *Engineering Computations*, 23:749–770, 2006.
- [39] F. Alonso-Marroquin and H. J. Herrmann. Calculation of the incremental stress-strain relation of a polygonal packing. *Physical Review E*, 66:021301, 2002.
- [40] F. Dubois and M. Jean. The non smooth contact dynamic method: recent LMGC90 software developments and application. In Peter Wriggers and Udo Nackenhorst, editors, *Analysis and Simulation of Contact Problems*, volume 27 of *Lecture Notes in*

Applied and Computational Mechanics, pages 375–378. Springer Berlin Heidelberg, 2006.

- [41] A. A. Peña, P. G. Lind, and H. J. Herrmann. Modeling slow deformation of polygonal particles using DEM. *Particuology*, 6:506 – 514, 2008.
- [42] C. Ericson. *Real-Time Collision Detection (The Morgan Kaufmann Series in Interactive 3-D Technology) (The Morgan Kaufmann Series in Interactive 3D Technology)*. Morgan Kaufmann Publishers Inc., San Francisco, CA, USA, 2004.
- [43] L. Pournin and T. M. Liebling. A generalization of distinct element method to three dimensional particles with complex shapes. In *Proceedings of Powders & Grains (Balkema, Leiden, 2005)*, 2005.
- [44] S. A. Galindo-Torres and D. M. Pedroso. Molecular dynamics simulations of complex-shaped particles using voronoi-based spheropolyhedra. *Phys. Rev. E*, 81:061303, 2010.
- [45] G. T. Houlsby. Potential particles: a method for modelling non-circular particles in DEM. *Computers & Geotechnics*, 36:953–959, 2009.
- [46] J. Harkness. Potential particles for the modelling of interlocking media in three dimensions. *International Journal for Numerical Methods in Engineering*, 80(12):1573–1594, 2009.
- [47] I. Vlahinić, E. Andò, G. Viggiani, and J. E. Andrade. Towards a more accurate characterization of granular media: extracting quantitative descriptors from tomographic images. *Granular Matter*, pages 1–13, 2013. doi:10.1007/s10035-013-0460-6.
- [48] T. J. R. Hughes, J. A. Cottrell, and Y. Bazilevs. Isogeometric analysis: CAD, finite elements, NURBS, exact geometry and mesh refinement. *Computer Methods in Applied Mechanics and Engineering*, 194:4135–4195, 2005.
- [49] J. E. Andrade, K.-W. Lim, C. F. Avila, and I. Vlahinić. Granular element method for computational particle mechanics. *Computer Methods in Applied Mechanics and Engineering*, 241-244:262–274, 2012.

- [50] K.-W. Lim and J. E. Andrade. Granular element method for three-dimensional discrete element calculations. *International Journal for Numerical and Analytical Methods in Geomechanics*, 38(2):167–188, 2014.
- [51] K.-W. Lim, K. Krabbenhoft, and J. E. Andrade. A contact dynamics approach to the granular element method. *Computer Methods in Applied Mechanics and Engineering*, 268:557–573, 2014.
- [52] K.-W. Lim, K. Krabbenhoft, and J. E. Andrade. On the contact treatment of non-convex particles in the granular element method. *Computational Particle Mechanics*, 1(3):257–275, 2014.
- [53] R. Hart, P. A. Cundall, and J. Lemos. Formulation of a three-dimensional distinct element model - Part II: Mechanical calculations for motion and interaction of a system composed of many polyhedral blocks. *International Journal of Rock Mechanics and Mining Sciences*, 25(3):117–125, 1988.
- [54] O. R. Walton and R. L. Braun. Simulation of rotary-drum and repose tests for frictional spheres and rigid sphere clusters. *DOE/NSF Workshop on Flow of Particulates*, pages 1–17, 1993.
- [55] D. J. Evans and S. Murad. Singularity free algorithm for molecular dynamics simulation of rigid polyatomics. *Molecular Physics*, 34(2):327–331, 1977.
- [56] H. Goldstein, C. P. Poole, and J. L. Safko. *Classical Mechanics (3rd Edition)*. Addison Wesley, 3rd edition, 2001.
- [57] X. Tu and J. E. Andrade. Criteria for static equilibrium in particulate mechanics computations. *International Journal for Numerical Methods in Engineering*, 75:1581–1606, 2008.
- [58] H. Hinrichsen and D. E. Wolf. *The Physics of Granular Media*. Wiley-VCH, Weinheim, 2004.
- [59] P. Lötstedt. Coulomb friction in two-dimensional rigid body systems. *ZAMM - Journal of Applied Mathematics and Mechanics / Zeitschrift fñr Angewandte Mathematik und Mechanik*, 61(12):605–615, 1981.

- [60] P. Lötstedt. Mechanical systems of rigid bodies subject to unilateral constraints. *SIAM Journal on Applied Mathematics*, 42(2):pp. 281–296, 1982.
- [61] J. J. Moreau. Some numerical methods in multibody dynamics: application to granular materials. *Eur. J. Mech. A Solids*, 13:93–114, 1994.
- [62] M. Jean. The non-smooth contact dynamics method. *Computer Methods in Applied mechanics and Engineering*, 177(3-4):235–257, 1999.
- [63] J. C. Simo and T. J. R. Hughes. *Computational Inelasticity*. Springer-Verlag, New-York, 1998.
- [64] P. Lötstedt. Numerical simulation of time-dependent contact and friction problems in rigid body mechanics. *SIAM Journal on Scientific and Statistical Computing*, 5(2):370–393, 1984.
- [65] D. Baraff. Coping with friction for non-penetrating rigid body simulation. *ACM SIGGRAPH Computer Graphics*, 25(4):31–40, 1991.
- [66] D. Baraff. Fast contact force computation for nonpenetrating rigid bodies. In *SIGGRAPH '94 Conference Proceedings*, pages 23–32. ACM, 1994.
- [67] D. Stewart and J. C. Trinkle. An implicit time-stepping scheme for rigid body dynamics with coulomb friction. *International Journal for Numerical Methods in Engineering*, 39:2673–2691, 1996.
- [68] M. Anitescu and F. A. Potra. Formulating dynamic multi-rigid-body contact problems with friction as solvable linear complementarity problems. *Nonlinear Dynamics*, 14:231–247, 1997.
- [69] C. E. Lemke. Bimatrix equilibrium points and mathematical programming. *Management Science*, 11(7):pp. 681–689, 1965.
- [70] S. Boyd and L. Vandenberghe. *Convex Optimization*. Cambridge University Press, New York, NY, USA, 2004.
- [71] S. C. Billups, S. P. Dirkse, and M. C. Ferris. A comparison of large scale mixed complementarity problem solvers. *Computational Optimization and Applications*, 7(1):3–25, 1997.

- [72] K. Krabbenhoft, A.V. Lyamin, J. Huang, and M. Vicente da Silva. Granular contact dynamics using mathematical programming methods. *Computers and Geotechnics*, 241-244:262–274, 2012.
- [73] C. Noguier-Lehon, B. Cambou, and E. Vincens. Influence of particle shape and angularity on the behaviour of granular materials: a numerical analysis. *International Journal for Numerical and Analytical Methods in Geomechanics*, 27(14):1207–1226, 2003.
- [74] S. McNamara and H. Herrmann. Measurement of indeterminacy in packings of perfectly rigid disks. *Phys. Rev. E*, 70:061303, Dec 2004.
- [75] M. Renouf, F. Dubois, and P. Alart. A parallel version of the non smooth contact dynamics algorithm applied to the simulation of granular media. *Journal of Computational and Applied Mathematics*, 168(12):375 – 382, 2004.
- [76] L. Staron and E. J. Hinch. Study of the collapse of granular columns using two-dimensional discrete-grain simulation. *Journal of Fluid Mechanics*, 545:1–27, 2005.
- [77] A. Taboada, K.-J. Chang, F. Radjai, and F. Bouchette. Rheology, force transmission, and shear instabilities in frictional granular media from biaxial numerical tests using the contact dynamics method. *Journal of Geophysical Research: Solid Earth*, 110(B9), 2005.
- [78] G. Saussine, C. Cholet, P.E. Gautier, F. Dubois, C. Bohatier, and J.J. Moreau. Modelling ballast behaviour under dynamic loading. part 1: A 2d polygonal discrete element method approach. *Computer Methods in Applied Mechanics and Engineering*, 195:2841 – 2859, 2006.
- [79] A. Ries, D. E. Wolf, and T. Unger. Shear zones in granular media: Three-dimensional contact dynamics simulation. *Phys. Rev. E*, 76:051301, Nov 2007.
- [80] L. Staron and E. J. Hinch. The spreading of a granular mass: role of grain properties and initial conditions. *Granular Matter*, 9:205–217, 2007.
- [81] R. Farhang and R. Vincent. Contact dynamics as a nonsmooth discrete element method. *Mechanics of Materials*, 41(6):715 – 728, 2009.

- [82] N. Estrada, E. Azéma, F. Radjai, and A. Taboada. Identification of rolling resistance as a shape parameter in sheared granular media. *Phys. Rev. E*, 84:011306, Jul 2011.
- [83] P.-Y. Lagree, L. Staron, and S. Popinet. The granular column collapse as a continuum: validity of a two-dimensional Navier-Stokes model with a $\mu(I)$ -rheology. *Journal of Fluid Mechanics*, 686:378–408, 2011.
- [84] L. Piegl and W. Tiller. *The NURBS book (2nd ed.)*. Springer-Verlag New York, Inc., New York, NY, USA, 1997.
- [85] C.-K. Shene. CS3621 Introduction to Computing with Geometry. <http://www.cs.mtu.edu/~shene/COURSES/cs3621/NOTES/>, July 2011.
- [86] J. Lowther J. Fisher and C.-K. Shene. If you know B-Splines well, you also know NURBS! *SIGCSE Bull.*, 36:343–347, March 2004.
- [87] M. G. Cox. The numerical evaluation of B-splines. Technical report, National Physics Laboratory DNAC 4, 1971.
- [88] C. De Boor. On calculation with B-splines. *Journal of Approximation Theory*, 6:50–62, 1972.
- [89] Robert McNeel & Associates. Rhinoceros (Rhino). <http://www.rhino3d.com/>.
- [90] B. Saint-Cyr, J.-Y. Delenne, C. Voivret, F. Radjai, and P. Sornay. Rheology of granular materials composed of nonconvex particles. *Phys. Rev. E*, 84:041302, 2011.
- [91] F. Ludewig and N. Vandewalle. Strong interlocking of nonconvex particles in random packings. *Phys. Rev. E*, 85:051307, 2012.
- [92] T.A. Laursen. *Computational Contact and Impact Mechanics: Fundamentals of Modeling Interfacial Phenomena in Nonlinear Finite Element Analysis*. Springer, Berlin, 2002.
- [93] I. Temizer, P. Wriggers, and T.J.R. Hughes. Contact treatment in isogeometric analysis with NURBS. *Computer Methods in Applied Mechanics and Engineering*, 200(9 - 12):1100 – 1112, 2011.

- [94] D. R. Jones, C. D. Perttunen, and B. E. Stuckman. Lipschitzian optimization without the lipschitz constant. *Journal of Optimization Theory and Applications*, 79(1):157–181, 1993.
- [95] R. L. Graham. An efficient algorithm for determining the convex hull of a finite planar set. *Information processing letters*, 1(4):132–133, 1972.
- [96] J. M. Gablonsky. An implementation of the DIRECT algorithm, technical report crsc-tr98-29. Technical report, Center for Research in Scientific Computation, North Carolina State University, Raleigh, NC, 1998.
- [97] C. T. Kelley. *Iterative Methods for Optimization*, number 18 in *Frontiers in Applied Mathematics*. SIAM, Philadelphia, 1999.
- [98] J. Nocedal and S. J. Wright. *Numerical Optimization*. Springer, New York, USA, 2nd edition, 2006.
- [99] K. Krabbenhoft, A.V. Lyamin, J. Huang, and M. Vicente da Silva. Granular contact dynamics with particle elasticity. *Granular Matter*, 14:607–619, 2012.
- [100] J.F. Sturm. SeDuMi 1.02, a MATLAB toolbox for optimization over symmetric cones. *Optimization Methods and Software*, 11–12:625–653, 1999.
- [101] MOSEK ApS. MOSEK. <http://www.mosek.com/>.
- [102] J. J. Moreau. Bounded variation in time. In *Moreau, J.J.; Panagiotopoulos, P.D.; Strang, G (eds.) Topics in Nonsmooth Mechanics*, volume 1, pages 1–74. Basel-Boston-Stuttgart: Birkhauser Verlag, 1987.
- [103] J. J. Moreau. Unilateral contact and dry friction in finite freedom dynamics. In *Moreau, J.J.; Panagiotopoulos, P. (eds.) Nonsmooth Mechanics and Applications, CISM Courses and Lectures*, volume 302, pages 1–82. Springer, Berlin, 1988.
- [104] J. Huang, M. Vicente da Silva, and K. Krabbenhoft. Three-dimensional granular contact dynamics with rolling resistance. *Computers and Geotechnics*, In Press, 2012.
- [105] W. L. Wood. *Practical Time-Stepping Schemes*. Oxford University Press, Oxford, 1990.

- [106] P. Souloumiac, Y.M. Leroy, B. Maillot, and K. Krabbenhoft. Predicting stress distributions in fold-thrust and accretionary wedges by optimisation. *J. Geophys. Res.*, 114, B09404, 2009.
- [107] P. Souloumiac, K. Krabbenhoft, Y.M. Leroy, and B. Maillot. Failure in accretionary wedges with the maximum strength theorem. *Comput. Geosci.*, 19:793–811, 2010.
- [108] S. J. Wright. *Primal-dual interior-point methods*. Society for Industrial and Applied Mathematics, Philadelphia, PA, USA, 1997.
- [109] F. Radjai, L. Brendel, and S. Roux. Nonsmoothness, indeterminacy, and friction in two-dimensional arrays of rigid particles. *Phys. Rev. E*, 54:861–873, 1996.
- [110] J. H. Snoeijer, T. J. H. Vlugt, M. van Hecke, and W. van Saarloos. Force network ensemble: A new approach to static granular matter. *Phys. Rev. Lett.*, 92:054302, 2004.
- [111] S. McNamara, R. García-Rojo, and H. Herrmann. Indeterminacy and the onset of motion in a simple granular packing. *Phys. Rev. E*, 72:021304, 2005.
- [112] T. Unger, J. Kertész, and D. E. Wolf. Force indeterminacy in the jammed state of hard disks. *Phys. Rev. Lett.*, 94:178001, 2005.
- [113] R. D. Mindlin. Compliance of elastic bodies in contact. *Journal of Applied Mechanics*, 71:259–268, 1949.
- [114] R. Phillips. *Crystals, Defects and Microstructures: Modeling Across Scales*. Cambridge University Press, 2001.
- [115] M. Oda. Initial fabrics and their relations to mechanical properties of granular materials. *Soils and Foundations*, 12:17–36, 1972.
- [116] A. L. Rechenmacher and R. J. Finno. Digital image correlation to evaluate shear banding in dilative sands. *Geotechnical Testing Journal, ASCE*, 27:1–10, 2004.
- [117] K.A. Alshibli and A. Hasan. Spatial variation of void ratio and shear band thickness in sand using x-ray computed tomography. *Géotechnique*, 58(4):249–257, 2008.

- [118] E. Andò, S. A. Hall, G. Viggiani, J. Desrues, and P. Besuelle. Grain-scale experimental investigation of localised deformation in sand: a discrete particle tracking approach. *Acta Geotechnica*, 7(1):1–13, 2012.
- [119] E. J. Garboczi. Three-dimensional mathematical analysis of particle shape using X-ray tomography and spherical harmonics: Application to aggregates used in concrete. *Cement and Concrete Research*, 32(10):1621–1638, 2002.
- [120] M. Saadatfar, M. L. Turner, C. H. Arns, H. Averdunk, T. J. Senden, A. P. Sheppard, R. M. Sok, W. V. Pinczewski, J. Kelly, and M. A. Knackstedt. Rock fabric and texture from digital core analysis. In *SPWLA 46th Annual Logging Symposium, New Orleans, Louisiana, June*, pages 26–29, 2005.
- [121] E. T. Bowman, K. Soga, and W. Drummond. Particle shape characterisation using fourier descriptor analysis. *Géotechnique*, 51(6):545–554, 2001.
- [122] G. Mollon and J. Zhao. 3D generation of realistic granular samples based on random fields theory and Fourier shape descriptors. *Computer Methods in Applied Mechanics and Engineering*, in press.
- [123] E. Weinan. *Principles of multiscale modeling*. Cambridge University Press, 2011.
- [124] C. Wellmann, C. Lillie, and P. Wriggers. Homogenization of granular material modeled by a three-dimensional discrete element method. *Computers and Geotechnics*, 35:394–405, 2007.
- [125] C. Dascalu and B. Cambou. Special issue on multiscale approaches to geomaterials. In C. Dascalau and B. Cambou, editors, *Acta Geotechnica*, volume 3. Springer, 2008.
- [126] H.A. Meier, P. Steinmann, and E. Kuhl. Towards multiscale computation of confined granular media - contact forces, stresses and tangent operators. *Technische Mechanik*, 28:32–43, 2008.
- [127] J. E. Andrade and X. Tu. Multiscale framework for behavior prediction in granular media. *Mechanics of Materials*, 41:652–669, 2009.

- [128] A. Koynov, I. Akseli, and A.M. Cuitino. Modeling and simulation of compact strength due to particle bonding using a hybrid discrete-continuum approach. *International Journal of Pharmaceutics*, 418:273–285, 2011.
- [129] R. A. Regueiro and B. Yan. Concurrent multiscale computational modeling for dense dry granular materials interfacing deformable solid bodies. *Springer Series in Geomechanics and Geoengineering*, pages 251–273, 2011.
- [130] T. K. Nguyen, G. Combe, D. Caillerie, and J. Desrues. FEM×DEM modelling of cohesive granular materials: Numerical homogenisation and multi-scale simulations. *Acta Geophysica*, 62(5):1109–1126, 2014.
- [131] N. Guo and J. Zhao. A coupled FEM/DEM approach for hierarchical multiscale modelling of granular media. *International Journal for Numerical Methods in Engineering*, 10.1002/nme.4702, 2014.
- [132] P. Soille. *Morphological Image Analysis, Principles and Applications*. Springer, Berlin, 2nd edition, 2004.
- [133] N. Lenoir, M. Bornert, J. Desrues, and G. Viggiani. 3D digital image correlation applied to X-ray microtomography images from triaxial compression tests on argillaceous rock. *Strain*, 43:193–205, 2007.
- [134] M. Babić. Discrete Particle Numerical Simulation of Granular Material Behavior. Technical Report 88-11, Department of Civil and Environmental Engineering, Clarkson University, 1988.
- [135] M. Anitescu. Optimization-based simulation of nonsmooth rigid multibody dynamics. *Mathematical Programming*, 105(1):113–143, 2006.
- [136] M. Anitescu and A. Tasora. An iterative approach for cone complementarity problems for nonsmooth dynamics. *Computational Optimization and Applications*, 47(2):207–235, 2010.
- [137] A. Tasora and M. Anitescu. A convex complementarity approach for simulating large granular flows. *Journal of Computational and Nonlinear Dynamics*, 5(3):031004, 2010.

- [138] A. Tasora and M. Anitescu. A matrix-free cone complementarity approach for solving large-scale, nonsmooth, rigid body dynamics. *Computer Methods in Applied Mechanics and Engineering*, 200(5):439–453, 2011.
- [139] A. Tasora and M. Anitescu. A complementarity-based rolling friction model for rigid contacts. *Meccanica*, 48(7):1643–1659, 2013.
- [140] C. Moler and C. V. Loan. Nineteen dubious ways to compute the exponential of a matrix, twenty-five years later. *SIAM Review*, 45(1):3–49, 2003.